# In Search of New Phenomena using Polarization

## HERA and ILC

Dissertation

zur Erlangung des Doktorgrades

des Department Physik

der Universität Hamburg

vorgelegt von

Christian Helebrant
aus Lebach

Hamburg
2009

| | |
|---|---|
| Gutacherin/Gutachter der Dissertation: | Dr. Jenny List<br>Prof. Dr. Robert Klanner |
| Gutacherin der Disputation: | Dr. Jenny List<br>Prof. Dr. Caren Hagner |
| Datum der Disputation: | 9. Oktober 2009 |
| Vorsitzender des Prüfungsausschusses: | Dr. Georg Steinbrück |
| Vorsitzender des Promotionsausschusses: | Prof. Dr. Robert Klanner |
| Leiter des Departments Physik: | Prof. Dr. Joachim Bartels |
| Dekan der Fakultät für MIN: | Prof. Dr. Heinrich Graener |

# Abstract

The longitudinal polarization of leptons can be used as an important tool in the search for new phenomena at particle colliders. In the first part of this thesis a search for first generation leptoquarks at the H1 experiment is presented. During the HERA-2 runperiod polarized lepton beams were used. The analysis presented herein utilizes this fact in order to enhance the sensitivity to these chirally coupling leptoquarks. Since no evidence for their existence is found, exclusion limits depending on the mass and Yukawa coupling are calculated. This analysis can exclude leptoquarks coupling at electromagnetic strength up to masses of $280 - 300\,\mathrm{GeV}$, depending on the leptoquark quantum numbers.

A new domain of physics is expected to be open to the planned electron positron linear collider ILC, where polarized lepton beams will play an important role. In order to fully exploit its physics potential, the polarization will have to be measured with an as yet unequaled precision of 0.25%, which is expected to be limited by systematic effects, like the nonlinearity of the photodetectors employed. In the second part of this thesis several methods are tested with respect to their capability to resolve photodetector nonlinearities at the permille level, and checked for their long term stability. With some of the methods presented herein it will be possible to measure and correct photodetector nonlinearities at a running ILC experiment with the accuracy required in order to achieve the aimed precision of the polarization measurement.

# Zusammenfassung

Die longitudinale Polarisation von Leptonen kann an Teilchenbeschleunigern als wichtiges Hilfsmittel bei der Suche nach neuen Phänomenen dienen. Im ersten Teil dieser Arbeit wird eine Suche nach Leptoquarks der ersten Generation am H1-Experiment vorgestellt. Während der HERA-2 Runperiode wurden dort polarisierte Leptonstrahlen genutzt. Diese Analyse verwendet die Polarisation, um die Sensitivität für die chiral koppelnden Leptoquarks zu erhöhen. Aufgrund der Abwesenheit von Anzeichen für die Existenz von Leptoquarks wurden Ausschlussgrenzen in Abhängigkeit von Masse und Yukawa-Kopplung berechnet. Diese Analyse kann mit elektromagnetischer Stärke koppelnde Leptoquarks mit Massen von bis zu $280 - 300\,\mathrm{GeV}$, je nach Leptoquark-Quantenzahlen, ausschliessen.

Es wird davon ausgegangen, dass der geplante Elektron-Positron-Linearbeschleuniger ILC der Physik neue Bereiche eröffnen wird. Dabei werden polarisierte Strahlleptonen eine wichtige Rolle spielen. Um deren Potenzial voll ausnutzen zu können, soll ihr Polarisationsgrad mit bislang unerreichter Genauigkeit von $0.25\%$ gemessen werden. Begrenzt wird die Präzision dabei durch systematische Effekte, wie beispielsweise die Nichtlinearität der verwendeten Fotodetektoren. Im zweiten Teil dieser Arbeit werden Methoden im Hinblick auf ihre Eignung überprüft, Nichtlinearitäten von Fotodetektoren im Promille-Bereich aufzulösen. Ausserdem wird die Stabilität dieser Methoden über längere Zeiträume hin untersucht. Mit einigen der präsentierten Methoden wird es möglich sein, Fotodetektor-Nichtlinearitäten während des laufenden ILC-Experiments mit der nötigen Genauigkeit zu ermitteln und zu korrigieren, um so die angestrebte Präzision der Polarisationsmessung zu erreichen.

# Contents


1. Introduction 1

I. Search for First Generation Leptoquarks at H1 11

2. Physics at HERA 13
   2.1. Deep Inelastic Scattering . . . 13
   2.2. Neutral and Charged Current Cross Sections . . . 15
   2.3. Background Processes . . . 18
   2.4. Leptoquarks in $ep$ Interactions . . . 20

3. The H1 Detector 27
   3.1. General Overview . . . 27
   3.2. Tracking Detectors . . . 27
   3.3. Calorimetry . . . 31
   3.4. Time-of-Flight System . . . 33
   3.5. Luminosity System . . . 34
   3.6. Trigger System . . . 34

4. Dataset and Monte Carlo Simulations 37
   4.1. The HERA-2 Dataset . . . 37
   4.2. Kinematic Reconstruction and Particle Identification . . . 38
   4.3. Electromagnetic and Hadronic Energy Calibrations . . . 42
   4.4. Monte Carlo Generators . . . 44

5. Selection of Neutral and Charged Current Events 47
   5.1. Event Timing . . . 47
   5.2. Topological Signature . . . 49
   5.3. Primary Vertex . . . 50
   5.4. Triggers . . . 50
   5.5. Fiducial Volume . . . 52
   5.6. Limitation of Kinematic Range . . . 52
   5.7. Jet Requirements . . . 53
   5.8. Neutral Current Specific Cuts . . . 53

5.9. Charged Current Specific Cuts . . . . . 54
5.10. Monte Carlo Simulation Reweighting . . . . . 58
5.11. Systematic Uncertainties . . . . . 60
5.12. Final Event Selections . . . . . 64

**6. Search for Leptoquarks** **73**
6.1. Leptoquark Signal in the Selected Data . . . . . 73
6.2. Leptoquark Simulation . . . . . 74
6.3. Statistical Method . . . . . 75
6.4. Exclusion Limits . . . . . 79

**II. Photodetector Studies for an ILC Polarimeter** **85**

**7. The ILC Compton Polarimeter** **87**
7.1. Compton Polarimetry . . . . . 87
7.2. ILC Compton Polarimeter . . . . . 90

**8. Instruments** **95**
8.1. Photodetectors . . . . . 95
8.2. Analog-to-Digital Converters . . . . . 98
8.3. Nonlinearity . . . . . 101

**9. Testing Facility** **103**
9.1. The Light-tight box . . . . . 103
9.2. Photodetector . . . . . 104
9.3. Light-emitting Diode . . . . . 105
9.4. Function Generator . . . . . 106
9.5. Data Acquisition . . . . . 107

**10.Photodetector Measurements** **115**
10.1. General Remarks . . . . . 115
10.2. Optical Filters . . . . . 119
10.3. Pulse Length . . . . . 126
10.4. Double Pulse . . . . . 136
10.5. E158 Method . . . . . 138
10.6. Comparison of Results Obtained with Different Methods . . . . . 140
10.7. Long Term Stability and Calibration . . . . . 144

**Conclusion and Outlook** **151**

**Danksagung** **165**

# Chapter 1.

# Introduction

### The Standard Model of Particle Physics

The Standard Model of Particle Physics [1] successfully describes the experimentally confirmed knowledge of elementary particles and their interactions. Mathematically it is a gauge theory with the gauge group $SU(3) \times SU(2) \times U(1)$. The Standard Model distinguishes fermions with half-integer spins, and bosons with integer spins. While all matter is built up of fermions, the bosons are force carriers. For each particle there exists an anti-particle, which has the inverse additive quantum numbers, but acts identically in all other respects.

All known forces can be reduced to four fundamental interactions: the strong, weak, and electromagnetic interactions, and gravity. The first three can be described with the Standard Model, and even, at sufficiently high energies, be reduced to two forces by the *electroweak unification*. Gravity is well known at macroscopic distances, but no quantumtheoretical description has yet been found. This is due to the fact that at spatial dimensions relevant in experimental particle physics, gravity is many orders of magnitude weaker than the other three interactions. Hence, gravity has to be neglected within particle physics. However, this vast difference in strengths is one of the most challenging mysteries of physics.

The Standard Model includes 12 fermions, that are, to the best of our knowledge, elementary, that is point-like particles which do not possess a substructure. These fermions can be divided into groups of six leptons and six quarks, each of which are grouped in three pairs called *flavors*. The major difference between leptons and quarks is that in addition to electroweak interactions, quarks can also partake in strong interactions. This represents the two pillars of the Standard Model: the Glashow-Salam-Weinberg (GSW) theory, and Quantum Chromodynamics (QCD).

The GSW theory [2, 3, 4] succeeds in describing all weak and electromagnetic interactions through one formalism (*electroweak unification*) as a $SU(2) \times U(1)$ gauge group. Its gauge bosons are the photon and the weakly interacting $W^{\pm}$ and $Z^0$ bosons. The weak interaction differs from all other fundamental forces as it violates parity symmetry. The $Z^0$ boson's coupling to fermions is depedent on the chirality, whereas the $W^{\pm}$ bosons only couple to left-handed fermions and right-handed anti-fermions. This causes weak processes to be sensitive to the polarization of the incident particles - a fact that is central to this thesis and will be discussed further on.

QCD [5, 6] is an $SU(3)$ non-Abelian gauge theory, which has some peculiar implications: The strong force acts on all particles carrying *color charge*. Since the exchange bosons, the gluons, are charge carriers as well they are also subject to strong interactions. At very high energies (very small distances) quarks and gluons act as quasi-free particles (*asymptotic freedom*). The strong force does, however, not diminish but even increase at growing distances, in contrast to all other known interactions (*confinement*). This makes it impossible to separate two quarks, or to observe a free quark.

All fermions and bosons of the Standard Model have been found and measured in experiments. There is, however, one particle postulated by the Standard Model, that has not been discovered yet. The fundamental principle of local gauge invariance requires the exchange bosons to be massless. This is true for the mediators of the strong interactions, the gluons. Although it is possible to describe electromagnetic and weak interactions with one theory (GSW), only one gauge boson is massless (photon), while the mediators of weak interactions, $W^{\pm}$ and $Z^0$, have been found to have a considerable mass: $M_W = 80\,\mathrm{GeV}$, $M_Z = 91\,\mathrm{GeV}$. This problem can be solved by the mechanism of *spontaneous electroweak symmetry breaking*, that introduces the Higgs field [7, 8]. Additional free parameters can be chosen in such a way that the weak gauge bosons become massive, while the photon still remains massless. An experimental confirmation for this theory, i.e. the discovery of the Higgs boson, would complete the Standard Model.

### Beyond the Standard Model

The Standard Model has been proven correct in every high energy physics experiment ever performed. However, despite being an exact model of particle physics, it is also generally accepted that the Standard Model is by no means a complete description, and leaves many questions unanswered.

The symmetry between the lepton and quark sectors (three families of two particles in both) seems to hint at a higher symmetry principle. This 'aesthetical' argument is added physical weight by the existence of certain processes (*triangle anomalies*) that would lead to diverging cross sections if the sum over the charges of the leptons and quarks did not vanish for *every* family separately. A further unresolved issue is posed by the hierarchy problem, the question why electroweak symmetry breaking appears at a scale far below the Planck mass. Closely related is the problem of incredibly precise fine tuning needed to avoid quadratic divergencies in the cross section of some Higgs processes.

A very popular extension of the Standard Model, that may resolve these problems, is called *Supersymmetry* (SUSY). SUSY postulates that for every Standard Model fermion there exists a supersymmetric bosonic partner, and vice versa. In order to explain the absence of SUSY phenomena in current high energy data, however, one must assume a SUSY breaking mechanism leading to higher masses for the supersymmetric particles. SUSY would help remove the quadratic divergencies of the hierarchy problem - while at the same time giving rise to a new hierarchy problem: namely, why SUSY breaking

appears at a scale so far below the Planck scale.

Astrophysical experiments have proven that only about five percent of the entire mass in the universe consists of particles described by the Standard Model. The rest consists of something entirely unknown and thus appropriately named *dark matter* and *dark energy*. The former could, at least in part, be explained by SUSY particles.

A way of explaining the weakness of gravity could be *Large Extra Dimensions*. This hypothesis postulates that gravity, as opposed to the other fundamental forces, propagates in several additional spatial dimensions, thus appearing weak from our four-dimensional point-of-view.

Ever since the successful unification of the weak and electromagnetic interactions, attempts have been made to encompass the strong interaction as well. This *Grand Unification Theory* (GUT) would provide the aforementioned symmetry concerning the lepton and quark sectors. Current estimates place the GUT at energies scales as high as $10^{15}$ GeV, and thus beyond the reach of any imaginable collider experiment. Nevertheless, the leptoquarks, that are subject to the search described in the first part of this thesis, could act as the exchange bosons of GUT.

A further unresolved issue is CP violation, that is synonymous with the question why there is a matter-antimatter asymmetry in our universe. The Standard Model may also be perceived as a precise but nevertheless inelegant theory: At least 19 parameters are required, that have to be found experimentally and do not arise from any fundamental principle.

In order to confirm or discard these theories experiments have to be conducted. In high energy physics these experiments are done using colliders, where particle collisions are studied at very high center-of-mass energies. Some accelerators, especially the two featured in this thesis, HERA and the ILC, used or will be using polarized electron beams. Longitudinally polarized electrons can be a valuable tool in the search for new physics phenomena.

### Polarization and New Physics Phenomena

It was a long held belief of the physical community that parity was a universal symmetry. While this was proven to be correct for the strong and electromagnetic interaction, parity conservation in weak interactions remained experimentally unconfirmed for a long time. In 1957 Wu and others analyzed the beta decay of cobalt-60 and proved that parity conservation is violated in weak interactions. As a consequence the GSW model of electroweak interactions had to be formulated as a chiral gauge theory, introducing chirality dependent couplings.

In collider experiments polarized beams are an important tool to study the Standard Model, or search for new processes. The beam polarization is defined as

$$\mathcal{P} = \frac{N_+ - N_-}{N_+ + N_-} \tag{1.1}$$

with $N_\pm$ denoting the number of particles with positive or negative helicity, respectively. The beam polarization can be used in several ways in the search for new phenomena. Polarization dependent Standard Model processes can be suppressed by choosing the 'wrong' spin configuration. The same principle can be used to enhance rare or new processes. At colliders where both beams are polarized (like the ILC) different spin configurations can be selected at the interaction point, thus allowing to analyze the spin structure of new particles.

At HERA a longitudinally polarized electron or positron beam was used. This allowed, for example, to prove the absence of $W$ bosons coupling to left-handed positrons [10]. In the search for leptoquarks described in this analysis, the polarization is utilized as well. The phenomenological model used assumes chirally coupling leptoquarks. The major Standard Model background for these hypothetical processes are neutral current interactions. These are dominated by the electromagnetic photon exchange which is completely independent from the electron polarization. Even in the kinematic regime, where $Z^0$ exchange contributes to the neutral current cross section, the polarization dependence is small. In the statistical method used to set limits on the existence of leptoquarks this fact is exploited by attributing larger statistical weight to those datasets and kinematic regions, where the signal process is enhanced due to its chiral coupling.

At the planned ILC it is foreseen to use polarized electron and positron beams. This will serve as an important tool in precision measurements of the Standard Model (for example properties of the $Z^0$ boson) or the analysis of physics beyond the Standard Model. Polarization will for example permit to distinguish between the production of left- and right-handed selectrons[1] by selecting the appropriate spin configuration of the $e^+e^-$ interaction. An extensive study of the advantages of polarized beams in $e^+e^-$ collider experiments has been presented in [11].

There are many techniques to measure the polarization of electrons. For the use in a collider experiment, however, only Compton polarimetry is feasible. As opposed to other methods it does not require the collision of electrons with a fixed target, thus destroying the beam, but relies on the scattering of laser photons off the beam leaving the majority of the electrons undisturbed.

### Compton Polarimetry

A generic Compton polarimeter design is shown in figure 1.1. At the Compton interaction point the incident electron beam is scattered off photons from a laser with known polarization. In Compton scattering the energies of both the scattered electron and photon depend on the product of their polarizations. This is shown in figure 1.2, for the cases $\mathcal{P}_e \cdot \mathcal{P}_\gamma = \{-1, 0, 1\}$. In the generic polarimeter layout (figure 1.1) the scattered electrons are separated from those beam electrons that did not participate in the Compton scattering by a spectrometric magnet. The recoil electrons' energy spectrum is thus

[1] the supersymmetric partner of the electron

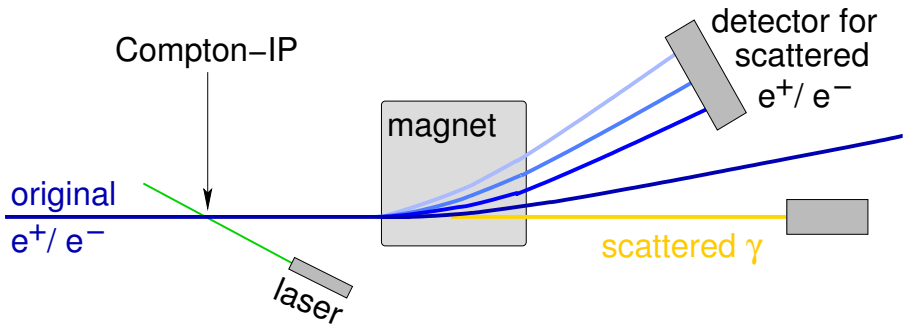


***Figure 1.1.:*** *Generic layout of a Compton polarimeter.*

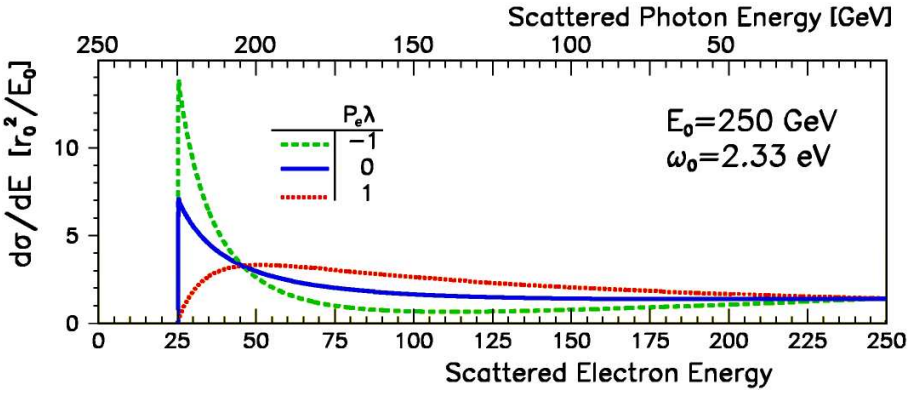


***Figure 1.2.:*** *Polarization dependent differential Compton cross section for different polarization configurations: $P_e$ and $\lambda$ are the incident electron and photon polarizations, respectively. The cross section is shown dependent on the energies of the outgoing electron and photon. The initial electron and photon energies are $E_0 = 250\,\mathrm{GeV}$ and $\omega_0 = 2.33\,\mathrm{eV}$, respectively. From [12].*

transformed into a spatial distribution, which is measured with an electron detector. Since the laser light polarization is known, the recoil electrons' spatial spectrum (and thus their energies) can be used to determine the initial beam polarization. However, the polarization is usually determined from an asymmetry measurement by flipping the laser polarization between $+1$ and $-1$. This allows for more precise measurements, as the energy, at which the event rates are equal (cf. figure 1.2), and the asymmetry is zero, can be determined very exactly.

An alternative way to measure the beam polarization with Compton scattering is the detection of the recoil photons. In this case, no spectrometric magnets can be used, and the measurement has to rely on direct energy measurements of many cumulated Compton scattering events. This is a less precise approach than the measurement of the spatial asymmetry of the scattered electrons described above. Compton polarimetry will be described in more detail in chapter 7.

### Hadron-Elektron-Ring-Anlage HERA

HERA was situated at DESY (*Deutsches Elektronen-Synchrotron*) in Hamburg. It was planned in order to study the substructure of the proton and properties of the strong interaction, and was the only accelerator facility to use electron (or positron) and proton beams.

The circumference of the HERA ring was 6.3 km. Electrons were accelerated to an energy of 27.5 GeV, and protons to an energy of 920 GeV. In the two experiments, H1 and ZEUS, both beams were brought into collision resulting in an $ep$ center-of-mass energy of 320 GeV. In the HERA-2 runperiod between 2003 and 2007 the $e^{\pm}$ beams were longitudinally polarized up to 45%.

When electrons are fed into the HERA ring they are unpolarized. However, due to the *Sokolov-Ternov effect* [13] they gradually become transversely polarized. When electrons move in a bent orbit around the storage ring they emit synchrotron radiation. In a homogeneous magnetic field such as that used to guide the electrons around the HERA ring, the electron spins will be aligned along the field lines. It has been found by Sokolov and Ternov that a small fraction of emitted synchrotron radiation photons will cause the electron spin to flip between 'up' and 'down'. It has further been shown that the probabilities for up-to-down and down-to-up transitions are not identical, thus resulting in a build-up of transverse polarization of the electrons circling the HERA ring. Over time electrons (positrons) will become anti-parallel (parallel) aligned to the external magnetic field. The time dependence of the electron polarization is given by $\mathcal{P}(t) = \mathcal{P}_{\max}(1-e^{t/\tau})$, with $\mathcal{P}_{\max}$ denoting the maximum attainable polarization, which in a planar storage ring and neglecting depolarization effects is $\approx 92.4\%$. At HERA, the time constant $\tau = 40\,\text{min}$, reflecting the small probability of spin flips in synchrotron radiation processes which appear every 10 ns.

For the study of polarization effects in electroweak interactions, only longitudinal polarization is relevant. When it had been ensured during the first HERA runperiod that a stable transverse polarization could be obtained, it was decided to install spin rotators to transform transverse polarization into a longitudinal one for the HERA-2 runperiod. These spin rotators consist of a sequence of interleaved horizontal and vertical bending magnets. They have been installed in front of the major experiments H1 and ZEUS. Additional spin rotators have been installed behind the $ep$ interaction points, since in order to maintain the beam polarization via the Sokolov-Ternov effect it is necessary to reinstall the transverse polarization. The spin rotators in front of and behind the HERMES interaction point have already been present during the HERA-1 runperiod. A schematic can be found in figure 1.3. In order to measure the beam polarization two Compton polarimeters were used: the transverse (TPOL) and longitudinal polarimeter (LPOL). The transverse polarization measurement makes it necessary to record a double asymmetry, since the cross section for transversely polarized electrons in Compton scattering also depends on the azimuthal angle. Due to spatial limitations the LPOL could not measure the recoil electron spectrum but had to use a multi-photon energy asymmetry. Thus, both polarimeters were limited in their capacities and achieved a

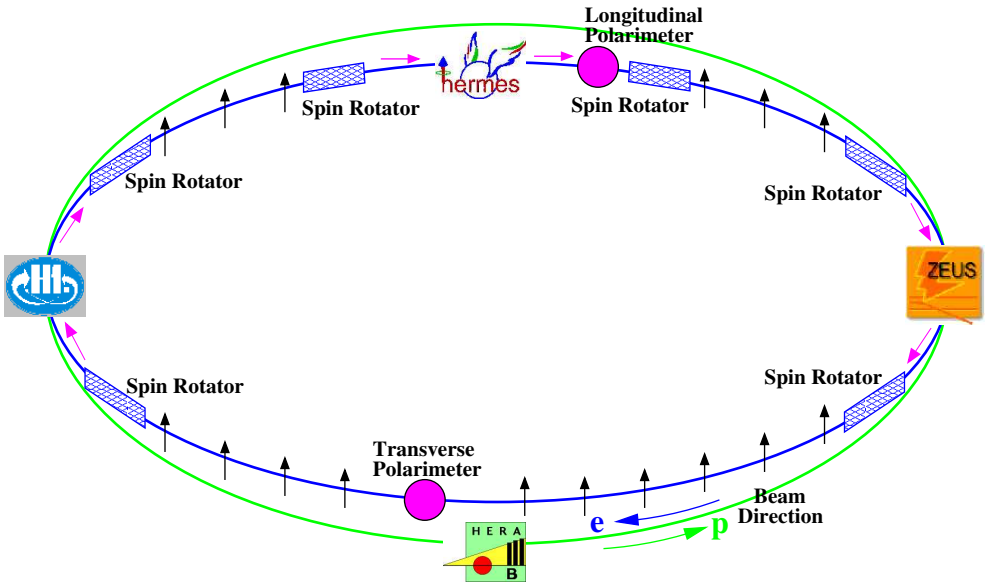


***Figure 1.3.:*** *Electron spin configuration and polarimeters at HERA.*

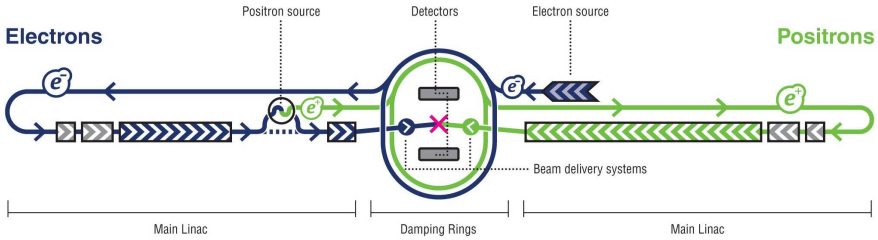


***Figure 1.4.:*** *The International Linear Collider [15].*

precision of $\Delta\mathcal{P}/\mathcal{P} = 3.4\%$ [14].

## International Linear Collider ILC

The ILC is a planned electron positron collider. It is generally perceived as a precision instrument to analyze the possible new phenomena discovered at the Large Hadron Collider (LHC). At the ILC the initial state is very clean and the initial conditions are very precisely known, enabling precision studies of new particles and their interactions. In addition, the ILC is foreseen to use polarized electron (80% or 90%), and positron beams (at least 30%, up to 60%).

A schematic of the ILC can be found in figure 1.4. The ILC is planned to be some 30 km in length, colliding electrons and positrons under an angle of 14 mrad at one central interaction point at a frequency of 5 Hz. The beams will consist of 1 ms long *bunch trains*, which in turn contain of the order of 1000 particle *bunches* with $\approx 10^{10}$

electrons or positrons in each. The center-of-mass energy is currently planned to be tunable between 200 and 500 GeV. At 500 GeV a peak luminosity of $2 \cdot 10^{34}\,\mathrm{cm}^{-2}\,\mathrm{s}^{-1}$ is to be reached.

An extensive description of the current design status of the ILC has been published in the Reference Design Report [16], and shall not be discussed further herein. Important in the scope of this analysis is the fact that it is planned to use polarized electron and positron beams, with a anticipated polarization of 80% and 30%, respectively.

Since at a linear collider, no synchrotron radiation is emitted the Sokolov-Ternov effect cannot be used to achieve the beam polarization. Instead, already the electron source has to be capable of producing highly polarized electrons with $\mathcal{P}_{e^-} \geq 80\%$ by irradiating pulsed laser light on a photocathode consisting of a strained GaAs/GaAsP superlattice structure. In addition, the laser helicity can be flipped from bunch train to bunch train, thus allowing for a fast reversal of the electron polarization. The positrons are produced via $e^{\pm}$ pair production. The electron beam passes through a helical undulator producing a high energy circular polarized photon beam that strikes a thin metal target. The produced positrons will have an initial polarization of at least $\mathcal{P}_{e^+} \geq 30\%$. An upgrade option to $\mathcal{P}_{e^+} \geq 60\%$ exists.

The polarization is to be measured by four Compton polarimeters: one upstream, one downstream of the interaction point, for each beam. The polarimeters will use the Compton recoil electrons, whose energy spectrum is transformed into a spatial distribution by a magnetic chicane. The spatial distribution is then measured by a Cherenkov hodoscope. A detailed description will be given in chapter 7.

In order to fully exploit the potential in searches for new phenomena, it is aimed to achieve an as yet unequaled precision of $\Delta\mathcal{P}/\mathcal{P} = 0.25\,\%$. So far the most precise polarization measurement was done at the $e^+e^-$ collider SLAC in Stanford, where $\Delta\mathcal{P}/\mathcal{P} = 0.5\,\%$ was achieved. A similar polarimeter design was used. The precision was found to be limited only by systematics. The linearity of the photodetectors in the Cherenkov detector was identified in particular as one of the crucial issues. The second part of this thesis (page 87ff) is dedicated to this and presents methods to measure photodetector nonlinearities at the permille level.

## Overview of this Thesis

**The first part** of this thesis presents a search for leptoquarks in data recorded by the H1 experiment during the HERA-2 runphase. After the basic physics processes are introduced in chapter 2, an overview of the H1 detector is given (chapter 3). The dataset on which the analysis has been performed is introduced in chapter 4. The data collected during the HERA-2 runperiod has been split into subsamples according to the helicity of the beam leptons in order to enhance the sensitivity to the presence of leptoquarks in the data. The search for leptoquarks is performed on datasets of neutral and charged current events, whose selection is described in chapter 5. Finally, chapter 6 presents the calculation of exclusion limits on these hypothetical particles.

**The second part** of this thesis is dedicated to the development of methods to measure photodetector nonlinearities to the subpercent level. This is done with regard to an ILC polarimeter whose precision will mainly be limited by systematic uncertainties like the detector nonlinearities. Chapter 7 gives an introduction to the planned Compton polarimeter, while in chapter 8 the basic principles of photodetectors and analog-to-digital converters are explained. In chapter 9 the test facility that has been assembled for the measurements of this thesis is presented. Finally, the actual photodetector nonlinearity measurements are described in chapter 10.

A summary of the results of both parts of this thesis and an outlook is given in the final chapter.

# Part I.

# Search for First Generation Leptoquarks at H1

# Chapter 2.

# Physics at HERA

This chapter gives an overview of the physics processes studied at HERA. The central process is the deep inelastic electron[1] proton scattering. Neutral and charged current reactions are introduced, because they form the basis for the search for leptoquarks presented in this thesis. Background processes to these events are explained. Finally the Buchmüller-Rückl-Wyler (BRW) model of leptoquarks is introduced.

## 2.1. Deep Inelastic Scattering

The HERA accelerator and its major detectors H1 and ZEUS have primarily been built in order to study the strong force and the structure of the proton in deep inelastic electron proton scattering processes (DIS). With the electron being a true elementary particle, this is equivalent to the elastic scattering of electrons on the proton's constituents, the quarks.

An interaction between electron and quark can only happen through the electroweak interaction, since the electron cannot partake in the strong interaction. Two types of processes are distinguished depending on whether a neutral or charged particle is exchanged between electron and quark. In the former case, a photon or a $Z^0$ boson is exchanged. In the latter, a $W^+$ or $W^-$ boson is exchanged depending on the charge of the beam lepton. In this case, the weak isospin of both particles changes and the final states consist of the electron's and quark's respective doublet partners. A schematic of both processes can be found in figure 2.1.

Since a large amount of momentum can be transferred in this reaction, the struck quark will leave the proton. Due to the confinement of the strong interaction the quark hadronizes, and is visible to the detector as a shower of particles, a *jet*. Only little momentum is transferred to the proton remnant, and it leaves the detector through the beam pipe, or causes activity in the very forward detectors. In figure 2.1 both the struck quark and the proton remnant are summarized as the hadronic system $X$.

The kinematics of DIS are often described in terms of three variables: $Q^2$, $x$, and $y$. If $k$, $k'$ are the four-momenta of the incident and outgoing leptons, respectively, and $P$

[1] Unless noted otherwise, the term *electron* refers to both electrons and positrons throughout this part of the thesis.

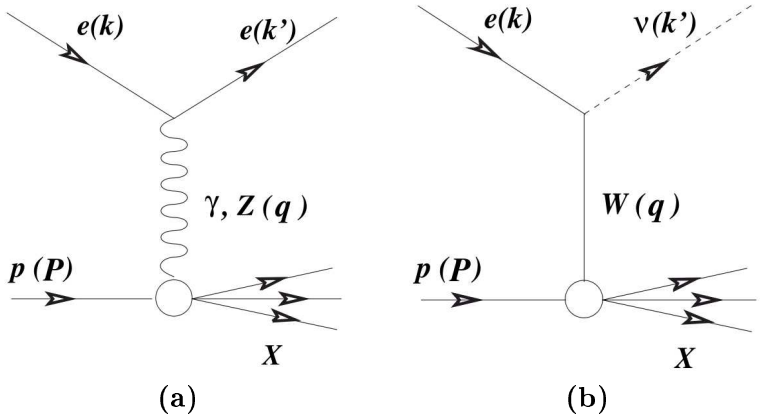


***Figure 2.1.:*** *Deep inelastic scattering: (a) neutral current; (b) charged current, from [17].*

the four-momentum of the initial proton, the gauge boson carries the four-momentum $q = k - k'$ (cf. figure 2.1).

The squared momentum transfer $Q^2$ corresponds to the virtuality of the gauge boson and is defined as

$$Q^2 = -q^2 = -(k - k')^2 \tag{2.1}$$

In the proton rest frame the inelasticity $y$ quantifies the amount of energy transferred from the electron to the hadronic system:

$$y = \frac{P \cdot q}{P \cdot k} \tag{2.2}$$

In the proton rest frame $y$ can also be expressed in terms of the angle between incident proton and outgoing lepton $\theta'$: $y = \frac{1}{2}(1 - \cos\theta')$.

The Bjorken scaling variable $x$ describes the fraction of the proton momentum carried by the struck quark:

$$x = \frac{Q^2}{2P \cdot q} \tag{2.3}$$

Finally, the squared center-of-mass energy $s$ is often used:

$$s = (P + k)^2 \approx 4E_e E_p \tag{2.4}$$

with $E_e$ and $E_p$ denoting the energies of electron and proton, respectively. For the approximation the masses of electron and proton have been neglected.

These four variables are connected via the relation

$$Q^2 = xys \tag{2.5}$$

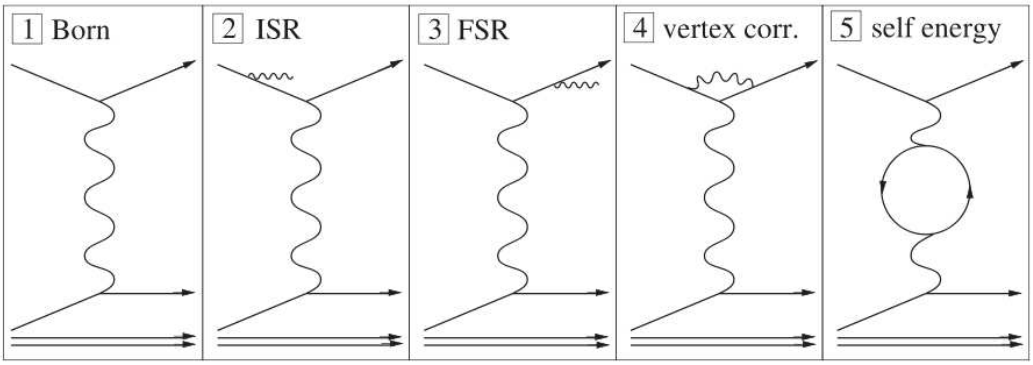


***Figure 2.2.:*** *Electroweak radiative corrections, from [17].*

### Electroweak Radiative Corrections

In the previous section the deep inelastic scattering has only been discussed at the Born level. However, in reality QED radiative effects will occur, and have to be taken into consideration. At the leading order, these originate from the emission of *soft* (low energetic) photons, that cannot be resolved in the detector. Both the electron and quark may emit these photons. In case the photon is radiated from an incoming particle this phenomenon is called *Initial State Radiation* (ISR). If the photon originates from the outgoing electron or quark, it is referred to as *Final State Radiation* (FSR). In addition to this, a combination of both (*vertex correction*) and internal loops can appear. These processes are depicted in figure 2.2. It has been shown [18] that the radiative effects from the quark are an order of magnitude smaller than those from the electron, and can be neglected. In case of ISR and FSR, for example, the energy $E_e$ of the incident electron is lowered, as is the energy $E'_e$ of the scattered electron, that is measured in the detector. Thus, if the values of the kinematic variables $Q^2$, $x$, and $y$ are calculated using $E_e$ and $E'_e$ they will be different from the true values in the electron-quark interaction. The reconstruction of the kinematic variables of DIS will be discussed in section 4.2.1. Radiative corrections will also be taken into account when calculating the cross sections for the generation of a leptoquark signal (section 6.2).

## 2.2. Neutral and Charged Current Cross Sections

Since they play an important role in the search for leptoquarks described in this thesis, this section discusses the two DIS processes, neutral and charged currents, in more detail. The polarization dependence of the cross sections is of particular importance for this analysis.

### 2.2.1. Neutral Current Cross Section

In case of unpolarized particles the neutral current cross section for the electroweak processes (including $Z$ exchange) $e^{\pm}p \to e^{\pm}X$ is given by

$$\frac{d^2\sigma^{\pm}_{\mathrm{NC}}}{dxdQ^2} = \frac{2\pi\alpha^2}{x}\left(\frac{1}{Q^2}\right)^2 \phi^{\pm}_{\mathrm{NC}}(x, Q^2) \tag{2.6}$$

with $\alpha = e/4\pi$ denoting the electromagnetic coupling constant. This equation shows the $Q^{-4}$ dependence typical for the elastic (Rutherford) scattering of point-like charged particles. The information about the internal structure of the proton and the fermion boson couplings are provided by the so-called *reduced neutral current cross section*

$$\phi^{\pm}_{\mathrm{NC}} = Y_+\tilde{F}_2^{\pm} \mp Y_- x\tilde{F}_3^{\pm} - y^2\tilde{F}_L^{\pm} \tag{2.7}$$

The *helicity factor* $Y_{\pm} = 1 \pm (1-y)^2$ represents the helicity dependence of electroweak interactions.

The longitudinal structure function $\tilde{F}_L$ describes the absorption of a longitudinally polarized vector boson. It is negligible for low $y$ and high $x$ and $Q^2$.

The generalized structure functions $\tilde{F}_2^{\pm}$ and $x\tilde{F}_3^{\pm}$ not only contain information about the parton structure of the proton, but they also accommodate for the fact that the neutral current process can be mediated by two different gauge bosons. The total cross section depends on the squared sum of the amplitudes of the photon and $Z^0$ exchange.

$$\tilde{F}_2^{\pm} = F_2 - (v_e \pm \mathcal{P}_e a_e)\kappa_Z F_2^{\gamma Z} + (v_e^2 + a_e^2 \pm \mathcal{P}_e v_e a_e)\kappa_Z^2 F_2^Z \tag{2.8}$$

$$x\tilde{F}_3^{\pm} = -(a_e \pm \mathcal{P}_e v_e)\kappa_Z x F_3^{\gamma Z} + (2v_e a_e \pm \mathcal{P}_e(v_e^2 + a_e^2))\kappa_Z^2 x F_3^Z \tag{2.9}$$

with the $Z$ propagator provided by $\kappa_Z = \frac{1}{4\sin^2\theta_W \cos^2\theta_W}\frac{Q^2}{Q^2+M_Z^2}$, and $v_e$ ($a_e$) denoting the electrons (axial-)vector coupling to the $Z$ boson. The structure functions $F_2$, $F_2^Z$, and $F_2^{\gamma Z}$ contain the information on the parton content of the proton and describe the pure photon exchange, the pure $Z$ exchange, and the interference between both, respectively. For a large part of the kinematic domain covered by HERA, neutral current processes are mediated predominantly through a photon. Only at $Q^2 \gtrapprox M_Z^2 \approx 8000\,\mathrm{GeV}^2$ does the $Z$ exchange become the dominating contribution to the cross section. However, both $Z$ exchange and interference terms have noticeable effects already at intermediate $Q^2$.

Via the generalized structure functions in equations 2.8 and 2.9 the neutral current cross section depends on the longitudinal lepton polarization:

$$\mathcal{P}_e = \frac{N_+ - N_-}{N_+ + N_-} \tag{2.10}$$

where $N_+$ and $N_-$ are the number of right and left-handed electrons or positrons in the beam.

### 2.2.2. Charged Current Cross Section

The charged current cross section for the processes $e^{\pm}p \to \overset{(-)}{\nu} X$ is given by:

$$\frac{d^2\sigma^{\pm}_{\mathrm{CC}}}{dxdQ^2} = (1 \pm \mathcal{P}_e)\frac{G_F^2}{2\pi x}\left(\frac{M_W^2}{Q^2 + M_W^2}\right)^2 \phi^{\pm}_{\mathrm{CC}}(x, Q^2) \tag{2.11}$$

There are some obvious differences to the neutral current cross section (equation 2.6): The fine structure constant is replaced by the Fermi coupling constant $G_F$. The propagator is modified to accommodate for the massive gauge boson. This propagator already shows that for $Q^2 \ll M_W^2$ the charged current cross section is much smaller than the neutral current cross section. Finally, there is a linear dependence of the cross section on the lepton polarization $\mathcal{P}_e$.

The *reduced charged current cross section* is defined like in the neutral current case:

$$\phi^{\pm}_{\mathrm{CC}} = \frac{1}{2}(Y_+\tilde{W}_2^{\pm} \mp Y_- x\tilde{W}_3^{\pm} - y^2\tilde{W}_L^{\pm}) \tag{2.12}$$

### 2.2.3. Comparison of NC and CC Cross Sections

Due to the fact that charged currents are only possible via the exchange of a massive boson, their cross section is much smaller than the neutral current cross section over a wide range of $Q^2$. This can be seen in figure 2.3 which shows a comparison of the $Q^2$ dependence of the total NC and CC cross sections measured at H1. Furthermore, these results beautifully demonstrate electroweak unification. For $Q^2 \lessapprox 2000\,\mathrm{GeV}^2$ the neutral current cross section is entirely dominated by the electromagnetic photon exchange, and the cross section is several orders of magnitude larger than the purely weak CC cross section. However, for $Q^2 \to M_{W,Z}^2$ electromagnetic and weak contributions become of similar size. It is notable, that the charged current cross section for electrons is generally larger than for positrons. In case of $e^-p$ reactions the exchanged $W$ boson couples to quarks with positive charge (up-type quarks), which have a larger density in the proton than the down-type quarks. This effect is observable for neutral current processes, as well, though only at large values of $Q^2$, for which the cross section is dominated by weak interactions.

#### Polarization Dependence

In the Standard Model, only left-handed fermions and right-handed antifermions partake in the charged current processes. For a lepton beam with right- and left-handed fermions, resulting in an average polarization of $\mathcal{P}_e$ (cf. equation 2.10) the Standard Model predicts a linear polarization dependence of the charged current cross section (cf. equation 2.11). This behavior has been experimentally verified at H1, which is shown in figure 2.4. It can also be seen from the plot that the extrapolated behavior for $\mathcal{P}_{e^-} \to +1$ and $\mathcal{P}_{e^+} \to -1$ is in agreement with the Standard Model predictions

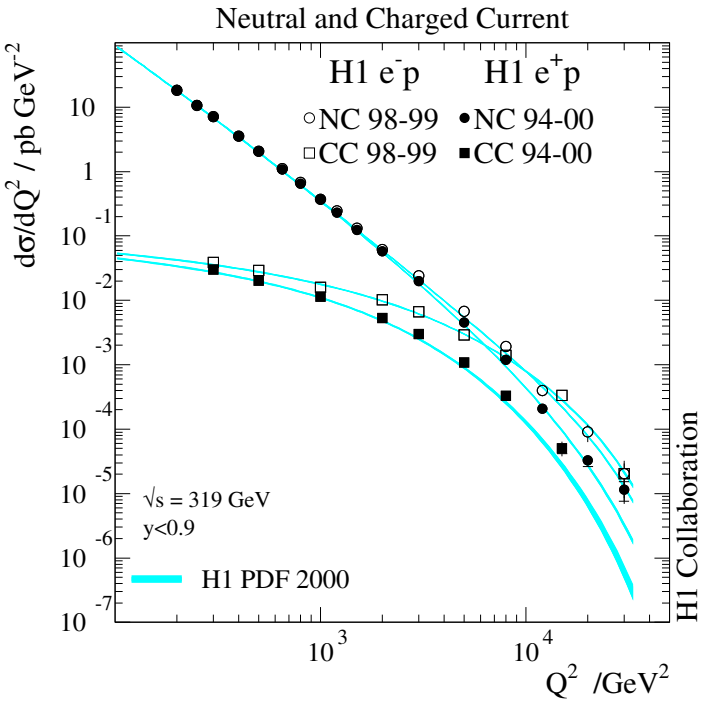


***Figure 2.3.:*** *The $Q^2$ dependence of the neutral and charged current cross sections as measured by H1, from [19].*

of vanishing charged current interactions for right-handed fermions and left-handed antifermions, respectively.

The polarization dependence of the neutral current cross section is caused by the $\gamma Z^0$ interference term and the $Z^0$ exchange due to the chiral nature of the electroweak interaction. Since neutral current processes are dominated by the electromagnetic photon exchange over a large kinematic range, polarization effects are only visible at large values of $Q^2$. Figure 2.5 shows the influence of polarized leptons on the neutral current cross section. The polarization independent electromagnetic part of $\sigma_{\mathrm{NC}}$ is removed from the graphs.

## 2.3. Background Processes

Since this analysis depends on the selection of clean samples of neutral and charged current events, all other Standard Model processes that may occur in $ep$ collisions are called *background processes*. Some of these may be misidentified as a neutral or charged current event, and will be discussed in the following.

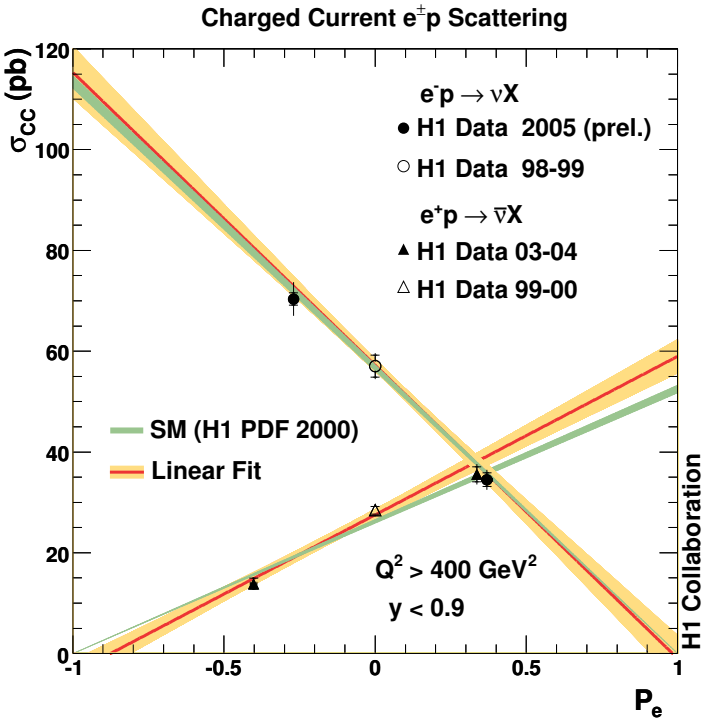


***Figure 2.4.:*** *Polarization dependence of the charged current cross section as measured by H1, from [20].*

## Photoproduction

This process occurs at a very low four momentum transfer $Q^2 \approx 0$. The electron proton interaction is mediated by a quasi-real photon. The cross section for this process is much larger than for charged and neutral current processes. A variety of different types of photoproduction processes exists. Figure 2.6(a) shows one example, the *direct* photoproduction. Due to the low $Q^2$ the scattered electron escapes through the beam pipe in most cases. However, a particle of the hadronic final state may be misidentified as the scattered electron thus faking a neutral current event. Photoproduction also contributes as background to charged current events, because the hadronic final state may contain neutrinos or muons with poorly measured momenta, thus leading to a final state imbalanced in transverse momentum. This fakes the typical charged current signature as will be further discussed in chapter 5.9.

## Lepton Pair Production

Figure 2.6(b) shows the dominant lepton pair production process at HERA. Both beam particles emit photons, which produce a lepton-antilepton pair ($e^+e^-$, $\mu^+\mu^-$, or $\tau^+\tau^-$). If one of these leptons escapes detection these events may be misidentified as neutral currents. If the scattered electron escapes under a very small angle through the beam

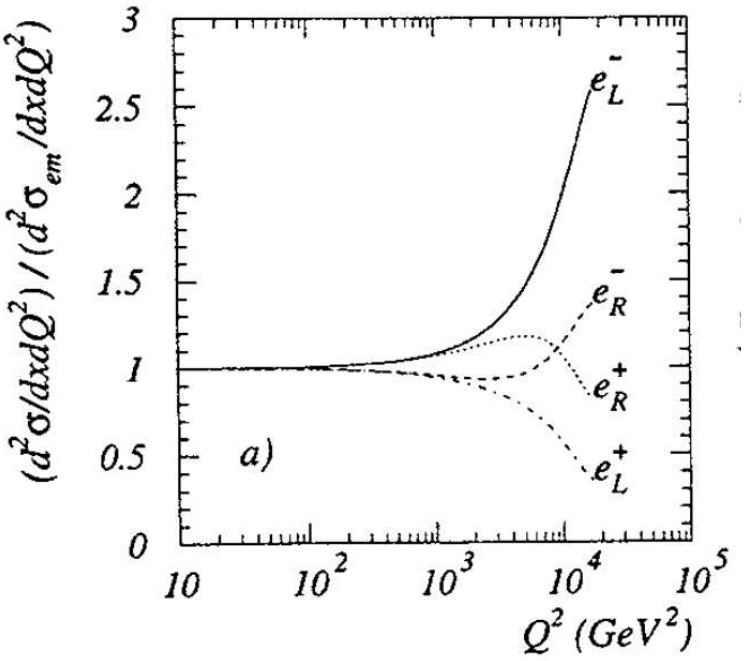


***Figure 2.5.:*** *Polarization dependence of the neutral current cross section: Purely electromagnetic contributions have been removed, from [21].*

pipe, these events may contribute to the charged current background. In case of $\mu$ or $\tau$ pair production similar misidentification issues exist as for photoproduction events, since their energy is not completely measured in the calorimeter.

#### Real $W^{\pm}$ Production

The production of real $W^{\pm}$ bosons at HERA is shown in figure 2.6(c). If the boson decays leptonically, and is not correctly reconstructed, these events may contribute to both neutral and charged current backgrounds. Especially, in the latter case this process has to be taken into account since the charged current cross section is only 50 times higher.

#### Wide angle bremsstrahlung

A Feynman diagram is shown in figure 2.6(d). This is only a minor background source to both neutral and charged current processes.

## 2.4. Leptoquarks in $ep$ Interactions

As already mentioned in chapter 1, the Standard Model is not a complete description of elementary particle physics. Especially the structural symmetry between the lepton and quark sector seems to hint to a more general order of elementary particles. In some

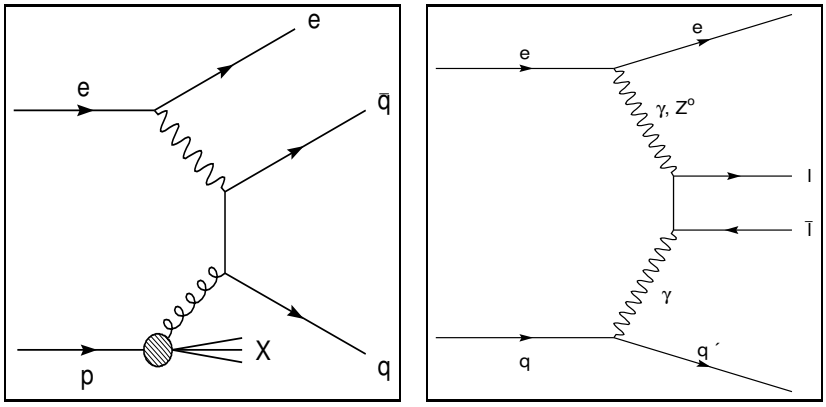


**(a)** direct photoproduction **(b)** lepton pair production

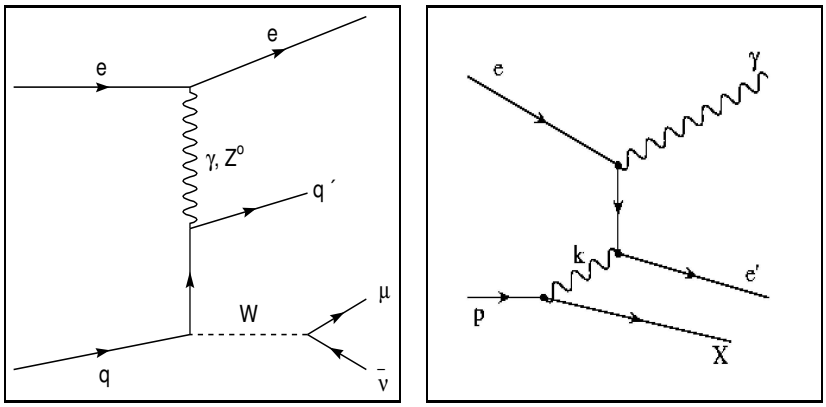


**(c)** real $W^{\pm}$ production **(d)** wide angle bremsstrahlung

***Figure 2.6.:*** *Standard Model background processes.*

extensions of the Standard Model, new particles are postulated that mediate transitions between both sectors. This analysis uses the model introduced by Buchmüller, Rückl, and Wyler to describe these *leptoquarks*.

## 2.4.1. The Buchmüller-Rückl-Wyler Model

By choosing a phenomenological ansatz the Buchmüller-Rückl-Wyler Model (BRW) model [24] is not limited to any specific extension of the Standard Model. It classifies all types of leptoquarks whose quantum numbers are not in conflict with experimental facts, like for instance the proton lifetime.

Since leptoquarks couple to both quarks and leptons, they carry color and a (fractional) electromagnetic charge. Both scalar and vector leptoquarks are possible, with spins 0 and 1, respectively. In order to classify these particles the *fermion number* $F$ is defined as:

$$F = |3B + L| \tag{2.13}$$

with baryon number $B$ and lepton number $L$. The fermion number can be either 0

or 2. Leptoquarks with $F = 2$ couple to lepton-quark and antilepton-antiquark pairs. Leptoquarks with $F = 0$ couple to antilepton-quark and lepton-antiquark pairs. In $ep$ interactions, like at HERA, leptoquarks could be produced in both $e^-p$ and $e^+p$ interactions. Since the proton's quark density is larger than its antiquark density (in the kinematic reach of this analysis), the $e^-p$ dataset will be more sensitive to leptoquarks with $F = 2$, and the $e^-p$ dataset to leptoquarks with $F = 0$.

Leptoquarks violating baryon or lepton numbers would have to be very heavy in order to avoid rapid proton decay. The proton mean life has been found experimentally to be at least $\tau > 1.9 \times 10^{29}$ years [22]. In order to realize quark masses detectable at HERA, the BRW model assumes baryon and lepton numbers conserving leptoquark couplings.

The effective Lagrangian with $SU(3) \times SU(2) \times U(1)$ invariant leptoquark couplings is:

$$\mathcal{L}_{\mathrm{LQ}} = \mathcal{L}_{F=2} + \mathcal{L}_{F=0} \tag{2.14}$$

with

$$\begin{aligned}\mathcal{L}_{F=2} =& \left(\lambda_L^{S_0} \bar{q}_L^c i\tau_2 l_L + \lambda_R^{S_0} \bar{u}_R^c e_R\right) S_0^\dagger + \left(\lambda_R^{\tilde{S}_0} \bar{d}_R^c e_R\right) \tilde{S}_0^\dagger + \\ & \left(\lambda_L^{\vec{S}_1} \bar{q}_L^c i\tau_2 \vec{\tau} l_L\right) \vec{S}_1^\dagger + \\ & \left(\lambda_L^{V_{1/2}} \bar{d}_R^c \gamma_\mu l_L + \lambda_R^{V_{1/2}} \bar{q}_L^c \gamma_\mu e_R\right) V_{1/2}^\dagger + \left(\lambda_L^{\tilde{V}_{1/2}} \bar{u}_R^c \gamma_\mu l_L\right) \tilde{V}_{1/2}^\dagger + \text{c.c.}\end{aligned} \tag{2.15}$$

and

$$\begin{aligned}\mathcal{L}_{F=0} =& \left(\lambda_L^{V_0} \bar{q}_L \gamma_\mu l_L + \lambda_R^{V_0} \bar{d}_R \gamma_\mu e_R\right) V_0^\dagger + \left(\lambda_R^{\tilde{V}_0} \bar{u}_R \gamma_\mu e_R\right) \tilde{V}_0^\dagger + \\ & \left(\lambda_L^{\vec{V}_1} \bar{q}_L \vec{\tau} \gamma_\mu l_L\right) \vec{V}_1^\dagger + \\ & \left(\lambda_L^{S_{1/2}} \bar{u}_R l_L + \lambda_R^{S_{1/2}} \bar{q}_L i\tau_2 e_R\right) S_{1/2}^\dagger + \left(\lambda_L^{\tilde{S}_{1/2}} \bar{d}_R l_L\right) \tilde{S}_{1/2}^\dagger + \text{c.c.}\end{aligned} \tag{2.16}$$

In these equations $q_L$ and $l_L$ denote the left-handed quark and lepton doublets, while $e_R$, $u_R$, and $d_R$ are the right-handed charged lepton and quark singlets. The superscript $c$ refers to a charge-conjugated fermion field. The leptoquarks are denoted with capital letters $S$ and $V$ referring to either scalar or vector leptoquarks with spins $J = 0$ or $J = 1$. The $\lambda_L^X$ signifies the Yukawa coupling of a leptoquark $X$ to a left-handed fermion.

The equations above, taken from [23], are modified from the original publication [24], in order to comply with the Aachen nomenclature [25], that is generally used in H1 publications on leptoquarks. In [24] only 10 types of leptoquarks are distinguished, with four of them coupling to both chiralities of leptons. However, these types of particles could mediate helicity unsuppressed leptonic two-body decays of the pion. From the experimental limit on $BR(\pi \to e\nu)$ it is deduced, that leptoquarks with masses accessible at HERA can only have either left- or right-handed couplings. In the Aachen notation these four types mentioned above are treated as separate particles with their left- or right-handed lepton coupling indicated by a superscript. For the purposes of this thesis, the resulting 14 types of leptoquarks, listed in table 2.1 are

used.

| $F = 2$ | | | | $F = 0$ | | | |
|---|---|---|---|---|---|---|---|
| LQ type | Dom. Prod. | Decay | $\beta_e$ | LQ type | Dom. Prod. | Decay | $\beta_e$ |
| Scalar Leptoquarks ($J = 0$) | | | | | | | |
| $S_{0,L}$ | $e_L^- u_L$ | $e^- u$<br>$\nu d$ | 1/2<br>1/2 | $S_{1/2,L}$ | $e_R^+ u_R$ | $e^+ u$ | 1 |
| $S_{0,R}$ | $e_R^- u_R$ | $e^- u$ | 1 | $S_{1/2,R}$ | $e_L^+ u_L$ | $e^+ u$ | 1 |
| $\tilde{S}_{0,R}$ | $e_R^- d_R$ | $e^- d$ | 1 | | $e_L^+ d_L$ | $e^+ d$ | 1 |
| $S_{1,L}$ | $e_L^- d_L$ | $e^- d$ | 1 | $\tilde{S}_{1/2,L}$ | $e_R^+ d_R$ | $e^+ d$ | 1 |
| | $e_L^- u_L$ | $e^- u$<br>$\nu d$ | 1/2<br>1/2 | | | | |
| Vector Leptoquarks ($J = 1$) | | | | | | | |
| $V_{1/2,R}$ | $e_R^- d_L$ | $e^- d$ | 1 | $V_{0,R}$ | $e_L^+ d_R$ | $e^+ d$ | 1 |
| | $e_R^- u_L$ | $e^- u$ | 1 | $V_{0,L}$ | $e_R^+ d_L$ | $e^+ d$<br>$\overline{\nu} u$ | 1/2<br>1/2 |
| $V_{1/2,L}$ | $e_L^- d_R$ | $e^- d$ | 1 | $\tilde{V}_{0,R}$ | $e_L^+ u_R$ | $e^+ u$ | 1 |
| $\tilde{V}_{1/2,L}$ | $e_L^- u_R$ | $e^- u$ | 1 | $V_{1,L}$ | $e_R^+ u_L$ | $e^+ u$ | 1 |
| | | | | | $e_R^+ d_L$ | $e^+ d$<br>$\overline{\nu} u$ | 1/2<br>1/2 |

***Table 2.1.:*** *The 14 different types of leptoquarks of the BRW model, in Aachen nomenclature. There are 7 types with fermion number $F = 2$, and 7 types with $F = 0$. Shown is also the dominant production process coupling to valence quarks. The branching ratio for decays into charged leptons is denoted by $\beta_e$.*

The leptoquarks are grouped according to their spin and their fermion number. Also given is the dominant production process which is the one involving the valence quarks of the proton. A leptoquark can always decay into a charged lepton and a quark. This could permit lepton flavor violation because the final state lepton does not have to be the same as the incident lepton. No evidence of the existence of such processes has yet been found[2]. In consequence this analysis is limited to *first generation leptoquarks*, i.e. leptoquarks coupling only to electrons, electron-neutrinos, up and down quarks, and their antiparticles. An analysis searching for lepton flavor violation mediated by leptoquarks is described in the PhD thesis of Matthias Janssen [23], as well as in several H1 and ZEUS publications like [26] and [27].

The production and decay channels given in table 2.1 already take into account the limitation to first generation leptoquarks. Thus, the decay channel into an $eq$ pair is open to all 14 types of leptoquarks. Four of them have an additional channel, which is a decay into a $\nu q'$ pair. In order to constrain the number of free parameters, it is assumed in the BRW model that the decay width for these four types is identical for

[2]for example: $\Gamma(\mu \to e\gamma)/\Gamma(\mu \to \text{all}) < 1.2 \cdot 10^{-11}$ and $\Gamma(\mu \to 3e)/\Gamma(\mu \to \text{all}) < 1.0 \cdot 10^{-12}$ [22].

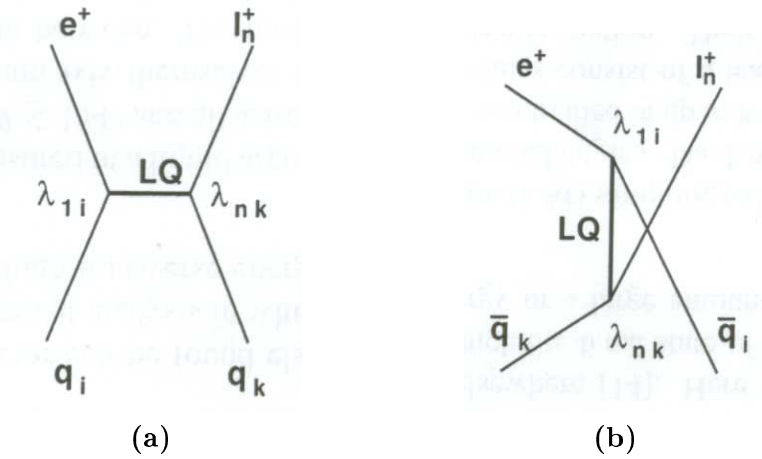


***Figure 2.7.:*** *Leptoquark processes in ep collisions: (a) s-channel production; (b) u-channel exchange. The indices denote lepton and quark generations. For first generation leptoquarks it is $i = n = k = 1$, from [28].*

both channels. This is expressed by $\beta_e = 1/2$, the branching ratio for an electronic decay. Hence, for each leptoquark type there are two free parameters in the BRW model: the mass $M_{\mathrm{LQ}}$ and the Yukawa coupling $\lambda$.

### 2.4.2. Experimental Signature

HERA offers the unique possibility to resonantly produce leptoquarks in $s$-channel $eq$ interactions. In addition to this a virtual leptoquark may be exchanged in the $u$-channel. Figure 2.7 shows Feynman diagrams for these processes in a generic form encompassing lepton flavor violation with the indices denoting lepton and quark generations. For the first generation leptoquarks analyzed in this thesis it is $i = n = k = 1$. The possible final states are either $eq$ or $\nu q'$. In the former case, the experimental signature in the detector will be an electron and one or several jets. For the latter leptoquark decay channel, one expects to observe one or more jets in combination with missing transverse momentum, caused by the neutrino escaping undetected. These experimental signatures are indistinguishable from Standard Model neutral and charged current processes. Evidence for the existence of leptoquarks can thus only be found statistically in quantities that are sensitive to the presence of these particles. For the further discussion the following Mandelstam variables are used:

$$\hat{s} = sx \tag{2.17}$$

$$\hat{u} = Q^2 - s \tag{2.18}$$

In the $s$-channel the leptoquark can be produced as a real particle with a mass that equals the center-of-mass energy in the electron-quark interaction: $M = \sqrt{\hat{s}}$. Because the quark can carry any fraction of the proton momentum ($0 < x \leq 1$), and due

to radiative processes that reduce the initial electron energy, $s$-channel production at HERA is possible at any mass up to the kinematic limit of $\sqrt{s_{ep}} = 320\,\mathrm{GeV}$. The decay widths $\Gamma_{S,V}$ for scalar and vector leptoquarks with masses well below the kinematic limit is expected to be small, and a narrow mass peak should be observable:

$$\Gamma_S = \frac{\lambda^2}{16\pi^2} M_{LQ} \tag{2.19}$$

$$\Gamma_V = \frac{\lambda^2}{24\pi^2} M_{LQ} \tag{2.20}$$

This corresponds to $\Gamma_S/M_{LQ} = \mathcal{O}(10^{-4})$ for a scalar leptoquark. In the narrow width approximation the resonant production cross section is

$$\sigma_{\mathrm{NWA}} \propto \lambda^2 q(x) \tag{2.21}$$

with $q(x)$ the parton density of the struck quark in the incident proton.

For leptoquark masses approaching the kinematic limit where $q(x)$ becomes very small, this is no longer valid. A strong distortion of the mass peak is caused by convoluting $q(x)$ with the Breit-Wigner resonance. This leads to large tails towards lower mass values. In addition, the interference of the $s$-channel production with the Standard Model neutral and charged current processes becomes noticeable. Both constructive and destructive interference terms are possible depending on the leptoquark type.

In approaching the kinematic limit, the contributions from off-shell $u$-channel exchange become more and more important, while being the only possible process for masses $M_{LQ} > \sqrt{s_{ep}}$. These events would have very broad mass distributions and would be concentrated at mass values much lower than $M_{LQ}$.

The mass spectrum is not the only distribution in which sizeable differences from Standard Model processes can be expected in case of the presence of a leptoquark signal. Differences in the angular distribution are expected as well. The Bjorken scaling variable, or inelasticity $y$ is related to $\theta^\star$, the polar angle of the outgoing lepton relative to the incident proton in the leptoquark rest frame, and is given by:

$$y = \frac{Q^2}{s_{ep} x} = \frac{1}{2}\left(1 + \cos\theta^\star\right) \tag{2.22}$$

For the dominating Standard Model process of neutral current $t$-channel photon exchange the differential cross section is

$$\left(\frac{d\sigma}{dy}\right)_\gamma \propto \frac{1}{y^2} \tag{2.23}$$

In contrast, scalar leptoquarks would be produced isotropically in their rest frame, while vector leptoquarks would have a characteristic $y$-dependence due to angular momentum

conservation, both of which are clearly different from $(d\sigma/dy)_\gamma$:

$$\left(\frac{d\sigma}{dy}\right)_S \propto 1 \tag{2.24}$$

$$\left(\frac{d\sigma}{dy}\right)_V \propto \left(1-y\right)^2 \tag{2.25}$$

Nota bene: These relation are only valid for $s$-channel production. In case of $u$-channel exchange, which becomes relevant for masses approaching the kinematic limit, the $y$-dependence is the other way round: flat for vector and $\propto (1-y)^2$ for scalar leptoquarks.

# Chapter 3.

# The H1 Detector

In this chapter a general overview of the H1 detector is given. Then the subsystems most relevant to this analysis are introduced.

## 3.1. General Overview

The H1 detector is shown in figure 3.1. It has been designed as a typical $4\pi$ multipurpose particle detector with a cylindrical symmetry around the beam pipe covering almost the entire solid angle.

The origin of the H1 coordinate system is located in the center of the detector. In H1 the flight direction of the incident proton defines the $z$-axis. The hemisphere given by the positive $z$-axis is called *forward* direction. Because of the much higher momentum of the proton the center-of-gravity of the $ep$ system moves in the forward direction, as do most particles originating from $ep$ collisions. This made it necessary to choose an asymmetric detector design with the forward region containing more instrumentation than the backward region.

The general layout of the detector follows the basic 'onion skin' design of high energy physics particle detectors. Centered around the beampipe [1] are the tracking detectors [2] and [3], that measure the trajectories and momenta of charged particles. They are followed by the electromagnetic [4] and hadronic calorimeters [5], where all particles, except for muons, are stopped and their energies are measured. The layout is completed by the superconducting coil [6] of the magnet, and the return iron yoke [10], which is instrumented as a muon detector [9].

In the following the components central to this analysis are introduced. A thorough description of the H1 detector can be found in [29], and on the official webpage [30], which is where the images shown herein are taken from.

## 3.2. Tracking Detectors

The tracking detectors are used to measure the trajectories of charged particles in the magnetic field provided by the superconducting coil. Thus, momenta and the sign of charge can be determined. The tracking system is divided into a forward, central and

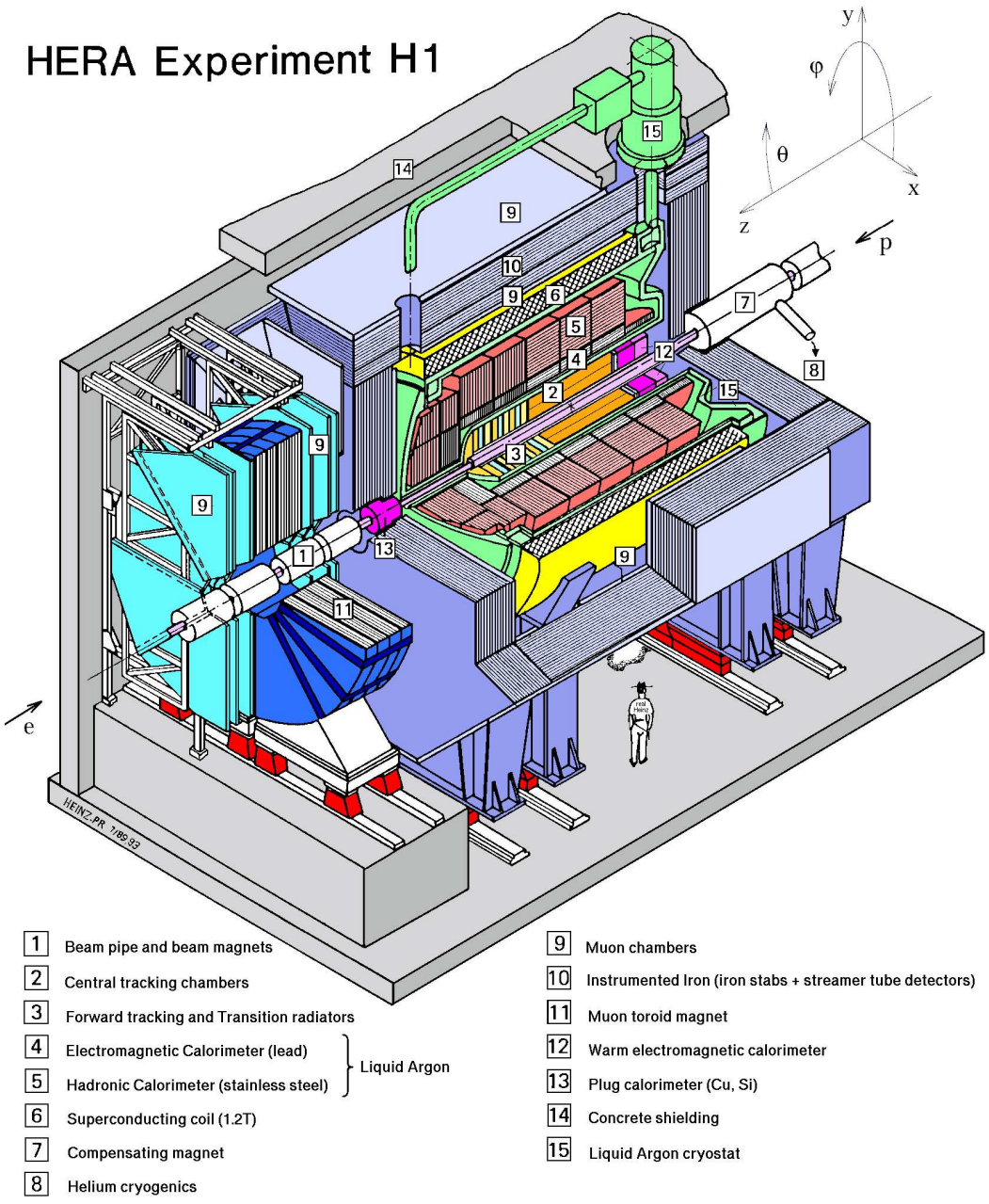


***Figure 3.1.:*** *The H1 Detector.*

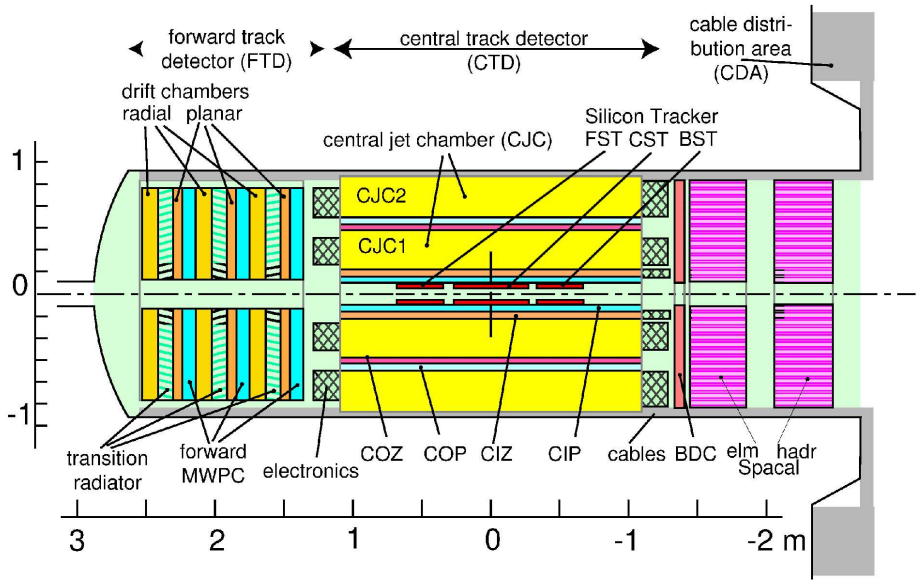


***Figure 3.2.:*** *Side view of the H1 tracking system. For the HERA-2 runperiod the CIZ and parts of the CIP were replaced by the CIP2k.*

backward part. Figure 3.2 shows a schematic overview. It consists of several multi-wire proportional chambers and silicon detectors. The main components of the central part are the Central Jet Chambers (CJC1 and CJC2), the Central Inner and Outer Proportional chamber (CIP and COP), the Central Outer Tracker Z-Chamber (COZ), and the Central Silicon Tracker (CST). The forward and backward parts are equipped with the Forward tracking Detector (FTD), the Forward Silicon Tracker (FST), the Backward Proportional Chamber (BPC), and the Backward Silicon Tracker (BST).

### 3.2.1. Central Tracking System

The central tracking detector (CTD) consists of five coaxial chambers. A sideview is shown in figure 3.3. The innermost component is the CST. It consists of two coaxial cylindrical silicon layers with 12 and 20 modules and a radius of 5.75 cm and 9.75 cm, respectively. It has an active length of 35.6 cm along the beam pipe, and provides the highest spatial resolution of all tracking detectors with $\sigma_{r\phi} = 14\,\mu$m while covering angles in the range of $30° < \theta < 150°$. The other four components of the Central Tracking Detector all consist of multi-wire proportional chambers. All of them have an extended angular coverage of $15° < \theta < 165°$. Next to the CST there is the CIP (or CIP2k), which is a replacement of the Central Inner Z-chamber and parts of the old CIP. The CIP has a diameter of $\approx 40$ cm and consists of five radial layers. Due to its high time resolution of $\approx 2\,\mu$s, it allows a fast determination of the $z$-position of the event vertex. For this reason it is suitable for background rejection and used for triggering.

Around the CIP there are the two central drift chambers (CJC1 and CJC2). The

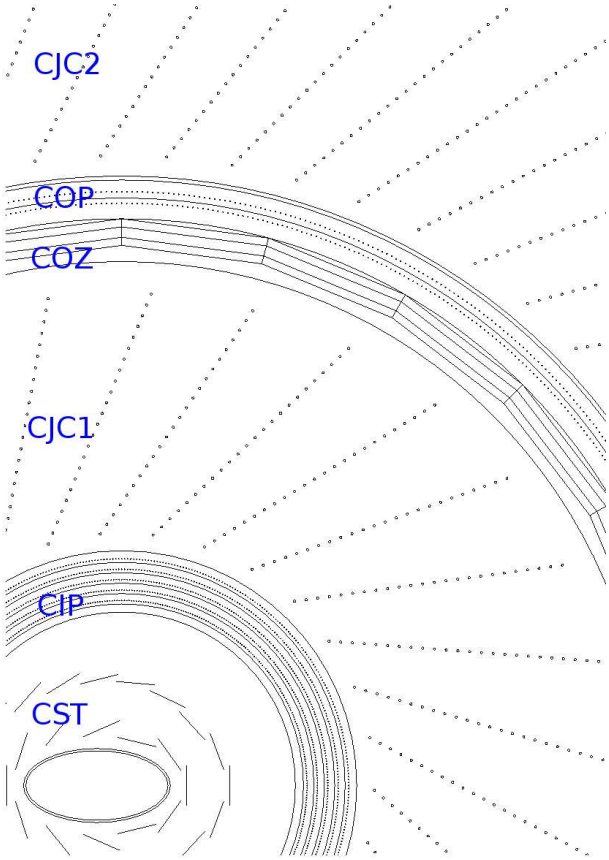


***Figure 3.3.:*** *Radial view of the H1 central tracking detector.*

CJC1 consists of 30 cells with 24 sense wires parallel to the beam axis. The CJC2 consists of 60 cells with 32 sense wires. The timing resolution is very high ($\sigma_t = 2\,\text{ns}$), which is why these chambers are used to remove events that do not appear at bunch crossing time (see section 5.1). These chambers offer a very good radial spacial resolution of $\sigma_{r\phi} = 170\,\mu\text{m}$. Since the CJCs' wires are parallel to the beam axis, their $z$-resolution is very limited ($\sigma_z = 22\,\text{mm}$), and is realized through charge division. The CJCs allow a transverse momentum measurement with a resolution of

$$\frac{\sigma(P_T)}{P_T} = 0.01 \cdot P_T/\text{GeV} \tag{3.1}$$

In order to compensate for the low $z$-resolution of the CJCs, the COZ is placed coaxial between both CJCs. The COZ's sense wires are perpendicular to the beam axis achieving a $z$-resolution of $\sigma_z = 350\,\mu\text{m}$. Finally, neighboring the COZ, the COP is situated. Like its the counterpart, the CIP, it offers a fast determination of the $z$-position of the event vertex and is used to trigger against background events.

### 3.2.2. Forward Tracking Detector

The Forward Tracking Detector (FTD) covers the angular region of $5° < \theta < 20°$ and consists of several drift chambers. These are grouped in three *Supermodules*, each built up of three planar $P$ and one or two $Q$ chambers. The $P$ chambers have four layers of wires each, and are tilted against the $y$-axis at angles of $-60°$, $0°$, and $60°$. The $Q$ chambers each consist of eight layers of wire, and are oriented at angles of $30°$ and $90°$. A schematic is depicted in figure 3.4.

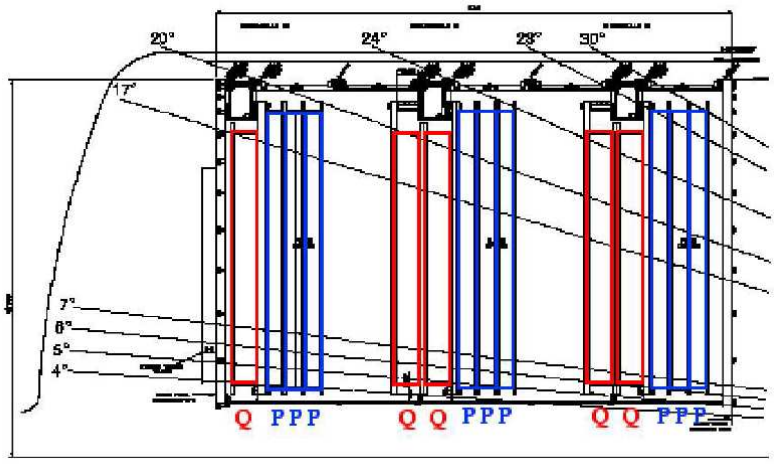


***Figure 3.4.:*** *Schematic of the H1 forward tracking detector.*

## 3.3. Calorimetry

The Liquid Argon Calorimeter (LAr) is the central calorimeter of H1, which covers the central and forward part of the detector within a range of approximately $4° < \theta < 154°$. The backward part of the detector is covered by the *Spaghetti Calorimeter* SpaCal ($153° < \theta < 174°$). The other two H1 calorimeters are the Plug ($0.7° < \theta < 3.4°$) and the Tail Catcher, which is part of the iron yoke's muon system.

### 3.3.1. Liquid Argon Calorimeter LAr

A schematic of the Liquid Argon Calorimeter (LAr) can be seen in figure 3.5. The LAr is built up of eight wheels with each wheel consisting of eight octants. This is necessary to provide space for support structures, power supply and readout cables. The LAr is divided into an inner, finer granulated electromagnetic and an outer hadronic part with an overall of 45000 readout cells. As a typical sampling calorimeter the LAr is built up of alternating layers of liquid argon at a temperature of 90 K as active medium and

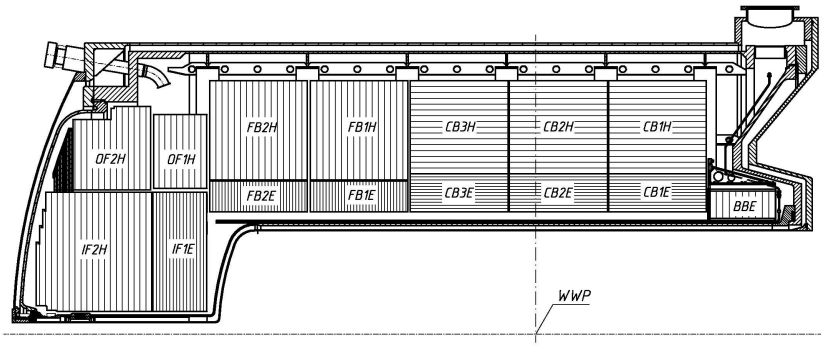


**(a)** side view upper part

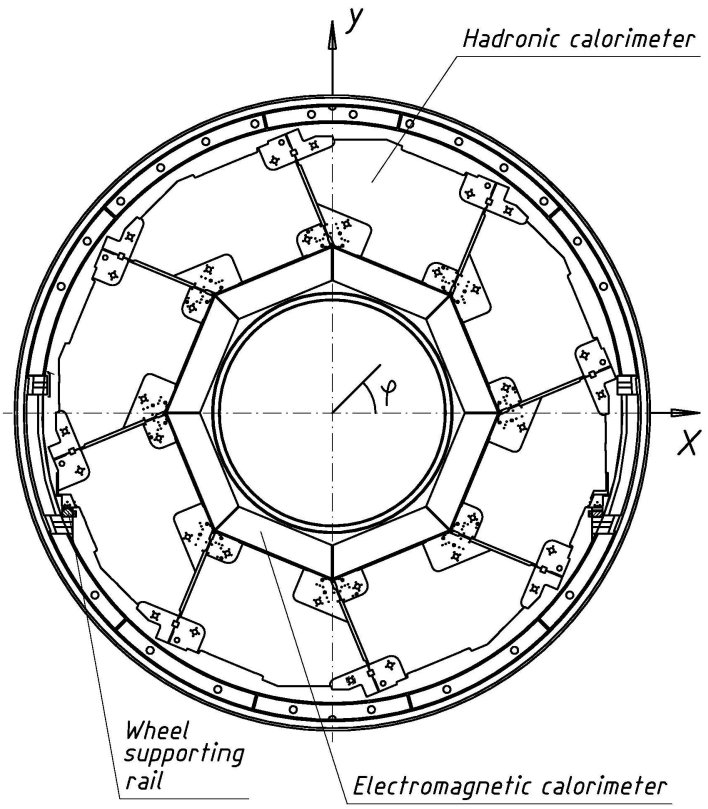


**(b)** radial view

***Figure 3.5.:*** *The Liquid Argon calorimeter.*

absorber plates. The absorber material in the electromagnetic part is lead and stainless steel in the hadronic section.

When a particle enters the calorimeter it interacts with the absorber material producing secondary particles. Thus, a shower or cascade is started that continues until the incident energy is absorbed. The energy deposited in the active material is measured. Electrons and photons interact with the absorber material mostly via bremsstrahlung and pair production, respectively. Hadrons scatter inelastically or elastically on the absorber nuclei.

The LAr is an example of a non-compensating calorimeter. This means that at the same input energy the signal of strongly interacting particles is smaller than that of electromagnetically interacting ones. This difference has to be corrected for during the data reconstruction.

The advantages of the LAr are good stability, easy calibration, homogeneity of response and high granularity. The drawback is the electronic noise pickup, because the recorded signals are not amplified within the calorimeter and have to be guided out of the detector over many meters of cable.

In testbeam measurements with electrons [31] and pions [32] at CERN the energy resolution has been determined to be:

$$\frac{\sigma(E)}{E} = \frac{11\%}{\sqrt{E/\mathrm{GeV}}} \oplus 1\% \quad \text{for electrons and photons} \tag{3.2}$$

$$\frac{\sigma(E)}{E} = \frac{50\%}{\sqrt{E/\mathrm{GeV}}} \oplus 2\% \quad \text{for hadrons} \tag{3.3}$$

### 3.3.2. Spaghetti Calorimeter

The Spaghetti Calorimeter (SpaCal) covers the very backward part of the detector. It is very important for analyses of processes involving a low momentum transfer $Q^2$ which leads to the electron being scattered under a small angle. At the very high values of $Q^2$ used in this analysis only events measured in the LAr are considered. In this analysis the SpaCal is only used to complement to the Time-of-Flight system to set veto conditions. Like the LAr, the SpaCal is a non-compensating calorimeter consisting of an electromagnetic and hadronic part. In contrast it does not use liquid argon as active material, but the particles are detected by scintillation in the eponymous fibers traversing the calorimeter.

## 3.4. Time-of-Flight System

The Time-of-Flight System (ToF) consists of three fast scintillation detectors that are positioned close to the beam pipe within or in the vicinity of the main detector: the backward ToF (BToF) at $z = -275\,\mathrm{cm}$, the forward ToF (FToF, $z = 540\,\mathrm{cm}$), and the Plug ToF (PToF, $z = 540\,\mathrm{cm}$). They are complemented by two veto walls at

$z = -810\,\text{cm}$ and $z = -650\,\text{cm}$. Due to the high time resolution of these detectors ($\approx 1\,\text{ns}$), the system is used to reject non-$ep$ background events, that is events not originating from an $ep$ interaction. Those events are for the most part not synchronized to the nominal HERA bunch crossing time.

## 3.5. Luminosity System

Since the luminosity is the link between the experimentally measured event numbers and the physically significant cross sections a precise luminosity measurement is the key to a correct interpretation of the data in high energy physics experiments. H1's luminosity system makes use the Bethe-Heitler bremsstrahlung process $ep \rightarrow ep\gamma$. This is a well known process with a large total cross section $\sigma_{\text{BH}}$ that can be precisely calculated within quantum electrodynamics (to a level of 0.5%). By counting the number of events $N_{\text{BH}}$ of this process the luminosity can be calculated from

$$\mathcal{L} = \frac{N_{\text{BH}}}{\sigma_{\text{BH}}} \tag{3.4}$$

The rate is measured by coinciding hits in the Photon Detector (PD, $z = -102.9\,\text{m}$) and the Electron Tagger (ET, $z = -33.4\,\text{m}$). During the HERA-2 runphase the precision was limited by systematical effects. Especially in the data taken in 2006 and 2007 some inconsistencies were observed so that at present the precision for this runperiod is $\Delta\mathcal{L}/\mathcal{L} = 4\%$. For other runyears the systematics are controlled better resulting in $\Delta\mathcal{L}/\mathcal{L} = 2\%$ for 2005, and $\Delta\mathcal{L}/\mathcal{L} = 1.3\%$ for 2003/04.

## 3.6. Trigger System

At HERA the electron and proton beams collide every 96 ns, corresponding to a rate of roughly 10 MHz. However, only a fraction of the events initiated by HERA contain 'interesting' physics. Considering the state of electronics hardware available in the late 80s and early 90s, when H1 was designed and built, an offline processing of the vast amount of information provided by the numerous subdetectors ($\approx$ 270000 channels) was impossible. Thus, an elaborate trigger system was envisioned in order to effectively (and traceably) reduce the number of undesirable or just abundant events with large total cross sections, while ensuring the recording of every rare process [29]. It is also imperative to minimize the dead time during data read-out and storage, in which no new events can be recorded. The H1 trigger system consists of several layers, which will be introduced in the following. A general overview is given in figure 3.6.

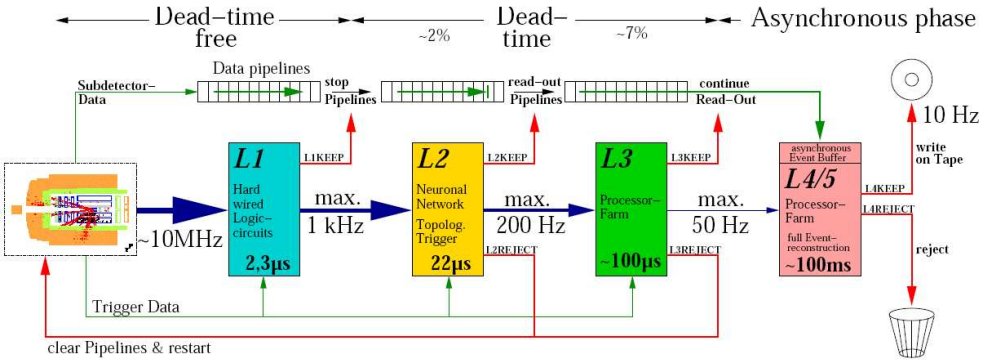


***Figure 3.6.:*** *Overview of the H1 trigger system.*

## 3.6.1. Trigger Level One (L1)

On the first trigger level [33] the event rate is reduced to about 1 kHz. The decision whether to reject or keep an event and pass it on to the next trigger level has to be reached within 24 BC (2.3 $\mu$s). During this time the information read from the subdetector systems is buffered in pipelines, so that dead time is avoided. To reach this fast decision, a subset of the data from different subdetectors is fed to fast hardwired logics, which are encoded in Boolean decisions (*trigger elements*). There are 256 trigger elements in L1, which are logically combined to up to 128 *raw subtriggers*. Most of these subtriggers check for signatures of various physics processes (*physics triggers*), some are used to monitor the subdetectors' performances and determine the efficiency of the physics triggers (*monitor triggers*). Subtriggers that may initiate a readout rate exceeding the limit of 1 kHz have to be prescaled. A prescale of $n$ means that the subtrigger is set only every $n$th time its condition is fulfilled. The subtriggers used in this analysis were not prescaled.

The L1 trigger decision is based on a logical `OR` of all subtriggers. This means if one subtrigger is set for a certain bunch crossing, the L1 trigger logic sends the `L1keep` signal. The pipelines are stopped and the corresponding event is passed on to the next trigger level. During this time the H1 detector is insensitive to any $ep$ events. As long as `L1keep` is not sent, the pipelines are being filled overwriting the oldest data if necessary.

## 3.6.2. Trigger Level Two (L2)

The second trigger level [34] further reduces the data rate to 200 Hz. It gets information from the subdetectors and has to validate the `L1keep` decision within 20 $\mu$s. It consists of two components: L2NN is a neural net trigger, that has been trained with samples of $ep$ and background events. The topological trigger L2TT utilizes a matrix representing the H1 detector. The trigger decision is based on a *distance to background* calculation.

If the event is rejected on L2, a signal (`L2reject`) is sent to the central trigger logic, and the pipelines are restarted, ending the dead time of the detector. If it is decided on L2 to keep the event (`L2keep`) the readout of the entire 270000 channels of the H1 detector is started.

### 3.6.3. Trigger Level Three (L3)

The third trigger level [35] has been installed during the HERA-2 upgrade as part of the Fast Track Trigger (FTT), that was designed to handle the high rates from the track triggers. L3 is software based, and makes use of a farm of RISCs[1]. Within 50 $\mu$s a decision is made to either clear and restart the pipelines (`L3reject`) or to continue the data readout. After the third trigger level a data rate of 50 Hz is achieved.

### 3.6.4. Final Trigger Level (L45)

Opposed to all three trigger levels described so far, the final trigger level is not synchronized to the HERA clock. On L45 (for Level Four and Five) a complete event reconstruction and classification is done on a dedicated computer farm. Once the central event builder of the data acquisition has collected all the information from H1's subdetectors, the event processing and reconstruction is started. At the same time the pipelines are restarted, thus ending the dead time of the detector that started with the `L1keep` decision. After the reconstruction the events are filtered according to potential interest. Events that cannot be associated to any category of $ep$ process are rejected (except for 1% that are kept for monitoring purposes). In addition, less 'interesting' events with abundant event rates are partly rejected in favor of rarer event types. Finally, all kept events are written to tape at a rate of about 10 Hz, and form the dataset recorded by H1.

[1] Reduced Instruction Set Computer: a simplified CPU design to achieve higher processing performance

# Chapter 4.

# Dataset and Monte Carlo Simulations

This section describes the dataset this analysis is run on. Furthermore, the Monte Carlo simulations are introduced, that are used to compare the selected data to Standard Model predictions.

## 4.1. The HERA-2 Dataset

This analysis is performed on the entire data recorded by the H1 detector during the runphase 2 of the HERA accelerator. This data was recorded in the years between 2003 and 2007. In this time period HERA has delivered about $550\,\mathrm{pb}^{-1}$ of integrated luminosity to the experiments. About $450\,\mathrm{pb}^{-1}$ thereof were recorded by H1. The H1 data taking is split up into periods of up to two hours during which beam and detector conditions can be assumed to be stable. These periods are called *runs*. The status of the different subsystems is constantly monitored, and it is recorded which detector components are fully operational, i.e. are supplied by high voltage. Since this analysis relies on certain subdetectors, it has to be ensured that they have been *on* for the entire data this analysis is performed on. For this reason a run selection is performed on the entire HERA-2 dataset. The detector components, already introduced in chapter 3, required to have been operational are:

- the central jet chambers CJC1 and CJC2
- the central inner proportional chamber CIP
- the liquid argon calorimeter LAr
- the time-of-flight system
- the luminosity detector
- the calorimeter triggers

| lepton type | $T = 1/2$ data set | $\mathcal{L}$ / pb$^{-1}$ | P / % | $T = 0$ data set | $\mathcal{L}$ / pb$^{-1}$ | P / % | $\sum\mathcal{L}$ / pb$^{-1}$ |
|---|---|---|---|---|---|---|---|
| $e^-$ | 05L | 68.0 | −27.1 | 05R | 30.1 | +36.8 | 153.0 |
| | 06L | 34.4 | −24.6 | 06R | 20.5 | +30.8 | |
| $e^+$ | 0304R | 24.5 | +33.5 | 0304L | 23.7 | −38.2 | 181.9 |
| | 0607R | 76.3 | +30.7 | 0607L | 57.4 | −35.5 | |
| $e-$ or $e+$ | | 203.2 | | | 131.7 | | 334.9 |

***Table 4.1.:*** *Data sets used in this analysis, grouped according to the beam lepton type and its weak isospin $T$.* $\mathcal{L}$*: integrated luminosity, P: average polarization of beam leptons*

Resulting from these subdetector requirements, the entire data set used in this search has an integrated luminosity of $335\,\mathrm{pb}^{-1}$.

HERA-2 used polarized lepton beams. Since the BRW model used in this analysis postulates chirally coupling leptoquarks, and the bulk of standard model background, the neutral current photon exchange, does not have a chiral coupling, the polarization of the beam leptons can be used to enhance the signal-to-background ratio. This is why the data has been split up according to the helicity and lepton type. Table 4.1 gives an overview of the integrated luminosity and beam (lepton) polarization used in this analysis. The data sets have been grouped according to the dominating weak isospin. These sets are especially sensitive to different types of leptoquarks, as will be discussed in chapter 6 on the limit calculations results.

## 4.2. Kinematic Reconstruction and Particle Identification

The raw data recorded by the H1 experiment consist of information like energy deposits in calorimeter cells, and hits in tracker elements. An extensive software package has to be applied in order to reconstruct the information needed for analyses like the particle identification, energies and momenta. In the following the focus is on the reconstruction of the kinematic variables defining a deep inelastic scattering (DIS) event and the identification of particles relevant to this analysis. It has to be pointed out that the principles and formulae presented in the following subsection are only valid at Born level. In *reality*, QED radiation effects appear that cannot be resolved by the detector, and have to be modeled. This has been discussed in section 2.1.

### 4.2.1. Kinematic Reconstruction

The most common variables used to define the kinematics of deep inelastic scattering (DIS) are the momentum transfer $Q^2$, the momentum fraction of the struck quark $x$,

and the inelasticity $y$. At the Born level they are related via:

$$Q^2 = xys \tag{4.1}$$

Ignoring radiative effects HERA's center-of-mass energy is fixed ($\sqrt{s} = 319\,\mathrm{GeV}$) and only two variables in 4.1 are independent. There are several ways to reconstruct these quantities from the information acquired by the experiment, that is energies and momenta of the hadronic final state, and, if present, the scattered electron.

### Electron Method

As the name suggests, this method [36] relies on the scattered electron. Two properties are used: the energy and the polar angle: $E'_e$ and $\theta_e$. With $E_e$ denoting the initial electron energy, momentum transfer and inelasticity can be calculated by:

$$Q^2_e = 4E_e E'_e \cos^2(\frac{\theta_e}{2}) \tag{4.2}$$

$$y_e = 1 - \frac{E'_e}{E_e}\sin^2(\frac{\theta_e}{2}) \tag{4.3}$$

Because of equation 4.1 the third DIS variable is:

$$x_e = \frac{Q^2_e}{s \cdot y_e} \tag{4.4}$$

The subscript $e$ of the three DIS variables signifies they were calculated using the electron method. This nomenclature will be used throughout this thesis.

Since both $E'_e$ and $\theta_e$ can be measured very precisely, the electron method provides very reliable information on both $Q^2_e$ and $y_e$. However, because of $\delta x_e/x_e = 1/y_e$ a good resolution in $x_e$ is limited to large values of $y_e$. This method is sensitive to radiative effects, since their dominating contribution comes from the electron. Furthermore, both $Q^2_e$ and $y_e$ directly depend on initial electron energy $E_e$, which is only known precisely at the Born level.

Despite these drawbacks, this method has been chosen for the reconstruction of neutral current events in this thesis, because of its excellent $Q^2_e$ and $y_e$ resolutions. In case of charged current events, for which the scattered electron is not available, all information has to be extracted from the hadronic final state.

### Hadron Method

This method was envisioned by Jacquet and Blondel [37]. It is the only method that exclusively uses properties of the hadronic final state, and is thus the only possibility to reconstruct charged current events. It uses the following quantities derived from the

hadronic final state:

$$\Sigma = \sum_i (E_i - P_{z,i}) \tag{4.5}$$

$$P_{T,h} = \sqrt{(\sum_i P_{x,i})^2 + (\sum_i P_{y,i})^2} \tag{4.6}$$

The summation includes all particles in the hadronic final state, that is all particles in the detector except for a possible scattered electron candidate. $P_{x/y/z}$ denotes the projection of a particle's momentum in the respective direction. As already mentioned in section 3.1, the direction of the incident proton is defined as $z$-axis, which means $x$ and $y$ are perpendicular to the beam axis. Thus $P_T$ is called *transverse momentum*.

With these definitions the kinematic variables can be written as (subscript $h$ denoting the hadron method):

$$Q^2_h = \frac{P^2_{T,h}}{1 - y_h} \tag{4.7}$$

$$y_h = \frac{\Sigma}{2E_e} \tag{4.8}$$

with $E_e$ being the initial electron energy. The third DIS variable is

$$x_h = \frac{Q^2_h}{s \cdot y_h} \tag{4.9}$$

The hadron method relies on a precise knowledge of the hadronic final state. It is often used, in combination with the electron method, to check hadronic calibrations and resolutions. The method does not use properties of the scattered electron which are affected much more by radiative effects than those of the hadronic final state. Thus it is little sensitive to radiative effects - especially when compared to the electron method - albeit not entirely insensitive since the energy of the incoming electron enters the calculations.

The $1/(1 - y_h)$ dependence in equation 4.7 causes a degradation of the $Q^2$ resolution for large values of $y$. It is therefore not used in neutral current analyses, but cannot be avoided for charged current selections.

Finally, a third method is introduced that uses an entirely different approach in that it is largely independent from calorimeter energy scales. It is therefore used for the calibration of energy measurements (cf. section 4.3).

### Double Angle Method

The kinematic reconstruction with the double angle method [36] is performed using the polar angles of the scattered electron $\theta_e$ and the struck quark $\gamma_h$. The latter is calculated from the hadronic final state under the assumption that the quark hadronizes to a single

massless jet. The kinematic variables can be derived as:

$$Q^2_{DA} = \frac{4E_e^2 \sin\gamma_h(1+\cos\theta_e)}{\sin\gamma_h + \sin\theta_e - \sin(\gamma_h+\theta_e)} \tag{4.10}$$

$$y_{DA} = \frac{\sin\theta_e(1-\cos\gamma_h)}{\sin\gamma_h + \sin\theta_e - \sin(\gamma_h+\theta_e)} \tag{4.11}$$

$$x_{DA} = \frac{Q^2_{DA}}{s \cdot y_{DA}} \tag{4.12}$$

The subscript *DA* denotes the double angle method, and $E_e$ is the initial electron energy. Because of its dependence on $E_e$ and $\theta_e$ this method is sensitive to radiative effects, though less than the electron method. The double angle method stands out because it is to a good approximation independent of the overall energy scale of the calorimeter measurement. This predestines it to be used in the calibrations of both the electromagnetic and hadronic calorimeter sections. This will be discussed in section 4.3.

With the double angle method the event's transverse momentum and the scattered electron's energy can be derived from:

$$P_{T,DA} = \frac{2E_e \sin\gamma_h}{\sin\gamma_h + \sin\theta_e - \sin(\gamma_h+\theta_e)} \tag{4.13}$$

$$E'_{e,DA} = \frac{2E_e}{\tan(\gamma_h/2) + \tan(\theta_e/2)} \tag{4.14}$$

### 4.2.2. Particle Identification

Once charged tracks have been reconstructed from the tracker information and linked to energy deposits in the calorimeter, finder algorithms are applied in order to identify the particle type. For this analysis only two types of particles are of interest: the scattered electron, and the hadronic final state, which consists, of course, of many particles. However, for practical reasons it is treated as an entity in the following. It is defined as all the particles found in the detector, minus the isolated leptons. Both finder algorithms are outlined in the following.

These overviews follow the PhD thesis of Andrei Nikiforov [17]. A detailed description of the electron identification algorithm can be found in [38] and on the webpage [39]. The hadron identification is presented in the H1 internal note [40].

#### Scattered Electron

At the high momentum transfers considered in this analysis, the beam electron is scattered into the liquid argon calorimeter. An electron can be identified by its compact shower shape and isolation from other activity in the calorimeter. Opposed to hadronic particles it deposits its energy entirely in the electromagnetic part of the calorimeter.

Only very high energetic electrons leave a - very small - signal in the hadronic part of the LAr. Finally, it can be distinguished from neutral photons by a charged track pointing towards the calorimeter cluster. Several estimators are used to check for these characteristics.

In order to rule out random calorimeter noise and low energetic hadrons it is required that the total energy of the cluster is at least 5 GeV and the transverse momentum 3 GeV. Furthermore, at least four calorimeter cells have to contribute to the cluster.

To ensure its containment in the electromagnetic part, it is required that at least 94% of the cluster's energy is deposited in the electromagnetic part. The compactness of electron showers results in the requirement that at least 98% of the energy of an electron candidate is found within a cone of radius 0.25 in $\eta - \phi$. The *pseudo-rapidity* is defined as $\eta = -\ln(\theta/2)$.

Finally, in order to distinguish the electron from a photon, the calorimeter cluster has to be associated with a charged track. This is given if the distance in $\eta - \phi$ between cluster and the track when extrapolated to the calorimeter is less than 0.1.

Although these requirements reach a rate of misidentification of less than 1% [41], it has to be ensured that a high energetic electron from a jet is not misidentified as the scattered electron. An electron is considered isolated against hadrons if the calorimeter energy in a cone with the radius 0.5 in $\eta - \phi$ around the electron is less than 5% of the electron energy.

### Hadronic Final State and Jets

The reconstruction of the hadronic final state is done by the Hadroo2 algorithm [40]. It is a particle flow based algorithm that combines information from tracks and calorimeter clusters. The information previously acquired on isolated leptons, especially the scattered electron, is taken into account unaltered, and those particles are not included in the hadronic final state.

After the hadronic final state is reconstructed an attempt is made to combine the identified particles to jets. This is done using a $k_t$ clustering algorithm [42] with a $P_T$ weighted recombination scheme [43].

## 4.3. Electromagnetic and Hadronic Energy Calibrations

In case of neutral current events both the electron and the hadronic final state can be measured in the detector. Since several different reconstruction methods can be applied, the kinematics of these events are over-constrained. This fact is used to calibrate the electron energy measurement. The double-angle method is to first order independent of calorimeter energies. In a sufficiently precise sample of neutral current events the directly measured electron energy is compared to the one predicted by the double angle method, and a calibration of the calorimeter response is done. Details can be

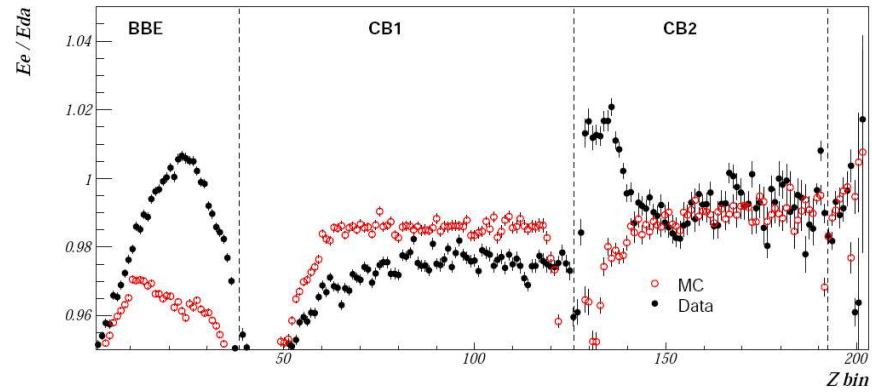


(a)

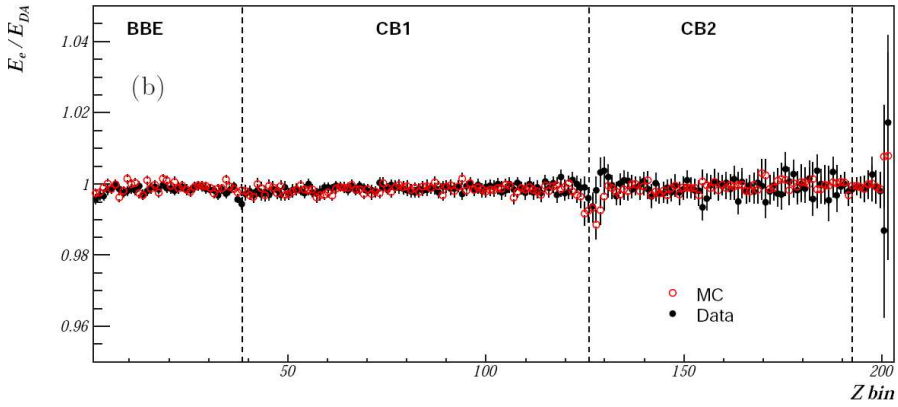


(b)

***Figure 4.1.:*** *Effect of electron energy calibration. The ratio of the directly measured electron energy and the one predicted by the double angle method is plotted versus the z-position of the electron's point of entry into the calorimeter. Full circles represent the data, and open circles a simulation. Shown are the backward barrel BBE, and the central barrels CB1 and CB2 of the liquid argon calorimeter (cf. figure 3.5) (a) before and (b) after the calibration, from [17].*

found in [17] and [44]. Figure 4.1 shows the ratio $E_e/E_{DA}$ both for data and a simulation plotted versus the $z$-position of the electron's point of entry into the calorimeter. Subfigure (a) shows the distribution before, subfigure (b) after the calibration. The calibration is very successful. Within less than one percent the ratio is close to one.

The calibration of the hadronic energy measurement is done within the Hadroo2 algorithm [40]. It relies on the same principle as the electronic energy calibration. In this case the calibration is done by comparing the transverse momentum directly measured from the hadronic final state (equation 4.6) with the one predicted by the double angle method (equation 4.13). This ratio $P_T^h/P_T^{DA}$ is sometimes called $P_T$-

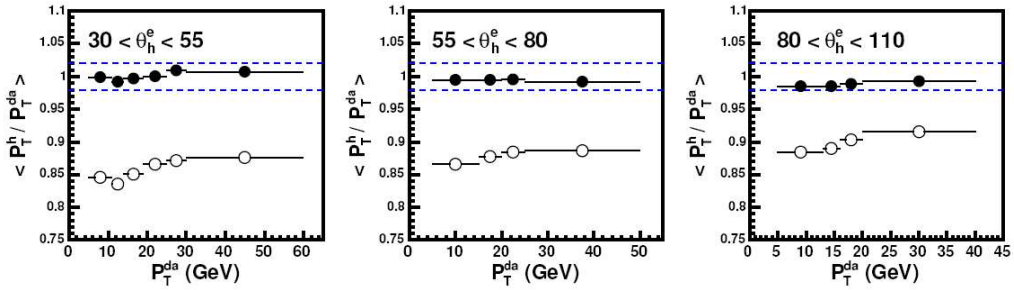


***Figure 4.2.:*** *Effect of hadronic energy calibration. The $P_T$-balance depending on $P_T^{DA}$ in different polar ranges for both uncalibrated (open circles) and calibrated data (full circles), from [40].*

balance. Figure 4.2 shows the effect of the calibration. Plotted is the $P_T$-balance as a function of $P_T^{DA}$ in three different polar ranges. The calibration is successful with deviations from unity of less than 2%.

## 4.4. Monte Carlo Generators

In order to compare the selected neutral and charged current data to the Standard Model predictions, Monte Carlo simulations of the processes contributing in the considered phase space region are used. The simulation of signal processes, that is neutral and charged current events, is done with `DJANGO` [45, 46]. The main source of background in both selections are photoproduction events. These are simulated with `PYTHIA` [47, 48]. Further processes and their respective Monte Carlo generators are lepton pair production (`GRAPE`, [49]), real $W^{\pm}$ production (`EPVEC`, [50]), and wide angle bremsstrahlung processes (`WABGEN`, [51]). Table 4.2 shows an overview of the integrated luminosities for the different generated processes. The generated Monte Carlo events are consecutively passed through a full simulation and digitization of the H1 detector, and the same set of reconstruction software is run as for data.

| Monte Carlo Generator | $\mathcal{L}$ / fb$^{-1}$ 0304 | 05 | 06 | 0607 | physical process |
|---|---|---|---|---|---|
| `NC_DJANGO` | 27778 | 27778 | 27778 | 27778 | neutral current |
| `CC_DJANGO` | 753 | 107 | 107 | 753 | charged current |
| `PYTHIA` | 11703 | 13200 | 13200 | 11703 | photoproduction |
| `GRAPE` | 480 | 480 | 480 | 480 | lepton pair production |
| `EPVEC` | 200 | 200 | 200 | 200 | real $W^{\pm}$ production |
| `WABGEN` | 933 | 933 | 933 | 933 | wide angle bremsstrahlung |

***Table 4.2.:*** *Integrated luminosities of Monte Carlo simulations used in this analysis, split up into different run periods.*

### Simulation of Leptoquark Events

For the simulation of leptoquark events which is needed for the limit calculation no dedicated Monte Carlo generator is used. The experimental signature of first generation leptoquark events is indistinguishable from neutral and charged current events, and the only difference arises from the cross sections. The necessary simulations are done by reweighting the DJANGO simulations of neutral and charged current events to the respective leptoquark cross section. This process is described in more detail in section 6.2.

# Chapter 5.

# Selection of Neutral and Charged Current Events

In this chapter the selection of neutral and charged current events from the datasets introduced in the previous chapter is described. Since many measures applied to the data, especially those concerning data quality, are the same or very similar for the neutral and charged current selection, they are described in general, and minor differences between both selections are pointed out. Very specific neutral and charged current cuts are described in separate sections at the end of this chapter. The chapter closes with control plots for both selections.

This analysis uses the `H1OO` framework, which is an extension of the `root` package developed at CERN [54, 55]. It is the general analysis tool for H1. Further information can be found in [52] or on the website [53]. On top of this, the analysis software Marana is used [56]. It provides additional tools and easier handling of measures like energy calibrations, and the application of efficiencies and systematic shifts.

## 5.1. Event Timing

In a first step a basic selection of the large HERA-2 data set is made. It is mainly focused on improving the data quality. A large fraction of the recorded data does not originate from electron proton interactions. Possible sources are:

- cosmic muons, that are produced by interactions of cosmic radiation with the particles in the earth's atmosphere.
- beam-wall or beam-gas events, that occur when a beam proton interacts with the beam-pipe wall or residual gas particles within the beam pipe.
- halo muons, that are produced in beam-wall and beam-gas events and travel parallel to the beam axis (thus surrounding the beam protons like some kind of halo)

A first measure to get rid of these non-$ep$ events is to make sure the time at which an event was recorded coincides with the time announced by HERA for a beam crossing.

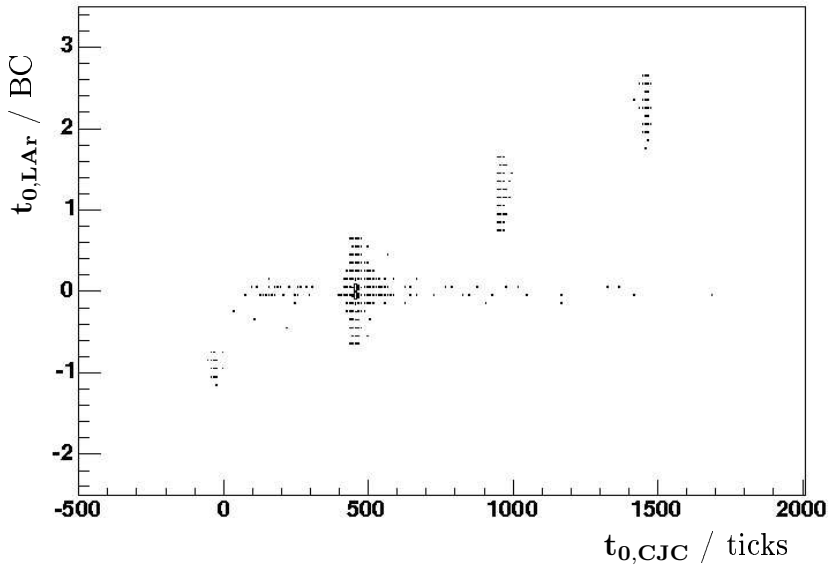


***Figure 5.1.:*** *Timing profile of the data, from [57].* 500 ticks $\hat{=}$ 1 BC $\hat{=}$ 96 ns.

In HERA the lepton and proton bunches collide in H1's interaction point every 96 ns, called a bunch crossing. The exact time is stored. It is possible to reconstruct the time of interaction from the drift time recorded by H1's central jet chambers. The CJCs achieve a time resolution of 2 ns.

In addition, timing information can be acquired from the liquid argon calorimeter. The LAr's time resolution is considerably lower: one tenth of a bunch crossing (BC), or 9.6 ns.

On the basis of these timing resolutions the following time windows are defined:

$$\Delta t_{\mathrm{CJC}} = 0.1\,\mathrm{BC} = 9.6\,\mathrm{ns} \tag{5.1}$$

$$\Delta t_{\mathrm{LAr}} = 0.7\,\mathrm{BC} = 67.2\,\mathrm{ns} \tag{5.2}$$

An event is considered to have correct timing if the event times reconstructed both from the CJCs and the LAr coincide with the nominal HERA bunch crossing time, within the respective time windows $\pm\Delta t$. A shift of up to two bunch crossings to either side is accepted, as long as both detector components measure the same shift. In case no tracks could be reconstructed in the central tracker, the event is accepted if the LAr timing information is correct. However, in this case it has to concur with the nominal bunch crossing time, no shifts are allowed.

A timing profile of the selected data is displayed in 5.1. It was taken from [57]. The figure shows a two dimensional plot of the selected events, binned in the timing information from the CJCs and the LAr: $t_{0,CJC}$ and $t_{0,LAr}$. An offset in $t_{0,CJC}$ of about 500 ticks, that is 1 BC, can be observed. The majority of events has been found at the actual bunch crossing time, but additional events have passed the cut, that are shifted $-1$, $+1$, and $+2$ bunch crossings in both variables. The width of the distributions in $t_{0,CJC}$ and $t_{0,LAr}$ direction correspond to the time windows defined in equations 5.1 and 5.1. Furthermore, one can recognize the events that have been triggered on timing information from the calorimeter only. They form an oblong horizontal distribution.

## 5.2. Topological Signature

Despite removing events with wrong timing, some non-*ep* events still remain in the data set, because they happened close to the nominal bunch crossing time. These events may overlay real *ep* events, thus biasing the reconstruction of event kinematics. In order to filter out those events a set of algorithms has been devised, that scans for topological signatures.

The topological finders are divided in three bitcoded sets: one set is called *safe* finders (Ibg) because they are considered to have a negligible rate of misidentifying real *ep* events as background. The two further sets, that are specifically designed for charged current analyzes are called Ibgam and Ibgfm.

One halo and one cosmic finder algorithm from the Ibg set and one beam-gas finder from the Ibgfm set are discussed exemplary. A detailed description can be found in the H1 internal notes [58] and [59].

The HALAR algorithm entirely relies on information from the liquid argon calorimeter to identify halo muons by checking for a horizontal energy pattern parallel to the beam axis. This corresponds to the typical signature of a halo event: a muon entering the detector in time with the proton while traversing parallel and close to the beam pipe. The LAr barrel is divided into $36 \times 26(\phi, z)$ sectors. For each value of $\phi$ triplets of adjacent sectors are checked for energy deposits exceeding noise level. If 19 or more triplets fulfill this condition the event is tagged as halo muon. Alternatively if there are at least 12 neighboring sectors exceeding the noise threshold for one $\phi$ and not more than 7 sectors for any other value of $\phi$, the event is identified as a halo muon as well.

The COSMULAR algorithm is designed to identify cosmic muons by matching all calorimeter energy to the direction of a muon track. The algorithm checks for a track with a polar angle between 10° and 170°, which has been reconstructed by at least 8 hits in the muon chambers. If more than 90% of the entire energy deposited in the calorimeter is contained in a cylinder of 90 cm radius around the muon track, this event is tagged as cosmic.

The BEAMGAS algorithm from the Ibgfm package checks for an abundance of tracks in the backward region (i.e. entering the detector with the proton) not coming from the vertex. The event is flagged as beam-gas if there are at least 10 tracks identified

by the central tracker, that have a minimal track length of 25 cm and a start point of 35 cm behind the nominal vertex, that cannot be fitted to the vertex.

As opposed to the set of *safe* finders used for the neutral current selection, some of the Ibgfm and Ibgam algorithm additionally used for the charged current events have a low quality. The quality of an algorithm is defined as the fraction of real charged current events that correctly pass the finder. They have to be excluded from the analysis. In addition, the quality of some of the algorithms is not correctly reproduced in the Monte Carlo simulations.

The Marana software package provides a recommended selection of algorithms for both neutral and charge current analyzes, along with their efficiencies in Monte Carlo simulations. Those finders are used in this analysis, and the efficiencies have been used to reweight the Monte Carlo simulations (see section 5.10.3).

## 5.3. Primary Vertex

The longitudinal position of the interaction point, the $z$-coordinate of the primary vertex $z_{\text{vtx}}$, should be centered within the detector, in order to guarantee an optimal reconstruction of event properties, and to veto non-$ep$ background events. The exact position of the interaction point along the beam axis can only be adjusted within some centimeters due to the length of the proton bunches in beam direction: $\sigma_z^p \approx 13\,\text{cm}$. The electron bunches are much shorter: $\sigma_z^e \approx 2\,\text{cm}$. The distribution of the primary vertex of $ep$ events thus follows a Gaussian distribution around the nominal interaction point. In order to make sure only events from $ep$ interactions with a central vertex enter the analysis, $z_{\text{vtx}}$ has been limited to be within $\pm 35$ cm of the center of the detector. In the Monte Carlo simulations the event vertex is generated with a broader shape, in order to be applicable to different run periods. Therefore, the simulated vertex distribution has to be reweighted to the respective dataset. This is described in section 5.10.4.

## 5.4. Triggers

As described in section 3.6 a subtrigger is a logical combination of several trigger elements, making it possible to identify certain event topologies already at the hardware level. The trigger elements represent electronic components that test the raw detector output for various features or do comparisons with predefined threshold values.

Three subtriggers are used in this analysis for the selection of neutral and charged current events: S66, S67, and S77. While for the charged current selection all three subtriggers are used, the neutral current analysis leaves out S66. The subtriggers are connected via a logical OR, meaning an event is accepted when at least one of these subtrigger conditions is fulfilled. The definition of the three subtriggers is shown in table 5.1. However, only the most important trigger elements are given. Further trigger elements use timing information from the liquid argon calorimeter and the central track

| subtrigger | definition |
|---|---|
| S66 | `LAr_Etmiss>2 && LAr_IF>1` |
| S67 | `LAr_electron_1` |
| S77 | `LAr_Etmiss>1 && CIP_sig>0` |

***Table 5.1.:*** *Definition of subtriggers used in this analysis.*

chamber, as well as veto conditions from the time-of-flight and CIP systems to reject non-ep events [60]. The integer values in the subtrigger definitions represent different threshold values, the subtriggers are checked against. In the following an explanation of all subtriggers is given.

### S66

This subtrigger is designed specifically for the selection of charged current events, and is thus used only in that selection. The subtrigger scans for a large imbalance in transverse energy deposited in the liquid argon calorimeter (`LAr_Etmiss>2`). The threshold value 2 corresponds to an energy of 6 GeV. Missing energy is a topology typical for charged current events since a neutrino is one of only two particles in the final state, and thus carries off a considerable amount of energy undetected. In addition to this an energy deposition in the calorimeter's inner forward part is required (`LAr_IF>1`).

### S67

Subtrigger S67 is primarily designed for the detection of electron candidates in the liquid argon calorimeter (`LAr_electron_1`). It is used in the neutral current analysis to trigger on the scattered electron in the final state. This is done by checking for a large and compact energy deposition in the electromagnetic part of the calorimeter with a veto condition on energy deposited in the hadronic calorimeter. However, the veto threshold is very high, so that S67 almost exclusively triggers on energy depositions in the electromagnetic section. This makes it also suitable for the detection of jets, which usually also have a large electromagnetic component. For this purpose S67 is also included in the trigger combination of the charged current selection.

### S77

Subtrigger S77 is similar to S66 in that it also checks for missing transverse energy in the liquid argon calorimeter (`LAr_Etmiss>1`). The threshold value 1 corresponds to an energy of 4.5 GeV. For this reason it is included in the charged current trigger mix. However, the energy threshold of the trigger element `LAr_Etmiss` is lower in this case, which makes S77 also suitable for neutral current selections. Neutral current events may show an apparent energy imbalance for several reasons: limited geometrical acceptance and energy resolution of the detector, or the saturation of the readout electronics by a

very high energetic electron [17]. This will be discussed further in section 5.9.2. Since the energy threshold of this trigger element is rather low, it may also be triggered by non-ep events, like noisy calorimeter cells. To exclude this, the trigger element is combined with an additional (minimal) requirement on the significance of tracks detected in the central inner proportional chamber (`CIP_sig>0`) [60]. The number of tracks in the central chamber has to exceed the sum of tracks in the forward and backward tracking detectors.

## 5.5. Fiducial Volume

The barrel of the liquid argon calorimeter is not a single monolithic structure but built up of several wheels and octants (cf. section 3.3.1). Between these the cables for the photodetectors' high voltage supply and the read-out electronics are run rendering these spaces insensitive material. Particles entering the calorimeter through these gaps may escape detection, or if they enter in close proximity, their energy may be misreconstructed. In case of neutral currents the energy of the scattered electron may be incorrect. However, the electron method used for kinematic reconstruction, heavily depends on this information. In charge current events, the energy of the hadronic final state may be heavily biased. In case of neutral (charged) currents, those events are removed from the final selection which have the electron (hadronic final state) enter the calorimeter within 2 cm of a crack.

## 5.6. Limitation of Kinematic Range

As a last step in this preselection the phase space of this analysis is limited. First of all, the inelasticity $y$ has to be limited due to detector constraints. For charged current events with no electron in its final state this quantity has to be reconstructed by the hadron method. Because of equation 4.7 $Q_h^2$ is proportional to $1/(1-y_h)$, and thus the $Q^2$ resolution of the hadron method is limited for high values of $y$. Furthermore, events with low values of $y_h$ have a hadronic final state scattered into the very forward region of the detector. For those events vertex reconstruction efficiencies are very low. This is why a double cut on the inelasticity is introduced:

$$0.1 < y_h < 0.9 \tag{5.3}$$

For neutral current events the inelasticity can be derived from energy and polar angle of the scattered electron. This method does not have the same shortcomings as the hadron method concerning the $Q^2$ resolution. However, the limitations for low values of the inelasticity still apply. The same cut as in the charged current case is applied to $y_e$:

$$0.1 < y_e < 0.9 \tag{5.4}$$

Since this analysis is dedicated to the search for heavy exchange bosons, a high momentum transfer is required:

$$Q_e^2 > 1000\,\mathrm{GeV}^2 \tag{5.5}$$

This drastically limits the number of events, but due to the large total cross section of neutral current events still provides ample statistics for control plots and the limit extraction process.

In case of charged current events, whose total cross section in this kinematic domain is about one order of magnitude below that of neutral currents, this cut has to be lowered:

$$Q_h^2 > 500\,\mathrm{GeV}^2 \tag{5.6}$$

## 5.7. Jet Requirements

Since this analysis is searching for heavy particles, one can expect the quark (and thus the resulting jet) to be high energetic. It is required that at least one jet with a transverse momentum of $P_T > 12\,\mathrm{GeV}$ is identified in the datasets for both the neutral and charged current selection.

Up to this point the measures and cuts applied to the data have been similar for both neutral and charged current events. The next to section describe the additional measures that have been applied to the two selections separately.

## 5.8. Neutral Current Specific Cuts

The dataset selected so far already contains many neutral current events. However, the purity can be further increased by applying some additional cuts. The most important requirement is the reliable identification of an isolated high energetic scattered electron. It is required that the scattered electron is identified and has an energy of at least

$$E_e > 12\,\mathrm{GeV} \tag{5.7}$$

The electron has to be isolated. It has to be reconstructed from information from the liquid argon calorimeter not just from the SpaCal or track based algorithms. Figure 5.2 shows the effect of these measures. The figure shows the inelasticity $y_e$ both before and after the application of the requirements. The amount of charged current events in the sample is reduced.

The longitudinal momentum balance is defined as: $E - P_z = \sum_i E_i - P_{z,i}$, with the sum including all particles in the detector. In order to further increase the purity of the sample, the following cut is applied:

$$35\,\mathrm{GeV} < E - P_z < 70\,\mathrm{GeV} \tag{5.8}$$

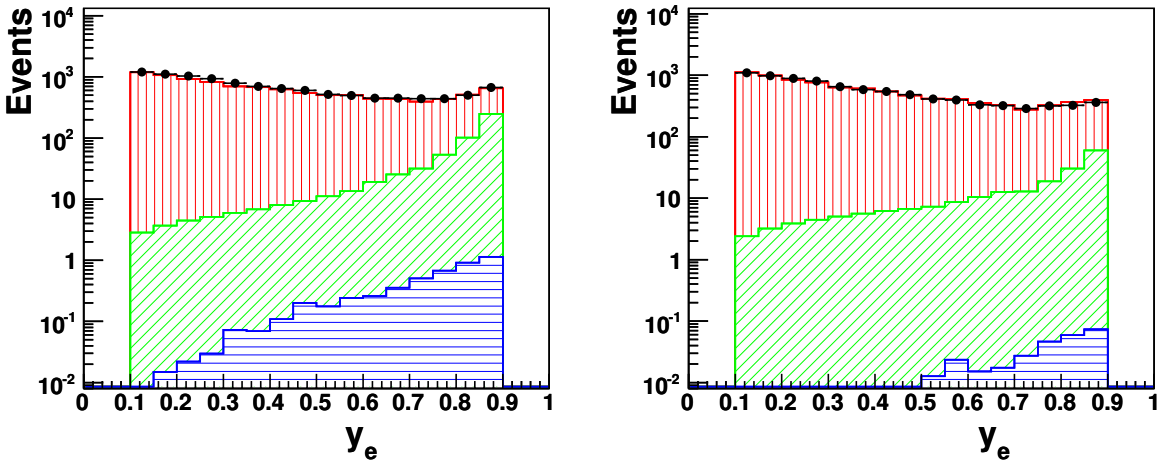


***Figure 5.2.:*** *Effect of electron requirements on the neutral current selection: The inelasticity $y_e$ is shown (a) before and (b) after requiring a high energy scattered electron. The black points show the data, whereas the vertically hatched red area denotes the neutral current, the horizontally hatched blue area the charged current, and the diagonally hatched green area the background Monte Carlo simulations.*

The distribution of the longitudinal momentum balance before this cut is shown in figure 5.3. In the $E-P_z$ ranges, that are removed, the background simulation makes up $\approx 10\%$ of the total Monte Carlo simulation. The neutral current events are clustered in $35\,\text{GeV} < E - P_z < 70\,\text{GeV}$, where they exceed the remaining events by two orders of magnitude.

## 5.9. Charged Current Specific Cuts

After the neutral current specific cuts explained in the precious section, this section starts with the dataset with the cuts described up to section 5.7.

Up to this point no dedicated charged current cut has been applied. The data set selected so far still contains mostly neutral current events which have a much larger cross section in this kinematic region. The main non-DIS background source are photoproduction events. Firstly, the longitudinal momentum balance $E - P_z$ of the event must not exceed 50 GeV. A distribution of this variable before the cut is shown in figure 5.4. The charged current events have a longitudinal momentum balance well below the cut threshold. By this cut a large fraction of neutral current and other background events are removed from the charged current sample. In addition, a data overshoot for large values of $E - P_z$ can be observed. These non-$ep$ background events are removed by this cut as well.

Then the most important cut in the charged current selection is applied.

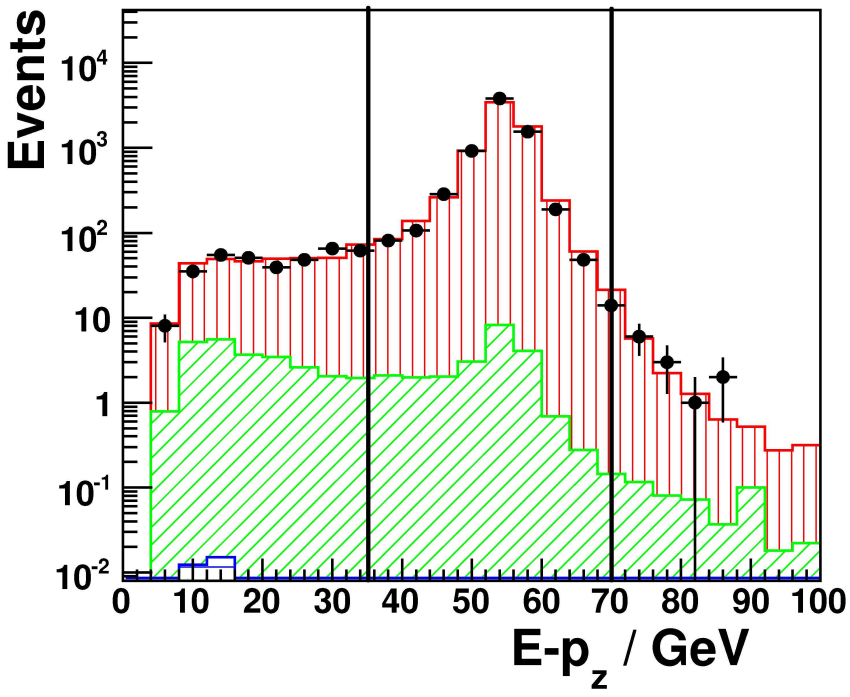


***Figure 5.3.:*** *The longitudinal momentum balance before application of the cut* $35\,\text{GeV} < E - P_z < 70\,\text{GeV}$ *on the neutral current selection. The black points show the data, whereas the vertically hatched red area denotes the neutral current, the horizontally hatched blue area the charged current, and the diagonally hatched green area the background Monte Carlo simulations. The cut values are indicated by vertical black lines.*

### 5.9.1. Missing Transverse Momentum

The distinct feature of charged current events is the outgoing neutrino. Momentum conservation causes this neutrino to carry the same amount of transverse momentum as the quark. The neutrino escapes the detector without depositing energy in the calorimeters or leaving a signature in the tracking chambers. The transverse momentum of such an event will be imbalanced as only the hadronic final state is detected and enters the kinematic reconstruction. A cut is applied at

$$P_T^{\text{miss}} > 12\,\text{GeV} \tag{5.9}$$

Figure 5.5 shows the distribution of $P_T^{\text{miss}}$ before the cut is applied. It can be seen that most background events have a $P_T^{\text{miss}}$ well below 12 GeV and are effectively removed from the data set. Especially the neutral current events in the sample mostly have $P_T^{\text{miss}} < 10\,\text{GeV}$. However, some background events, consisting predominantly of photoproduction events, have a high missing transverse momentum and pass the cut. The cut may have been tightened to $P_T^{\text{miss}} > 20\,\text{GeV}$, but in order not to discard too

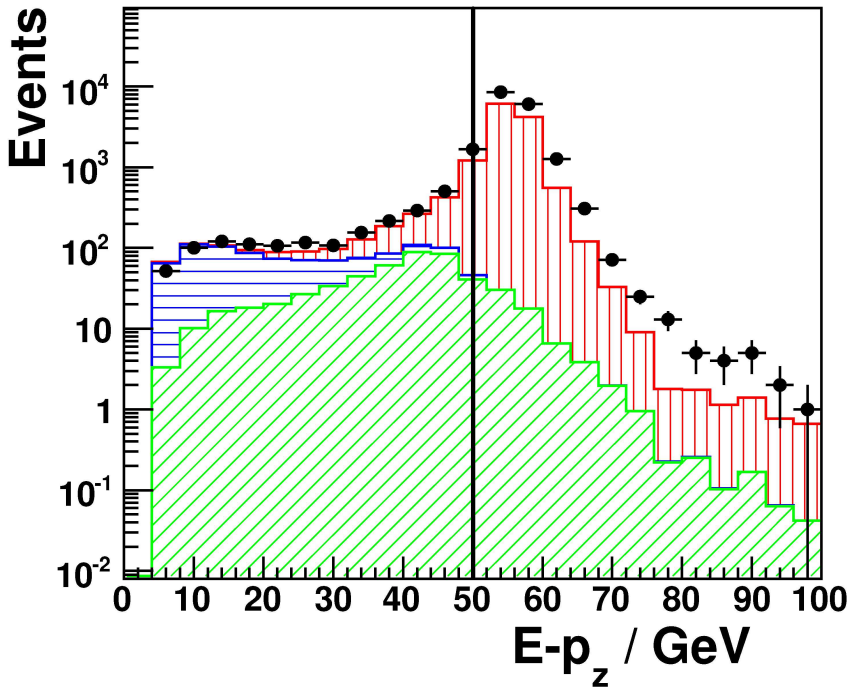


***Figure 5.4.:*** *The longitudinal momentum balance before application of the cut $E - P_z < 50\,\mathrm{GeV}$ on the charged current selection. The black points show the data, whereas the horizontally hatched blue area denotes the charged current, the vertically hatched red area the neutral current, and the diagonally hatched green area the background Monte Carlo simulations. The cut value is indicated by a vertical black line.*

many charged current events this has been avoided. The remaining background events can be removed by a second cut.

### 5.9.2. Acoplanarity

The presence of neutral current and photoproduction events with a high missing transverse momentum has no physical but merely technical reasons. Limited geometrical acceptance and energy resolution or saturated readout electronics in case of very high energetic electrons can bias the reconstruction leading to events incorrectly imbalanced in $P_T$.

However, these events still differ significantly from charged current events in their topological signature. Figure 5.6 shows typical charged current, neutral current, and photoproduction events in a radial view of the detector. The charge current events display an clear imbalance of calorimeter entries, while the neutral current events are still more or less balanced, despite a possibly misreconstructed transverse momentum. These topological differences can be quantified by the so called acoplanarity $\mathcal{V}$ or V-

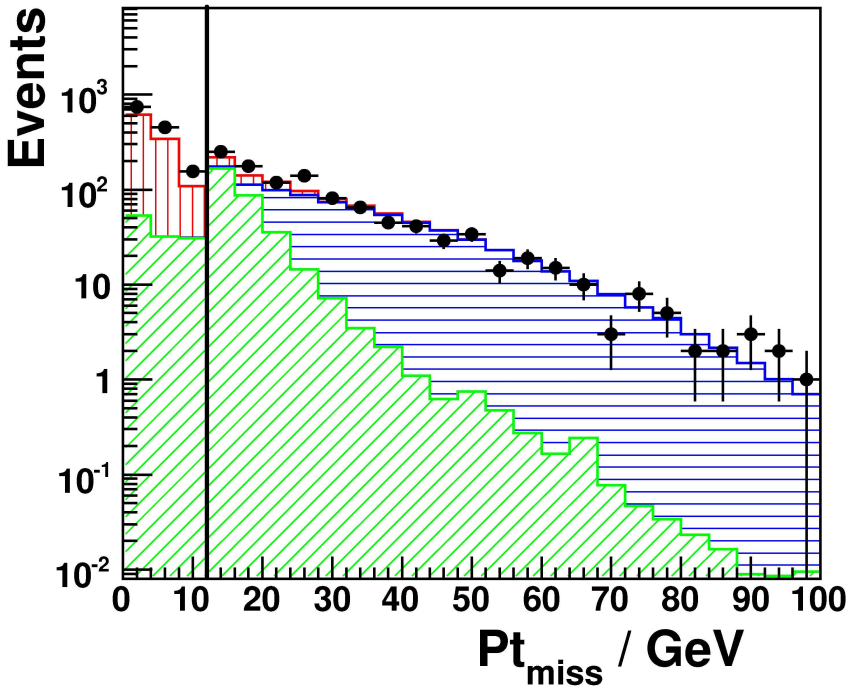


***Figure 5.5.:*** *The missing transverse momentum before application of the cut $P_T^{miss} > 12\,\mathrm{GeV}$ on the charged current selection. The black points show the data, whereas the horizontally hatched blue area denotes the charged current, the vertically hatched red area the neutral current, and the diagonally hatched green area the background Monte Carlo simulations. The cut value is indicated by a vertical black line.*

ratio of the event. It is defined as follows:

$$\mathcal{V} = \frac{V_{ap}}{V_p} \tag{5.10}$$

with

$$V_p = \sum_i \vec{P}_{T,i} \cdot \vec{n}_{P,h} \qquad \text{for } \vec{P}_{T,i} \cdot \vec{n}_{P,h} > 0 \tag{5.11}$$

and

$$V_{ap} = -\sum_i \vec{P}_{T,i} \cdot \vec{n}_{P,h} \qquad \text{for } \vec{P}_{T,i} \cdot \vec{n}_{P,h} < 0 \tag{5.12}$$

The summation runs over all particles in the detector, and $\vec{n}_{P,h}$ represents the unit vector in direction of the hadronic final state's transverse momentum. In this definition $V_p$ ($V_{ap}$) is the sum over all transverse momenta that are in the same (opposite) detector hemisphere as the hadronic final state. Thus, for a typical charged current event one expects the acoplanarity to be close to zero, whereas for the background (neutral current and photoproduction) with balanced transverse momenta events, it will be close to one.

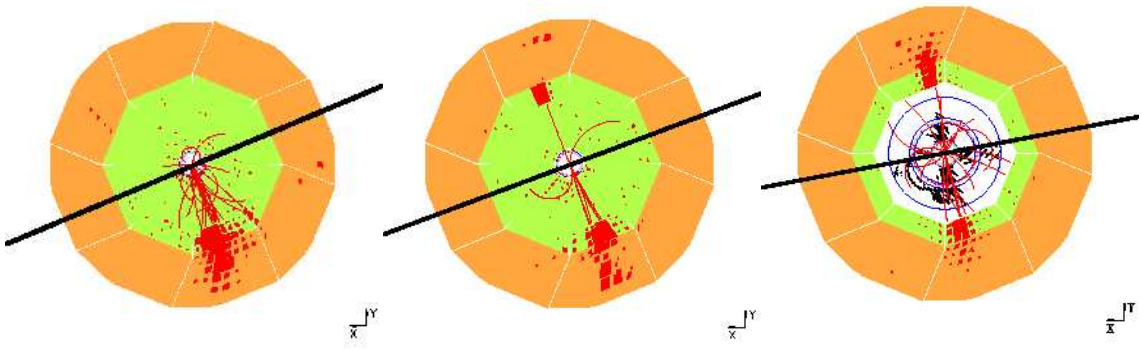

(a) (b) (c)

***Figure 5.6.:*** *Schematic of the definition of acoplanarity: Shown are radial views of the detector for typical (a) charged current, (b) neutral current, and (c) photoproduction events. The black line is perpendicular to the direction of the hadronic final state, and divides the detector in two hemispheres (see equations 5.11 and 5.12).*

The background events with misreconstructed transverse momenta discussed above have $\mathcal{V} < 1$, but still considerably larger than for charged current events.

A two-dimensional cut in $\mathcal{V}$ is applied.

$$\begin{aligned} \mathcal{V} &< 0.35 \qquad \text{for } P_T^{\text{miss}} > 25\,\text{GeV} \\ \mathcal{V} &< 0.15 \qquad \text{for } P_T^{\text{miss}} < 25\,\text{GeV} \end{aligned} \tag{5.13}$$

For events with high missing transverse momentum $P_T^{\text{miss}} > 25\,\text{GeV}$ the acoplanarity must not exceed 0.35. For events with $P_T^{\text{miss}} < 25\,\text{GeV}$, which is the kinematic region where most of the remaining background events are, the cut threshold on $\mathcal{V}$ is enforced to 0.15.

In figure 5.7 this cut is illustrated in the $P_T^{\text{miss}} - \mathcal{V}$-plane. A clean separation of charged current and background events is visible.

## 5.10. Monte Carlo Simulation Reweighting

In order to compare the selected data events with the Standard Model predictions, represented by Monte Carlo simulations, the latter have to be reweighted.

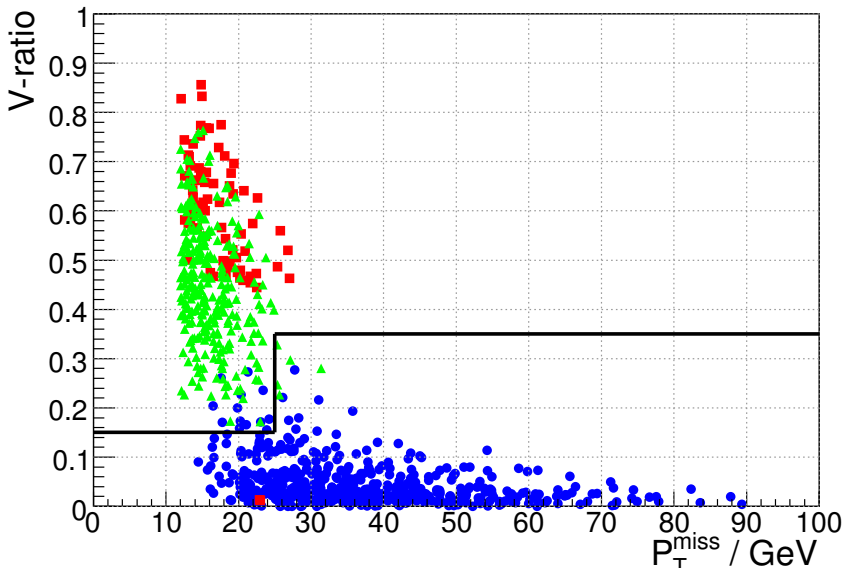


***Figure 5.7.:*** *The distribution of the V-ratio (acoplanarity $\mathcal{V}$) plotted against the missing transverse momentum $P_T^{miss}$ before the cut. Blue circles represent the charged current, red squares the neutral current, and green triangles the background simulations. The two-dimensional cut (cf. equation 5.13) is represented by the black line. Only events* below *the line are kept in the selection.*

### 5.10.1. Luminosity

The Monte Carlo simulations used in this analysis are generated with a much higher integrated luminosity than the data luminosity. This is done in order to minimize statistical uncertainties on the predicted distributions. For each data set of this analysis the Monte Carlo simulations are reweighted to the respective data luminosity. The according luminosities can be found in table 4.1 (data) and 4.2 (simulations).

### 5.10.2. Polarization

All Monte Carlo simulations are generated for the case of unpolarized beam electrons. However, the search for leptoquarks presented in this analysis relies heavily on the use of polarized beams, which is why the data has been split up in polarized subsets. The cross sections for both charged and neutral events depend on the lepton polarization (see section 2.2.3). This has been considered and the simulations are reweighted accordingly.

### 5.10.3. Efficiencies

For the charged current selection the efficiencies of both triggers and background finders are not reproduced correctly in the simulations. In both cases reweighting factors

provided by the `Marana` package have been applied to the charged current DJANGO Monte Carlo. These values are not applied globally but in $x_h$ and $Q_h^2$ bins to individual events. Figure 5.8(a) shows the factors that were applied for the background finders efficiencies. Different reweighting factors for the trigger efficiencies have been applied depending on the runyear. As an example the values for the 2006/07 $e^+p$ runperiod (0607L and 0607R in table 4.1 on page 38) are shown in figure 5.8(b).

The subtrigger S67 that is the only one used for the neutral current selection is considered to be well reproduced in the simulation of these events. For the rejection of non-ep background events only the set of *safe* finders has been used. These algorithms are also very well reproduced, so no efficiency weight is applied to the neutral current DJANGO simulation.

### 5.10.4. Vertex Reweighting

For the simulations, the Gaussian distribution of the interaction vertex is generated broader than it actually is. The control by HERA's operating crew over the the exact position of the interaction point is limited, causing its mean position to change slightly between different run periods. To ensure that one Monte Carlo simulation can be used to described data sets from different years, the vertex is generated broader than in reality. Thus, even events in the far tails of the vertex distribution are simulated with sufficient statistics.

In consequence the simulations have to be reweighted to the different data sets used in this analysis. This procedure is only performed for the dominating neutral and charged current processes. The result is shown in figure 5.9 exemplary for the neutral current selection.

## 5.11. Systematic Uncertainties

The correlated systematic uncertainties, also called 'systematic errors', are determined by applying systematic shifts to important properties in the Monte Carlo simulations. This procedure is performed eventwise. For the neutral current selection these shifts are applied to the electronic energy and polar angle. The electron energy is shifted between 0.7% and 3%, depending on $z$-coordinate of the electromagnetic cluster in the calorimeter. The polar angle electron is varied by 10 mrad.

For both the neutral and charged current selection systematic shifts are applied to the hadronic energy and polar angle. The energy is scaled up and down by 2%. The polar angle of the hadronic final state is shifted by 10 mrad in case it was measured by the central tracking detectors, and by 5 mrad in case it was reconstructed from forward tracking detector information.

In addition to these correlated, eventwise systematic shifts, some global systematic uncertainties are applied to the selection. The luminosity measurement is attributed an error of 1.3% for the 2003/04 data, 2% for the 2005 data, and 4% for all data from

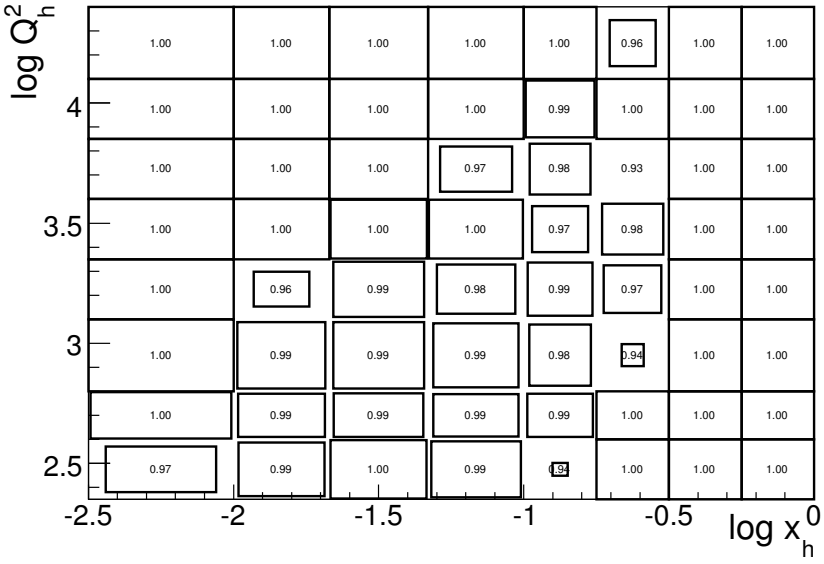


**(a)**

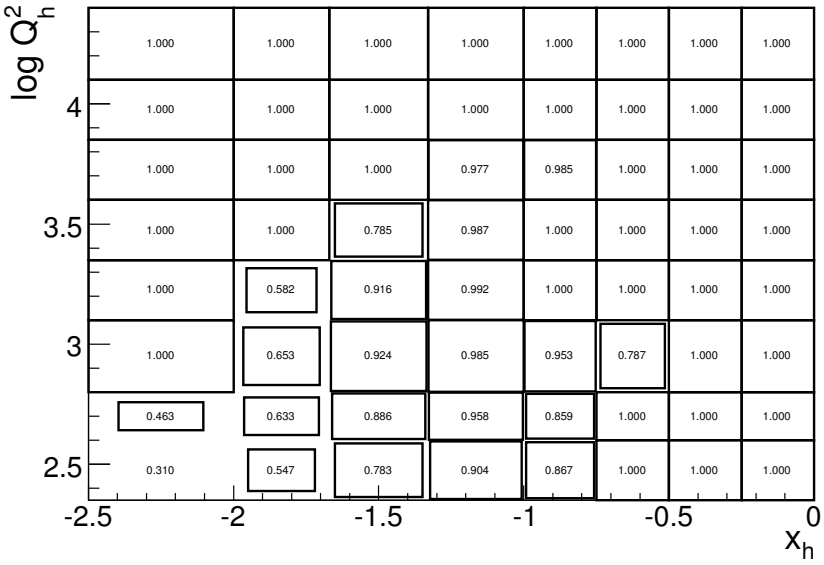


**(b)**

***Figure 5.8.:*** *Monte Carlo reweighting factors for (a) background finders and (b) trigger efficiency. The latter is shown for the 2006/07 $e^+p$ runperiod (0607L and 0607R in table 4.1).*

2006 on. The polarization measurement is attributed a global systematic error of 3.4%. For radiative corrections an uncertainty of 1% is used. In case of trigger efficiencies the global uncertainty is different for the two selections: 1% for the neutral and 1.8% for

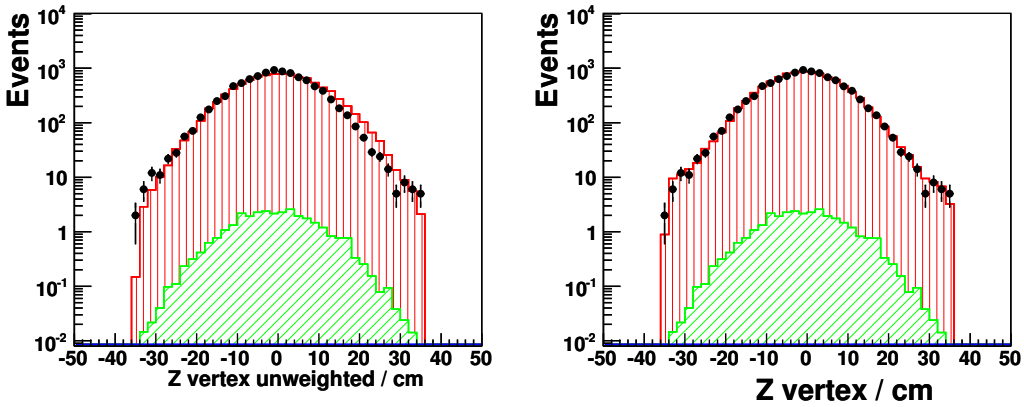


(a) (b)

***Figure 5.9.:*** *Example of vertex reweighting. Shown are the $z_{vtx}$ distributions for the neutral current selection in the dataset 0607L (a) before and (b) after the reweighting. The data are signified by black points. The neutral current simulation is shown as vertically hatched red area. The diagonally hatched green area is the background simulation, that is not reweighted.*

the charged current simulation.

The global systematic on the vertex finding efficiency is only applied to the CC selection (2.4%). In neutral current the scattered electron is present resulting in an efficient vertex reconstruction. Also, the neutral current selection only uses *safe* background finding algorithms (see section 5.2), that are very well reproduced in the simulation, so no systematic uncertainty is assumed. For charged current selections an uncertainty of 2% is used.

Finally, systematic uncertainties on the theoretical models represented by the Monte Carlo simulations are taken into account. Most important one is the uncertainty on the signal `DJANGO` simulation, which is assumed to be 10%. Large errors are assumed for the background simulations, especially for `PYTHIA` photoproduction simulation, resulting in a combined systematic uncertainty of about 60% This, however, this hardly influences the event numbers since the selected NC and CC samples contain only little background events (see section 5.12).

All systematic uncertainties described above are summarized in table 5.2.

| **systematic shifts** | |
|---|---|
| hadronic energy scale | 2% |
| hadronic polar angle | 10 mrad central, 5 mrad forward |
| electron energy scale | $0.7 - 3\%$ dependent on $z_{\text{cluster}}$ |
| electron polar angle | 10 mrad |
| **global systematics** | |
| luminosity | $1.3\% - 4\%$ dependent on run year |
| polarization | 3.4% |
| radiative corrections | 1% |
| trigger efficiencies | NC: 1%, CC: 1.8% |
| vertex finding | CC: 2.4% |
| background finding | CC: 2% |
| **theory uncertainties** | |
| DJANGO | 10% |
| PYTHIA | 50% |
| GRAPE | 30% |
| WABGEN | 30% |
| EPVEC | 15% |

***Table 5.2.:*** *Systematic uncertainties for neutral and charged current selection.*

## 5.12. Final Event Selections

Table 5.3 on the next page shows the event numbers for the neutral and charged current selections. The different datasets used (cf. table 4.1 on page 38) are summarized to the $e^+p$ and $e^-p$ runperiods of HERA-2. The number of selected data events is compared with the Standard Model predictions from simulations (total MC). A breakdown of the total Monte Carlo numbers is given: The share of neutral (NC) and charged current (CC) processes is displayed, as well a sum of all background processes (SM bgr). The stated errors are the combined statistical and systematic uncertainties. The selection purity is defined as the number of simulated signal events (NC/CC) over the total Monte Carlo events.

For both selections and both runperiods the data are very well reproduced by the Monte Carlo simulations. A slight undershoot can be observed in the neutral current electron data. It is, however, within the uncertainties of the simulation.

Figure 5.10 shows the event yields (events per $10\,\mathrm{pb}^{-1}$ of integrated luminosity) for both the neutral and charged current selections. The entire HERA-2 dataset is displayed. The beam lepton type used is indicated in the plots. For the neutral current selection the event yield is constant over the entire runrange. Smaller differences between the electron and positron data can be observed. As has already been discussed in section 2.2.3, this is due to the weak $Z$ boson exchange that contributes significantly to the neutral current cross section at the large values of $Q^2$ considered in this analysis (cf. figure 2.3).

The total charged current cross section has a strong polarization dependence $\sigma_{\mathrm{CC}} \propto 1 \mp \mathcal{P}_e$ for $e^{\pm}p$ interactions (cf. section 2.2.2). The charge current event yield has been corrected for this. The distribution is constant for each beam lepton type. There are, however, significant differences in the event yield between electron and positron data taking periods. In case of $e^-p$ reactions the exchanged $W$ boson couples to quarks with positive charge (up-type quarks), whereas in $e^+p$ interaction the gauge boson couples to down-type quarks. The quark densities for up-type quarks in the proton are larger in the kinematic range of the analysis resulting in a higher charged current cross section for $e^-p$ interactions.

### 5.12.1. Neutral Current Control Plots

Control plots for the neutral current selection are shown in figures 5.11 and 5.12 on pages 67 and 68. Six quantities are shown both for the $e^-p$ and the $e^+p$ datasets: inelasticity $y_e$, momentum transfer $Q^2_e$, longitudinal momentum balance $E - P_z$, transverse electron momentum $P^T_e$, transverse momentum balance $P^T_e/P^T_h$, and polar electron angle $\theta_e$.

In all plots a very good agreement between data and simulation can be observed. No deviation from the predicted shape can be observed in the distribution of the inelasticity $y_e$ (cf. figure 5.11(a,b)). This variable is sensitive to the presence of leptoquarks in the data, as shall be further discussed in chapter 6.

| Dataset | Data | total MC | NC | CC | SM bgr | purity |
|---|---|---|---|---|---|---|
| neutral current selection | | | | | | |
| $e^-p$ | 20901 | $22048^{+2448.4}_{-2440.0}$ | $21989^{+2447.1}_{-2438.6}$ | $0.1^{+0.01}_{-0.02}$ | $59^{+35.6}_{-35.5}$ | 99.7% |
| $e^+p$ | 22852 | $23036^{+2551.4}_{-2553.3}$ | $22964^{+2549.6}_{-2551.7}$ | $0.1^{+0.01}_{-0.01}$ | $72^{+43.2}_{-43.2}$ | 99.7% |
| charged current selection | | | | | | |
| $e^-p$ | 4829 | $4975^{+543.0}_{-544.6}$ | $26^{+3.4}_{-3.6}$ | $4890^{+539.9}_{-541.2}$ | $59^{+35.6}_{-35.7}$ | 98.3% |
| $e^+p$ | 2735 | $2694^{+294.3}_{-296.1}$ | $28^{+6.2}_{-5.9}$ | $2598^{+288.7}_{-290.5}$ | $67^{+40.9}_{-40.9}$ | 96.4% |

***Table 5.3.:*** *Event numbers for neutral and charged current selection. The HERA-2 is divided into $e^-p$ and $e^+p$ runperiods. The data are compared with the Standard Model simulations. The total Monte Carlo is the sum of neutral (NC) and charged current (CC) simulations and background processes (SM bgr). The errors shown are the combined statistical and systematic uncertainties. The selection purity is defined as $\frac{NC}{total\ MC}$ and $\frac{CC}{total\ MC}$, respectively.*

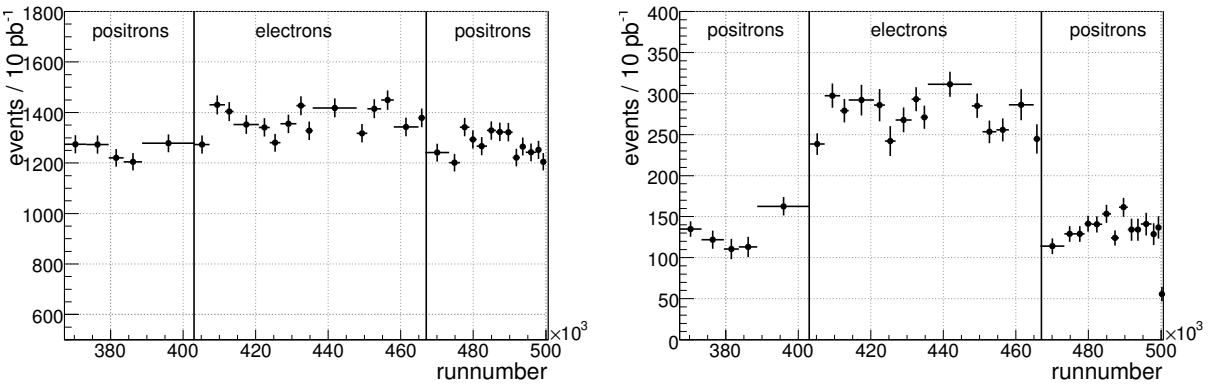


**(a)** NC **(b)** CC

***Figure 5.10.:*** *Event yields for neutral (a) and charged (b) current selections. The runrange covers the entire HERA-2 runphase. The CC selection is corrected for polarization effects.*

## 5.12.2. Charged Current Control Plots

Control plots for the charged current selection are shown in figures 5.13 and 5.14 on pages 69 and 70. Similar six quantities as for the NC selection are shown both for the $e^-p$ and the $e^+p$ datasets: inelasticity $y_h$, momentum transfer $Q_h^2$, Bjorken scaling variable $x_h$, longitudinal momentum balance $E - P_z$, missing transverse momentum $P^T_{\text{miss}}$, and polar hadronic angle $\theta_h$.

The distribution show a good agreement between data and simulation. However, the hadronic final state is not perfectly described by the simulations. In figure 5.14(c,d) small deviations can be observed in the distributions of the polar angle $\theta_h$. They are covered by the uncertainties for the most part. Another deviation can be observed

in low $y_h$ values (figure 5.13(a,b)). Nevertheless, they do not seem to hint at any significant deviation from the Standard Model predictions. This shall be discussed in more detail in chapter 6 on the search for leptoquarks.

However, in the charged current selection of the subsample 06R (2006 $e^-p$), problems were detected. This is shown in figure 5.15. Subfigures (a) and (b) depict the inelasticity $y_h$ and the hadronic polar angle $\theta_h$ for the charged current selection of this period. This phenomenon is connected with problems with the reconstruction of the hadronic final state during this period, and known within H1. So far, no solution has been found. This dataset is excluded from further analysis in this thesis, especially the limit calculation in the following chapter. Figure 5.15(c) shows that this problem is caused by misreconstruction of the hadronic final state: In the distribution of $y_e$, which is reconstructed from the scattered electron's properties, in the neutral current selection of the same runperiod no problems are observed. In figure 5.15(d) $\theta_h$ is shown for charged current selection in the 06L runperiod. Again, the data are well reproduced by the simulation. This signifies that the observed problems are limited to the said runperiod.

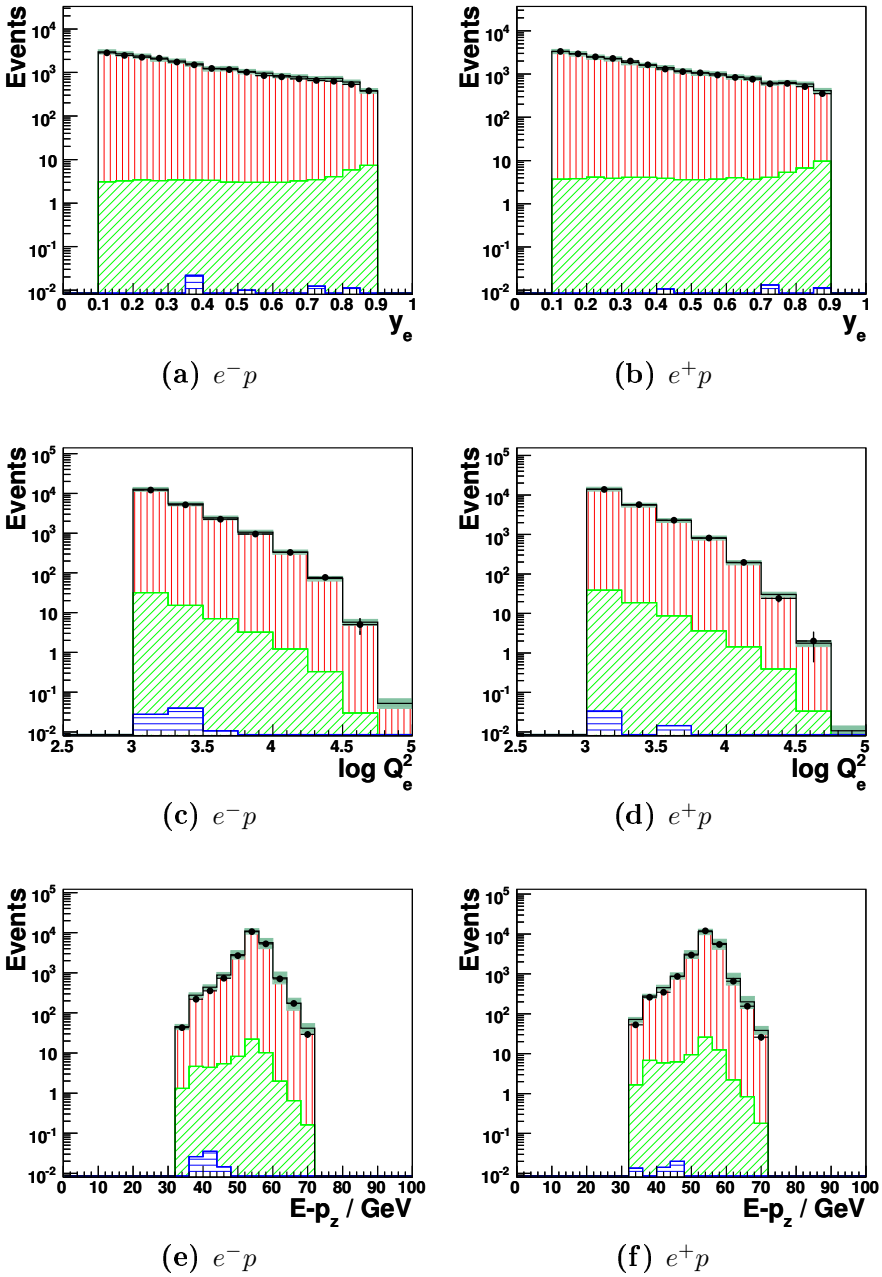


(a) $e^-p$ (b) $e^+p$

(c) $e^-p$ (d) $e^+p$

(e) $e^-p$ (f) $e^+p$

***Figure 5.11.:*** *Control plots for the neutral current selection. Shown are (a,b) inelasticity $y_e$; (c,d) momentum transfer $Q^2_e$; (e,f) longitudinal momentum balance $E - P_z$. The beam lepton type is indicated below the plots. The data are denoted by black dots. The total simulation is shown as a black histogram with the combined statistical and systematic uncertainties as a gray band. The different Monte Carlo contributions are shown as vertically hatched red area (NC), horizontally hatched blue area (CC), and diagonally hatched green area (SM bgr).*

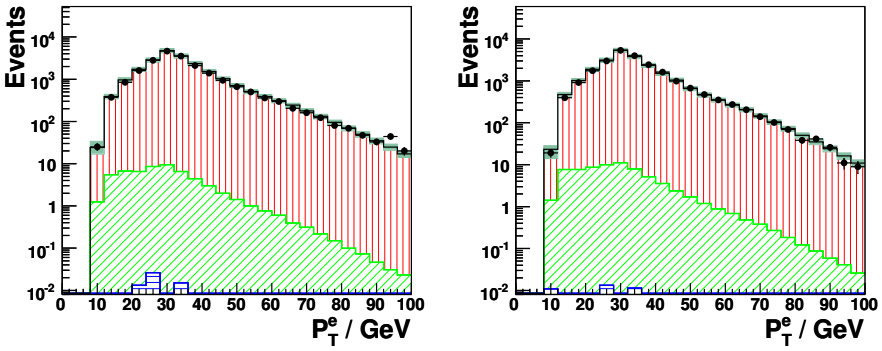


(a) $e^-p$ (b) $e^+p$

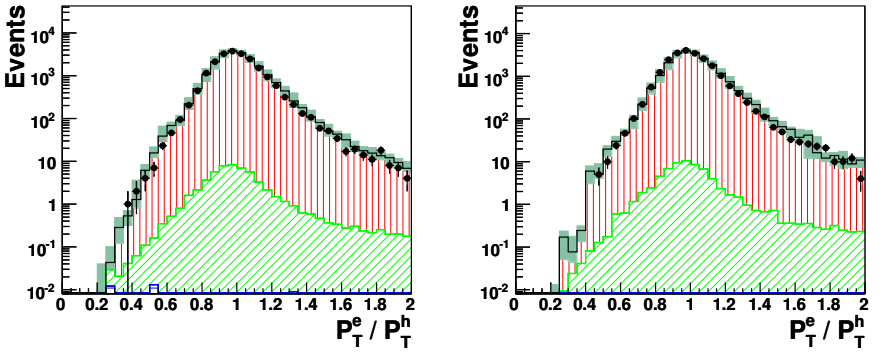


(c) $e^-p$ (d) $e^+p$

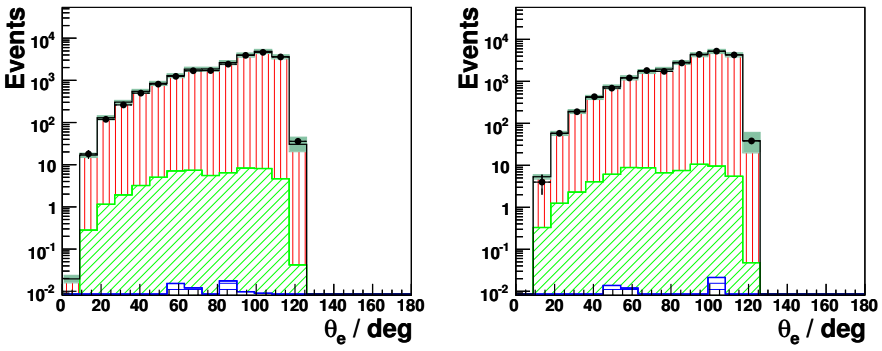


(e) $e^-p$ (f) $e^+p$

***Figure 5.12.:*** *Control plots for the neutral current selection. Shown are (a,b) transverse electron momentum $P_e^T$; (c,d) transverse momentum balance $P_e^T/P_h^T$; (e,f) polar electron angle $\theta_e$. The beam lepton type is indicated below the plots. For an explanation of the drawing style for the different simulation contributions see figure 5.11 on the preceding page.*

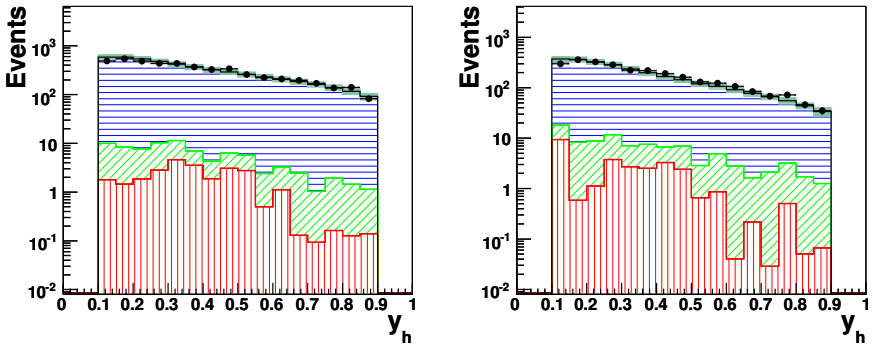


(a) $e^-p$ (b) $e^+p$

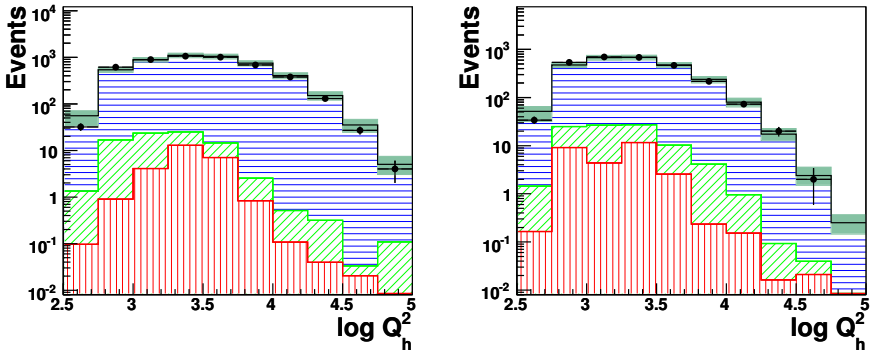


(c) $e^-p$ (d) $e^+p$

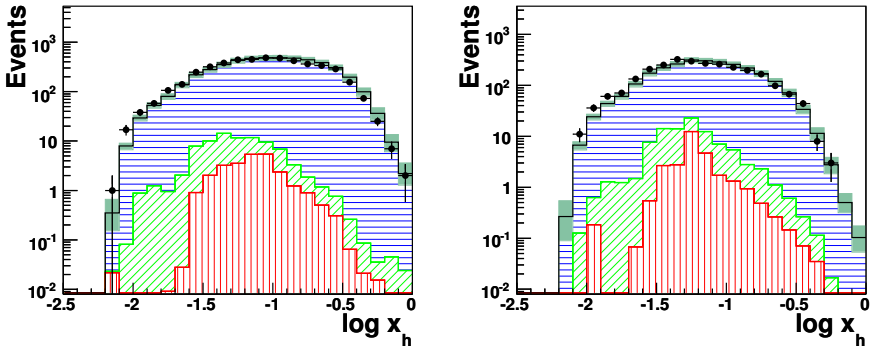


(e) $e^-p$ (f) $e^+p$

***Figure 5.13.:*** *Control plots for the charged current selection. Shown are (a,b) inelasticity $y_h$; (c,d) momentum transfer $Q_h^2$; (e,f) Bjorken scaling variable $x_h$. The beam lepton type is indicated below the plots. The data are denoted by black dots. The total simulation is shown as a black histogram with the combined statistical and systematic uncertainties as a gray band. The different Monte Carlo contributions are shown as horizontally hatched blue area (CC), vertically hatched red area (NC), and diagonally hatched green area (SM bgr).*

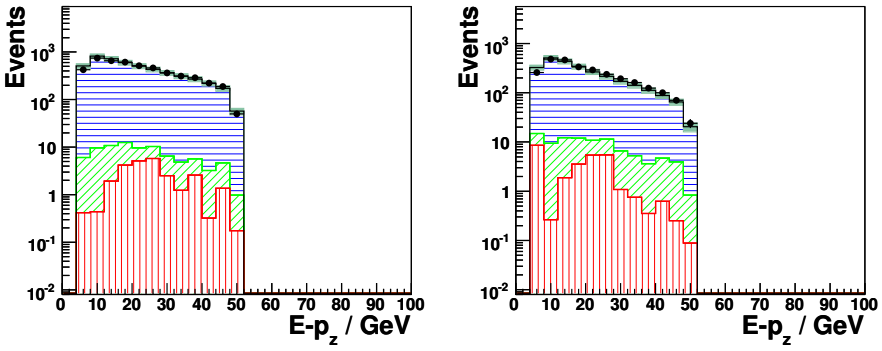


(a) $e^-p$ (b) $e^+p$

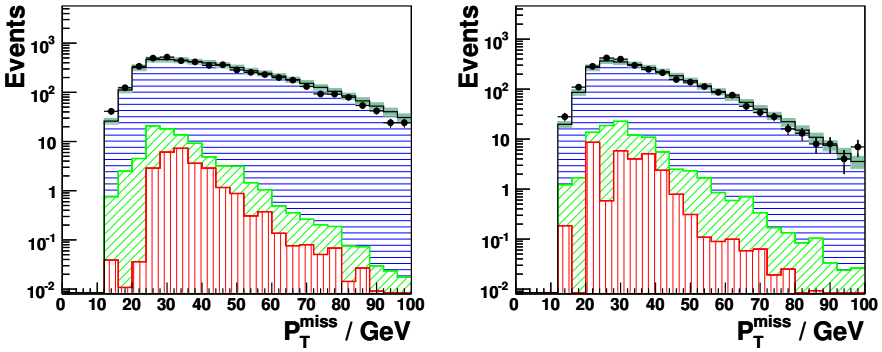


(c) $e^-p$ (d) $e^+p$

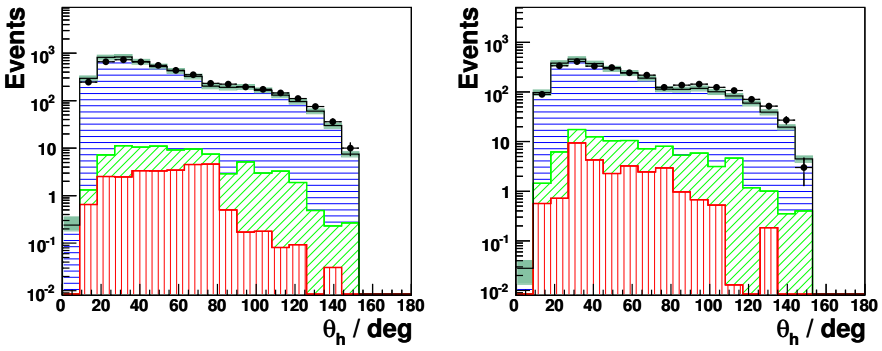


(e) $e^-p$ (f) $e^+p$

***Figure 5.14.:*** *Control plots for the charged current selection. Shown are (a,b) longitudinal momentum balance $E-P_z$; (c,d) missing transverse momentum $P^T_{miss}$; (e,f) polar hadronic angle $\theta_h$. The beam lepton type is indicated below the plots. For an explanation of the drawing style for the different simulation contributions see figure 5.13 on the preceding page.*

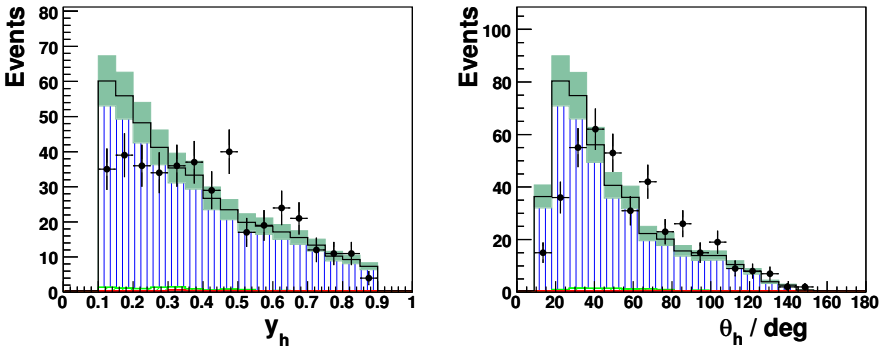


(a) 06R CC (b) 06R CC

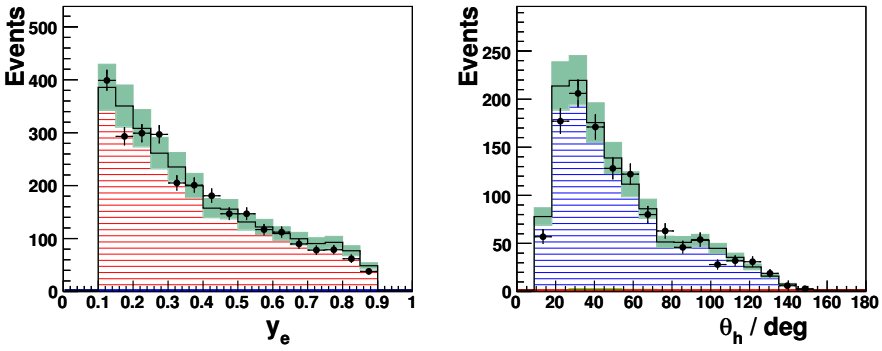


(c) 06R NC (d) 06L CC

***Figure 5.15.:*** *Problematic charged current selection in 06R period. Shown are (a) inelasticity $y_h$, and (b) hadronic polar angle $\theta_h$. For comparison (c) $y_e$ in neutral current selection in 06R runperiod, and (d) $\theta_h$ in charged current selection in 06L runperiod. For an explanation of the drawing style for the different simulation contributions see figure 5.13 on page 69.*

# Chapter 6.

# Search for Leptoquarks

In this section the neutral and charged current data selected in the previous chapter are scanned for a leptoquark signal. Since none can be found, exclusion limits are calculated for the 14 types of leptoquarks described by the BRW model. Before the limits are presented, the statistical method is introduced. The same method as in the HERA-1 publication [61] on leptoquarks is used. The limits calculated in this analysis are compared to the published results.

## 6.1. Leptoquark Signal in the Selected Data

As already discussed in chapter 2.4.2, the presence of leptoquarks in the selected neutral and charged current events should be visible in the distributions of the inelasticity $y$ and the leptoquark mass $M_{\mathrm{LQ}} = \sqrt{Q^2/y}$. The $y$-distributions have already been investigated in the previous chapter (cf. figures 5.11 and 5.13). No significant deviation from the Standard Model predictions could be observed.

Figure 6.1 shows the distribution of $M_{\mathrm{LQ}}$ for the different datasets. For leptoquark masses well below HERA's kinematic limit, resonant $s$-channel production is the preferred process, and the presence of leptoquarks should be visible in a data excess at $M_{\mathrm{LQ}}$. No such peak is visible in any dataset. For $M_{\mathrm{LQ}} \to \sqrt{s}$ both the $u$-channel and the interference of $s$-channel leptoquark production with Standard Model boson exchange become more and more important. Events originating from the former would mainly be found at low values of $M_{\mathrm{LQ}}$, while the latter may result in destructive interferences. Both phenomena may not be easily identified in the dataset. Furthermore, the absence of a clear leptoquark signal could be attributed to a very small coupling constant.

Thus, exclusion limits on the leptoquark Yukawa coupling constant $\lambda$ depending on the mass $M_{\mathrm{LQ}}$ are calculated. Before the statistical method is described, it is discussed how the leptoquark signal is modelled.

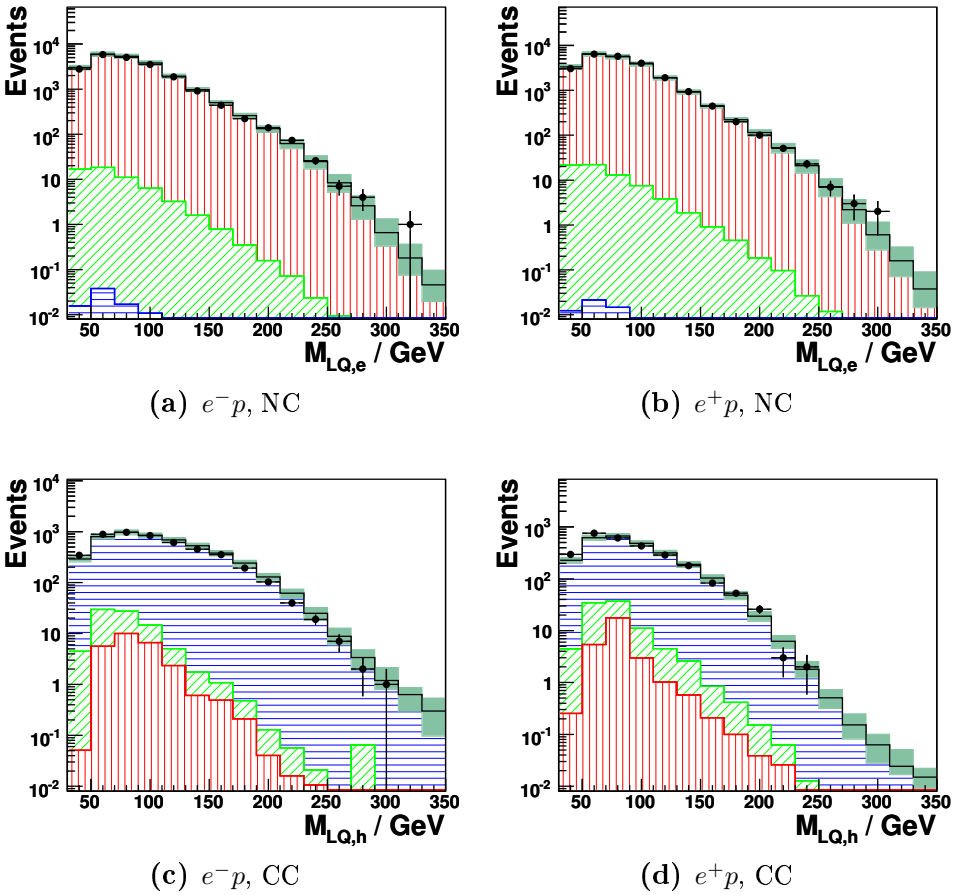


(a) $e^-p$, NC (b) $e^+p$, NC

(c) $e^-p$, CC (d) $e^+p$, CC

***Figure 6.1.:*** *Leptoquark mass for neutral and charged current selections. The beam lepton type and the selection is noted below each plot.*

## 6.2. Leptoquark Simulation

Due to several reasons no dedicated leptoquark simulation has been used in this analysis. Since the BRW model does not make any predictions on the mass and coupling constant of leptoquarks, any configuration of $M_{\mathrm{LQ}}$ and $\lambda$ needs to be simulated. Therefore, the neutral and charged current `DJANGO` simulations are reweighted to the leptoquark cross sections. Furthermore, the leptoquark cross section contains an interference term with the Standard Model processes, which means a leptoquark signal could be a *reduction* of events, in some cases. This makes it impossible to generate a *pure* leptoquark signal, and simply add this to the Standard Model predictions.

In order to reweight the neutral and charged current simulations to a leptoquark event, radiative effects have to be taken into consideration. The reconstruction of the kinematic variables $Q^2$, $x$, and $y$ as described in chapter 4.2 is only valid at Born level. Leptoquarks are produced or exchanged at the center-of-mass energy of the hard

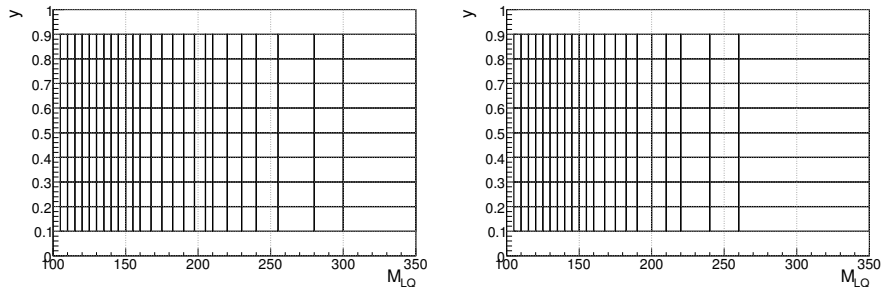


***Figure 6.2.:*** *$M_{LQ} - y$ binning used in leptoquark search: (a) neutral current, (b) charged current dataset.*

$eq$ subprocess. In case of $s$-channel processes, leptoquarks are produced at a mass of $M_{\mathrm{LQ}} = \sqrt{sx}$, with $\sqrt{s}$ the center-of-mass energy of the $ep$ interaction, and $x$ the momentum fraction of the struck quark. Because initial state radiation (ISR) of the electron may lead to a true $\sqrt{\hat{s}} < 320\,\mathrm{GeV}^2$, information about ISR photons is obtained from the Monte Carlo simulations, and the center-of-mass energy is accordingly corrected. Furthermore, ISR and final state radiation (FSR) effects may cause a misreconstruction of the kinematic variables $Q^2$, $x$, and $y$. Hence, for the Monte Carlo reweighting not the reconstructed but the generated values for these variables are used.

## 6.3. Statistical Method

For the computation of exclusion limits the method of *Fractional Event Counting* by Peter Bock is used. The introduction given in the following follows the HERA-1 publication [61] on first generation leptoquarks and focuses on the aspects relevant to this thesis. A general and profound discussion can be found in the original publication [62].

In the following the term *background* refers to *all* Standard Model processes, including neutral and charged current events, whereas *signal* denotes leptoquark events. The analysis is performed in a binned $M_{\mathrm{LQ}} - y$ plane, since these are the quantities most sensitive to the presence of leptoquarks. The binning is chosen in order to guarantee sufficient statistics in each bin [63]. Because charged current events have a lower total cross section than neutral current events, the binning chosen for the former is coarser. Figure 6.2 shows the binning used for both the neutral and charged current selections.

The number of Standard Model background events is taken from Monte Carlo simulations. Each Monte Carlo event $k$ is attributed a weight $e_k$, in order to normalize the simulation to the data. The weights applied to the Monte Carlo simulations have been described in chapter 5.10. The number of background events in bin $i$ is then given by:

$$b_i = \sum_{k \in \mathrm{bin}\ i} e_k \tag{6.1}$$

As has already been mentioned (cf. section 6.2), the leptoquark cross section contains an interference term that makes it impossible to generate a *pure* leptoquark signal $s_i$. In order to predict the number of signal-plus-background events $s_i + b_i$ in bin $i$ for a given leptoquark of mass $M_{\mathrm{LQ}}$ and coupling constant $\lambda$, a reweighting procedure is performed:

$$s_i + b_i = \sum_{k \in \text{bin } i} e_k \frac{\sigma_k^{\mathrm{LQ}} + \sigma_k^{\mathrm{INT}} + \sigma_k^{\mathrm{SM}}}{\sigma_k^{\mathrm{SM}}} \tag{6.2}$$

with $\sigma_k^{\mathrm{SM,\,LQ,\,INT}}$ denoting the differential cross sections for the Standard Model and the leptoquark processes, as well as the interference between both, respectively. Their definition can be found in [24]. The analysis is done in the binned plane of the *reconstructed* values of $M_{\mathrm{LQ}}$ and $y$. However, in order to include radiative effects, the calculation of cross section uses the 'true' information of the *generated* values from the simulation.

The method of fractional event counting uses a weighting technique in order to increase the sensitivity to signals. Each bin $i$ in the $M_{\mathrm{LQ}} - y$ plane is attributed a weight $w_i$ arising from the asymmetry between the number events in the absence and presence of a leptoquark signal:

$$w_i = \frac{(s_i + b_i) - b_i}{(s_i + b_i) + b_i} = \frac{s_i}{s_i + 2b_i} \tag{6.3}$$

In [62] it is shown how this definition for $w_i$ arises from the requirement to optimize the discrimination between the two hypotheses 'background only' and 'signal-plus-background'.

Figure 6.3 shows an example for these weights. All plots have been made for the $2005\,e_L^-$ dataset (05L). In subfigure (a) a scalar leptoquark of mass $M_{\mathrm{LQ}} = 200\,\mathrm{GeV}$ is shown. This leptoquark would predominantly be produced resonantly in the $s$-channel. As has been explained in section 2.4.2, the mass distribution of such a leptoquark would show a narrow peak around its mass value. One can see that the weights in this region are very large. Furthermore, in $s$-channel production the spectrum of the inelasticity $y$ should be flat, as opposed to the $1/y^2$ behavior of the main background process, $t$-channel photon exchange. This is reflected by the weights in subfigure (a), which show a maximum towards large values of $y$. With $s \propto 1$ and $b \propto y^{-2}$, the definition of weights (equation 6.3) leads to $s/(s+2b) \propto 1 - 1/(y^2+1)$, which is a monotonic increasing function. It is more demonstrative to calculate a simple signal-to-background ratio: $s/b \propto y^2$.

Similar observation can be made for the vector leptoquark $V_{1/2,L}$, with $M_{\mathrm{LQ}} = 200\,\mathrm{GeV}$ as well, shown in subfigure (b). It would, of course, also be prevalently produced in the $s$-channel. Hence, the weight distribution shows a maximum at the leptoquark's mass for all values of $y$. The $y$ spectrum of vector leptoquarks in resonant production is $\propto (1-y)^2$, which leads to a complex proportionality of the weights $s/(s+2b)$. An approximation yields: $s/b \propto y^2(1-y)^2$. In the logarithmic display of figure 6.3(b) this

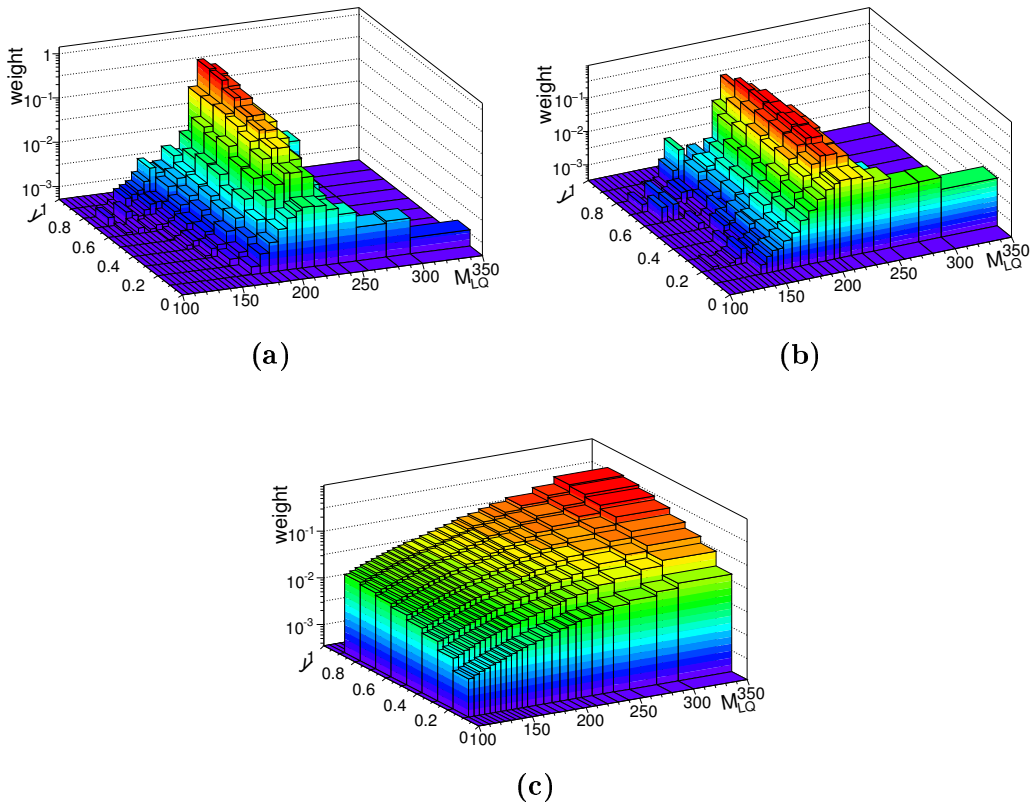


***Figure 6.3.:*** *Example of weights used in leptoquark search. The weights are shown for the neutral current selection of the 2005 $e_L^-$ dataset (05L).*
*(a) scalar leptoquark $S_{0,L}$ with mass $M_{LQ} = 200\,\mathrm{GeV}$ and coupling $\lambda = 0.02$,*
*(b) vector leptoquark $V_{1/2,L}$ with mass $M_{LQ} = 200\,\mathrm{GeV}$ and coupling $\lambda = 0.03$,*
*(c) scalar leptoquark $S_{0,L}$ with mass $M_{LQ} = 350\,\mathrm{GeV}$ and coupling $\lambda = 0.29$.*

behavior is visible as a rather flat $y$-distribution with a maximum at midrange values of $y$.

Finally, figure 6.3(c) shows the same scalar leptoquark type $S_{0,L}$ as in (a) though with a mass of $M_{\mathrm{LQ}} = 350\,\mathrm{GeV}$, that is beyond the kinematic limit of HERA. This type of leptoquark could only be produced as a virtual particle in $u$-channel exchange. Events of this type would show a very broad mass distribution extending to low mass values. This can clearly be seen in the distribution of weights.

With the help of these weights a test statistics for the selected data is defined:

$$X(\mathrm{data}) = \sum_i w_i N_i(\mathrm{data}) \tag{6.4}$$

$N_i(\mathrm{data})$ denotes the number of events reconstructed in bin $i$.

A similar test statistics can be defined for the number of background and signal-plus-

background Monte Carlo events:

$$X(b) = \sum_i w_i N_i(b) \tag{6.5}$$

$$X(s+b) = \sum_i w_i N_i(s+b) \tag{6.6}$$

A frequentist approach is chosen and a large number of pseudo-experiments (10000 each) is generated. For each experiment $N_i(b)$ and $N_i(s+b)$ are smeared by a Poisson distribution, and the test statistics is calculated. Finally, this results in two Poisson distributions $P_{s+b}$ and $P_b$. Thus, frequentist probabilities $\mathrm{CL}_{s+b}$ ($\mathrm{CL}_b$) can be defined as the fraction of pseudo-experiments, in which $X(s+b)$ ($X(b)$) is smaller than the data test statistics $X(\mathrm{data})$.

$$\mathrm{CL}_{s+b} = \int_{X<X(\mathrm{data})} P_{s+b}(X)dX \tag{6.7}$$

$$\mathrm{CL}_b = \int_{X<X(\mathrm{data})} P_b(X)dX \tag{6.8}$$

This means $\mathrm{CL}_b = 0.5$ in case the data is perfectly represented by the background-only hypothesis.

In this analysis the confidence level for the exclusion of leptoquarks is defined as:

$$\mathrm{CL} = 1 - \frac{\mathrm{CL}_{s+b}}{\mathrm{CL}_b} \tag{6.9}$$

The definition ensures that for leptoquarks with a vanishing coupling constant, which can, of course never be excluded, the confidence level drops to zero[1].

For the calculation of exclusion limits in this thesis the polarization of the beam leptons at HERA has been exploited. As has already been mentioned, in the BRW model the leptoquarks have chiral couplings, whereas the dominant background process, neutral current photon exchange, is insensitive to polarization. Hence, for leptoquarks with left-handed couplings a possible signal will be more pronounced in $e^-_L$ and $e^+_R$ datasets. Furthermore, if this leptoquark has a fermion number of $F = 2$ it will preferably couple to $e^-q$ rather than $e^+\bar{q}$. These features are used to enhance the sensitivity to the presence of leptoquarks in the data, and the datasets presented in 4.1 (cf. table 4.1 on page 38) are treated as independent channels in the limit calculation. Thus, all sums presented in this chapter do not only run over all bins of one analysis channel, but must be augmented with a second sum over all contributing channels. Channels which are especially sensitive to a given leptoquark configuration will be attributed larger weights via equation 6.3 and contribute more to the calculation of test statistics and limits.

[1] because $\lambda \to 0$ results in $\mathrm{CL}_{s+b} \to \mathrm{CL}_b$

The effect of systematic uncertainties on the calculated limits is also taken into account. Using equations 6.7 to 6.9 the confidence level for a given leptoquark configuration (type, mass, coupling) can be written as:

$$\mathrm{CL} = 1 - \frac{\int_{X<X(\mathrm{data})} dX\, P_{s+b}(X)}{\int_{X<X(\mathrm{data})} dX\, P_b(X)} \tag{6.10}$$

The systematic uncertainties are incorporated by performing an additional 300 Monte Carlo experiments for each systematic shift (cf. section 5.11). This alters the $e_k$ in equations 6.1 and 6.2, and, hence, the weights in equation 6.3. Because the test statistics for both simulation ($P_{s+b}(X)$, $P_b(X)$) and data ($X(\mathrm{data})$) are affected by the systematic shifts (equations 6.4 to 6.6), the confidence levels (equations 6.7 and 6.8) change as well. Finally, one averages over the effects of the systematic shifts on $\mathrm{CL}_{s+b}$ and $\mathrm{CL}_b$ separately. The confidence level for the exclusion of a leptoquark signal is then calculated with equation 6.10.

## 6.4. Exclusion Limits

Using the method described in the previous section, exclusion limits on the presence of leptoquarks have been calculated. They are shown in figure 6.4. The exclusion limits on the leptoquark coupling strength $\lambda$ are shown depending on the leptoquark mass $M_{\mathrm{LQ}}$. The areas above the curves are excluded at 95 %CL. A horizontal black line signifies the electromagnetic coupling strength $\lambda_{\mathrm{em}} = 0.3$. One can observe the two regimes described above: For masses well below the kinematic limit, $s$-channel production is dominating. This process has a clear peak signature, which can easily be excluded in the recorded data. For masses approaching and exceeding the kinematic limit $u$-channel exchange becomes dominating. Those processes have a very broad mass spectrum, that cannot be easily excluded for weak couplings. Between these two regimes, the limit rises over two order of magnitude. This analysis can exclude leptoquarks coupling with electromagnetic strength at 95 %CL up to masses of $M_{\mathrm{LQ}} = 280 - 300$ GeV, depending on the leptoquark type.

The limits obtained in this analysis surpass the ones in the H1 HERA-1 publication [61]. However, in the high mass region the HERA-1 limits could not be improved for all leptoquark types. For three types the limits in this range were weaker. This is documented in figure 6.5. The subfigures (a)-(c) compare the limits obtained for three leptoquark types (red line) with the published HERA-1 results (blue line). In the high mass region, that is dominated by $u$-channel exchange, the HERA-2 limit is weaker than the HERA-1 limit. In this range the analysis cannot profit from the increased luminosity during the HERA-2 runphase. Already the HERA-1 analysis was limited by systematic effects, and not by statistical errors. For the HERA-2 runperiod the systematic uncertainties are higher than for HERA-1. Especially the data recorded during 2006 and 2007 is still affected by large systematical uncertainties in the lumi-

nosity measurement. This is confirmed by subfigure (d), which shows the *expected limit* for the same leptoquark as in (c). The expected limit is calculated from simulated data only and expresses the theoretical expectation considering the luminosities, polarizations, and systematic uncertainties of the analysis' datasets. Subfigure (d) shows that even the expectation for the HERA-2 data is weaker than for HERA-1. As soon as one succeeds to reduce the systematic uncertainties for HERA-2 the limits on these leptoquarks will improve. This will also lead to an additional improvement for the other 11 leptoquarks, whose limits already are better than for HERA-1 data, in all mass regions.

In figure 6.6 the results obtained for the scalar leptoquarks $S_{0,L}$ and $S_{0,R}$ are compared with the published H1 results using HERA-1 data [61]. The limits obtained in this analysis surpass the HERA-1 results considerably. This due to both the higher integrated luminosity, and the polarized lepton beams that were available at HERA-2, and that have been used in this analysis to enhance the sensitivity to leptoquark signals.

Furthermore, figure 6.6 shows comparisons to results obtained at the L3 and D0 experiments [66, 65]. At D0 scalar leptoquarks are pair produced in strong interactions via quark-antiquark annihilation or gluon-gluon fusion. Thus, the limits obtained at D0 are independent of the Yukawa coupling, as can be seen from the figure.

At L3 leptoquarks can only be exchanged in the $u$-channel. Hence, the limit follows the behavior of the H1 limit in the high mass region. Beyond HERA's kinematic region, the limits acquired by L3 are slightly better than those calculated in this thesis. At lower mass values, however, the H1 results can benefit from the direct leptoquark production that is only possible at HERA. In this range, the limits obtained in this analysis surpass the L3 limits by an order of magnitude.

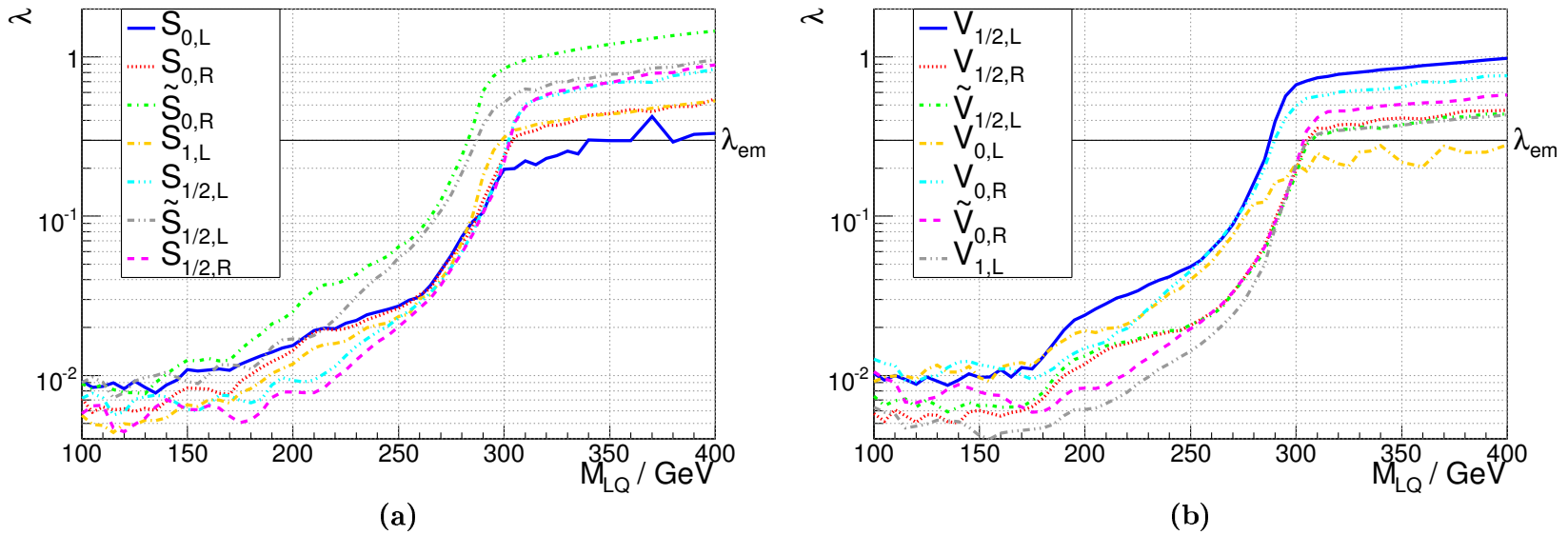


***Figure 6.4.:*** *Exclusion limits on the leptoquark coupling strength $\lambda$ depending on the leptoquark mass $M_{LQ}$ for (a) scalar and (b) vector leptoquarks (cf. table 2.1 on page 23). The area above the curves is excluded at 95 %CL. The coupling strength of the electromagnetic interaction is marked by a horizontal black line.*

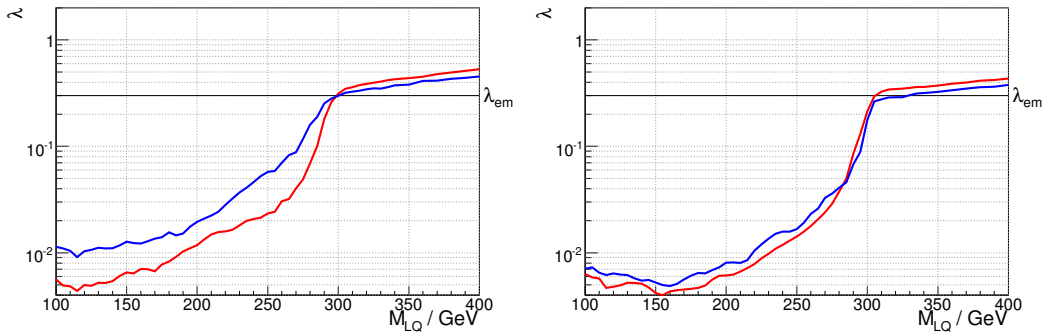


**(a)** $S_{1,L}$ **(b)** $V_{1,L}$

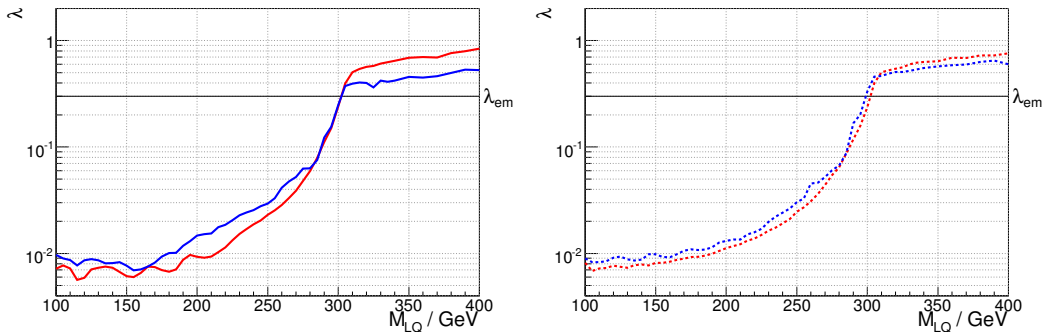


**(c)** $S_{1/2,L}$ **(d)** $S_{1/2,L}$, expected limit

***Figure 6.5.:*** *Comparison with HERA-1 results. blue line: HERA-1, red line: HERA-2.*

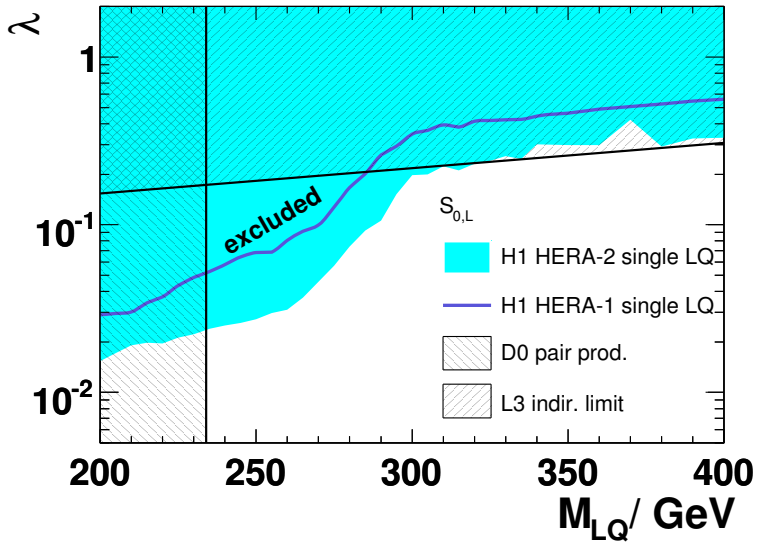


(a) $S_{0,L}$

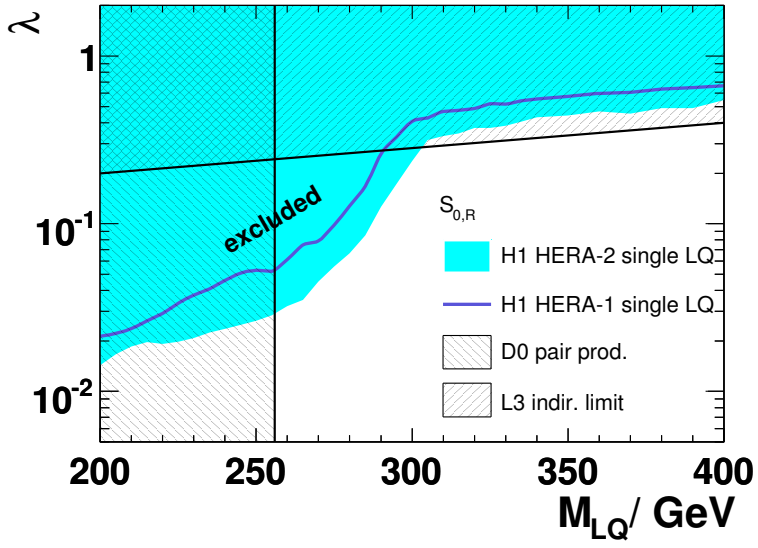


(b) $S_{0,R}$

***Figure 6.6.:*** *Comparison of exclusion limits calculated in this thesis with results from H1 using HERA-1 data [61], an indirect limit from L3 [65], and leptoquark pair production at D0 [66].*

# Part II.

# Photodetector Studies for an ILC Polarimeter

# Chapter 7.

# The ILC Compton Polarimeter

At the proposed International Linear Collider (ILC) it is aimed to measure the polarization of the electron and positron beams with an unequaled precision of $\Delta\mathcal{P}/\mathcal{P} = 0.25\%$. The measurements are to be done with Compton polarimeters. In this chapter the basics of Compton polarimetry are described. Then the layout of the planned polarimeter is introduced, and the photodetector studies presented in this part of the thesis are motivated.

## 7.1. Compton Polarimetry

A Compton polarimeter is based on the Compton scattering of polarized beam electrons off polarized laser light. The coordinate system and variables used in the following discussion are shown in figure 7.1, assuming a head-on collision between electron and photon. Furthermore, the photon polarization is expressed by the Stokes vector $\mathbf{S} = (S_0, S_1, S_2, S_3)$ and the electron polarization given in Cartesian coordinates $\mathbf{P} = (P_X, P_Y, P_Z)$, with the direction of the incident photon defining the $z$ axis.

The photon is scattered into the solid angle $\Omega = (\theta, \phi)$. The differential cross section

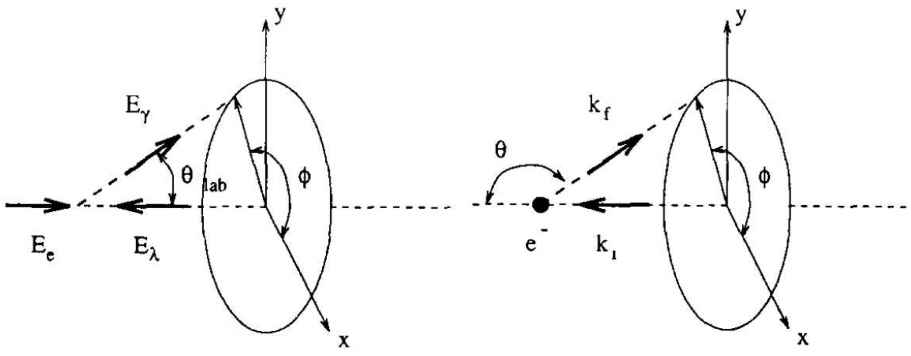


**(a)** laboratory frame **(b)** electron rest frame

***Figure 7.1.:*** *Coordinate system of Compton scattering, from [67].*

for this process is given by [67]:

$$\frac{d\sigma}{d\Omega} = \Sigma_0 + S_1(0)\Sigma_1' + S_3\big(P_Y\Sigma_{2Y} + P_Z\Sigma_{2Z}\big) \tag{7.1}$$

with

$$\begin{aligned} \Sigma_0 &= C\big[(1+\cos^2\theta) + (k_i - k_f)(1-\cos\theta)\big] \\ \Sigma_1' &= C\cos 2\phi \sin^2\theta \\ \Sigma_{2Y} &= -Ck_f \sin\phi \sin\theta(1-\cos\theta) \\ \Sigma_{2Z} &= -C(1-\cos\theta)(k_f + k_i)\cos\theta \\ C &= \frac{r_0^2 k_f^2}{2k_i^2} \end{aligned} \tag{7.2}$$

and $r_0$ the classical electron radius.

In this formula $\Sigma_0$ describes the unpolarized cross section. The second term $S_1(0)\Sigma_1'$ is dependent on the linear photon polarization. The last term accounts for circular photon polarization and both transverse ($P_Y$) and longitudinal ($P_Z$) electron polarization.

It is convenient for the discussion of Compton scattering to consider the cross section in the lab frame as a function of the scattered photon's energy $E_\gamma$ and vertical displacement $y$, instead of the rest frame scattering angle $\theta$ and azimuthal angle $\phi$. These quantities are related via:

$$\cos\theta = \frac{E_e - E_\gamma(1+1/k_i)}{E_e - E_\gamma} \tag{7.3}$$

$$y = D\tan\theta_{\text{lab}}\sin\phi \tag{7.4}$$

with $D$ denoting the distance between Compton interaction point and detector.

At the ILC the beam electrons will be longitudinally polarized, and circular polarized laser light is to be used in the polarimeter. However, inaccurate laser adjustment may lead to a nonvanishing linear photon polarization $S_1(0) \neq 0$. Furthermore, in a real accelerator distortions in the magnetic fields may cause a tilted electron spin axis, resulting in $P_Y \neq 0$. Hence, for correct calculations at a running ILC polarimeter, the full formula 7.1 has to be taken into account. In order to explain the principle of ILC Compton polarimetry in this chapter, it is assumed that $S_1 = 0$, and either $P_Y = 0$ or $P_Z = 0$.

For the cross section of transverse polarized electrons ($P_Y \neq 0$, $P_Z = 0$) only $\Sigma_0$ and $S_3\Sigma_{2Y}$ in equation 7.1 contribute. As can be seen from equation 7.2, $\Sigma_{2Y}$ depends on both angles $\theta$ and $\phi$. Hence, the cross section is dependent on both the energy and the vertical displacement of the photons (cf. equation 7.3). In order to obtain the transverse electron polarization at a collider experiment a double asymmetry between

Compton scattering processes with left and right laser polarization has to be measured:

$$\mathcal{A}(y, E_\gamma) = \frac{N_L(y, E_\gamma) - N_R(y, E_\gamma)}{N_L(y, E_\gamma) + N_R(y, E_\gamma)} \tag{7.5}$$

$$= P_Y \frac{\Sigma_{2Y}}{\Sigma_0} \tag{7.6}$$

$N_L(y, E_\gamma)$ denotes the number of recoil photons as a function of their energy and vertical displacement. The subscript denotes the laser polarization. The double asymmetry is provided by the term $\Sigma_{2Y}$, as $\Sigma_0$ is independent of the polarization. This principle was used at the transverse polarimeter TPOL at HERA.

At the planned ILC polarimeter the longitudinal electron polarization is to be measured ($P_Z \neq 0$, $P_Y = 0$). According to equations 7.1 and 7.2, only the unpolarized cross section $\Sigma_0$ and $S_3\Sigma_{2Z}$ contribute to the Compton cross section. As opposed to the measurement of $P_Y$ described above, the cross section only depends on the polar angle $\theta$ and, thus, on the energy of the backscattered photons.

The longitudinal electron polarization is obtained by measuring the asymmetry in the energy spectra of the backscattered photons with different laser helicities ($S_{3,a}$ and $S_{3,b}$, with $\Delta S = (S_{3,a} - S_{3,b})/2$).

$$\mathcal{A}(E_\gamma) = \frac{N_L(E_\gamma) - N_R(E_\gamma)}{N_L(E_\gamma) + N_R(E_\gamma)} \tag{7.7}$$

$$= \Delta S P_Z \frac{\int_y \Sigma_{2Z}}{\int_y \Sigma_0} \tag{7.8}$$

$$= \Delta S P_Z \Pi(E_\gamma) \tag{7.9}$$

Ideally one will switch between fully left- and right-polarized laser light, and thus $\Delta S = 1$. This, however has to be monitored during the polarization measurement. Via $\Sigma_{2Z}$ the asymmetry is provided by the term $\Pi$, which is often called *analyzing power*, and represents the maximum obtainable asymmetry (for $P_Z = \Delta S = 1$). Because of energy conservation the final energies of electron and photon in the lab frame ($E'_e$ and $E_\gamma$) are related to the initial energies ($E_e$ and $E_\lambda$) by

$$E'_e + E_\gamma = E_e + E_\lambda \approx E_e \tag{7.10}$$

Thus, it is equally possible to measure the asymmetry in the energy spectra of the backscattered *electrons*. This is foreseen for the ILC polarimeters. In the following it is assumed that the electrons at the ILC are only longitudinally polarized, and the following substitutions are made: $\mathcal{P}_e = P_Z$ and $\mathcal{P}_\gamma = \Delta S$.

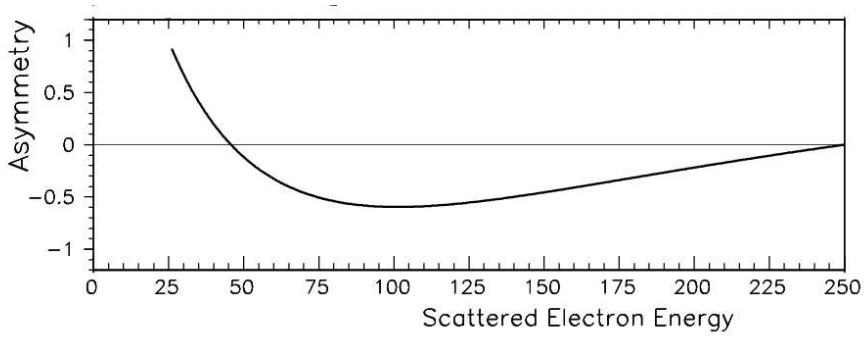


***Figure 7.2.:*** *Analyzing power for Compton scattering off longitudinally polarized electrons at a beam energy of* 250 GeV *and a green laser, from [12].*

Thus, the beam polarization at the ILC can be acquired from:

$$\mathcal{P}_e = \frac{\mathcal{A}}{\mathcal{P}_\gamma \Pi} \tag{7.11}$$

$$= \frac{\mathcal{A}}{\Pi} \tag{7.12}$$

The second equation is valid only for fully polarized laser light. The shape of the analyzing power $\Pi$ is shown in figure 7.2.

## 7.2. ILC Compton Polarimeter

For the planned linear collider ILC it is foreseen to measure the beam polarization with a precision of $\Delta\mathcal{P}/\mathcal{P} = 0.25\%$. It is advisable to use an overall of four polarimeters: both up- and downstream from the interaction point for each beam. The up- and downstream polarimeters will be complementary, as the upstream detector will be able to use much higher rates, whereas the downstream one will be sensitive to depolarization effects in the $e^+e^-$ interaction.

Since the study presented in this thesis was performed in a group working on the development of an upstream polarimeter, the following description are focused on the very same. The basic operating principle, however, is the same for the downstream polarimeters. A detailed description of the planned polarimeter scheme at the ILC can be found in [68].

The planned ILC Compton Polarimeter is to be located roughly 1800 m in front (*upstream*) of the interaction point. At this location the polarimeter can profit from clean beam conditions and low background rates to provide a fast and precise measurement. The polarimeter utilizes the polarization dependence of Compton scattering: The energy of the recoil electrons depends on the product of the photon and electron polarization.

The polarimeter is to be situated in a dedicated magnetic chicane consisting of four

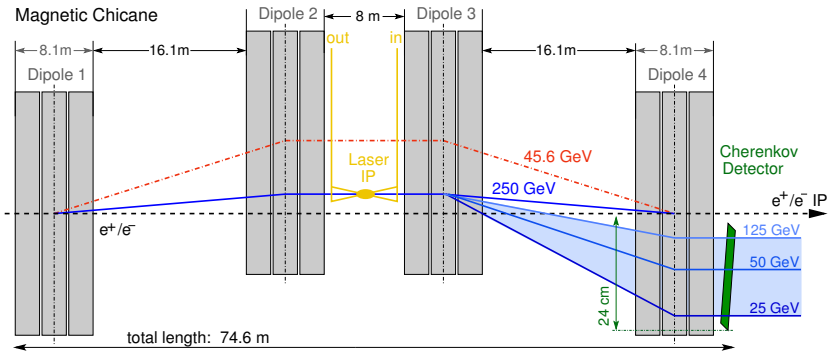


***Figure 7.3.:*** *Layout of the magnetic chicane for the ILC upstream polarimeter.*

dipole magnets, and some 70 m in length. The layout of the chicane is shown in figure 7.3. In the chicane the beam is displaced horizontally by the first two dipole magnets. Between the second and third magnet, in the center of the chicane, the Compton interaction point is situated. Under a very low angle of about 10 mrad a polarized laser is fired onto the electrons. The laser light's circular polarization can be measured with a precision of $\Delta\mathcal{P}_\gamma/\mathcal{P}_\gamma = 0.1\%$. After the Compton scattering the recoil electrons' energy spectra are dependent on the product of the electron and photon polarization. Behind the Compton interaction point the electron beam passes two further dipole magnets. The electrons that have not been interacting with the laser beam are bent back to the nominal beam axis and continue to the $e^+e^-$ interaction point. Those electrons that have taken part in the Compton scattering are deflected out of the beam line, with their energy spectrum being transformed into a spatial distribution. This spatial distribution is measured with a Cherenkov hodoscope. The general layout is shown in top view figure 7.4. The ILC is planned to have continuously tunable beam energies. This is taken into account in the polarimeter design: As shown in figure 7.3, different electron energies will mean different beam dispersions at the Compton interaction point. Thus, the laser system is mounted on a movable platform that can be adjusted to the actual beam position. With the current configuration of the chicane, the maximum dispersion will be about 12 cm at a beam energy of $E_b = 45.6\,\mathrm{GeV}$, and about 2 cm at $E_b = 250\,\mathrm{GeV}$. An alternative design foresaw tunable magnets that would have result in a fixed dispersion. This would, however, result in a jolted Compton spectrum in the Cherenkov detector with increasing beam energies. Hence, less channels could be used for measurements resulting in a degradation of precision. The chosen design using fixed magnetic fields guarantees that the Compton spectrum is spread horizontally over about 20 cm for all beam energies.

The hodoscope consists of 20 u-shaped tubes filled with perfluorobutane ($C_4F_{10}$). One of these tubes is shown in side view in figure 7.5. The gas has a high Cherenkov threshold of about 10 MeV, making it less susceptible to low energy background radiation. Other gases like propane were also considered. However, perfluorobutane has the advantages of being non-toxic and not inflammable, thus, easing security precautions.

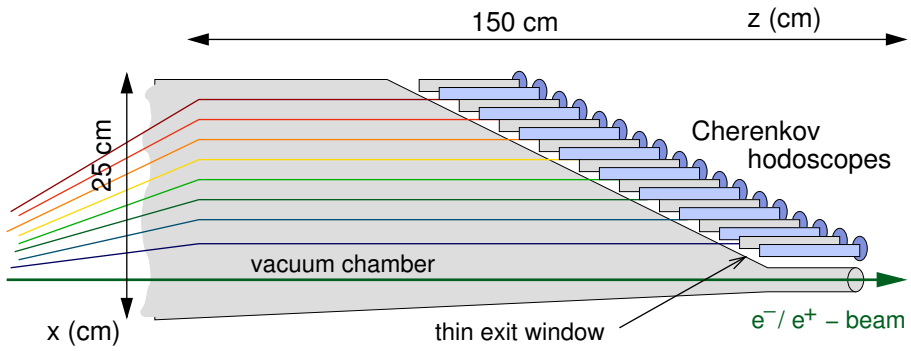


***Figure 7.4.:*** *Top view of the Cherenkov hodoscope.*

The tubes are mirrored on the inside to guide the Cherenkov light to the photodetectors. The $u$-shaped design has been chosen in order to place the photodetectors out of the beam plane, thus avoiding beam induced background radiation. In the second leg of the u-shaped tubes, an LED will be installed, in order to perform calibration measurements.

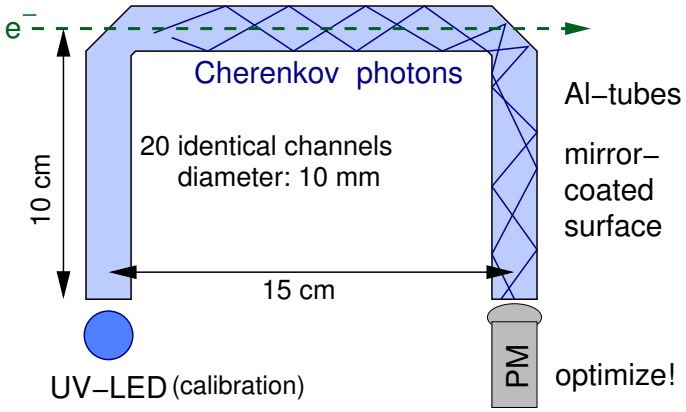


***Figure 7.5.:*** *Side view of a Cherenkov counter.*

In order to determine the beam polarization the laser helicity is flipped between $+1$ and $-1$, and the asymmetry (cf. equation 7.12) in the electron's energy spectrum is measured in the Cherenkov hodoscope. It is foreseen to pulse the laser with the same structure as the electron beam allowing to measure every bunch. The laser intensity will be chosen so that of the order of 1000 recoil electrons are expected from the Compton scattering. The statistical precision of the polarization measurement is expected to be 3% for two arbitrary bunches with opposite helicity. It is estimated that the average precision over two trains with opposite helicity will have a statistical error of $(\Delta\mathcal{P}/\mathcal{P})_{\text{stat}} = 0.1\%$ [68].

However, experiences from similar polarimeters, especially the one at the SLAC collider, have shown that the aimed precision goal is not limited by statistics but systematics, most of all the linearity of the photodetectors used in the Cherenkov detector and the calibration of the analyzing power [69, 70]. It is expected from simulations

that in order to achieve the aimed precision of $\Delta\mathcal{P}/\mathcal{P} = 0.25\%$ both effects have to be controlled to a level of 0.1 to 0.2% [71]. This is a level of accuracy that is usually not provided by the manufacturer, and few published results are available on this topic. In this second part of the thesis, methods are devised to measure photodetector nonlinearities with the required precision.

# Chapter 8.

# Instruments

This chapter gives a short introduction to two instruments that are central to the linearity measurements presented in this part of the thesis. First a short introduction to photodetectors is given. For detailed studies the book of W. R. Leo [72] is recommended, which this introduction also follows. Then the functional principle of analog-to-digital converters is explained. Finally, a definition of the different types of nonlinearities (integral and differential) as used in this thesis is given.

## 8.1. Photodetectors

In nuclear and high energy physics photodetectors are often used for the detection of particles via the measurement of light either generated through scintillation processes or, as in this part of the thesis, Cherenkov radiation. Although many different designs have been developed over the last decades, the basic principle is still the same and shall be discussed using a standard vacuum photomultiplier tube (PMT).

A schematic diagram of a typical PMT can be found in figure 8.1. Its main components are a photosensitive *photocathode*, a *dynode structure*, and finally an *anode*, from which the signal is read-out. PMTs are usually operated at a high voltage of several hundred to thousand volts. This voltage is applied in such a way to the cathode-dynode-anode structure, that a potential 'ladder' is set up. When a photon hits the photocathode an electron is emitted due to the photoelectric effect. The potential applied between the cathode and the first dynode causes this *photoelectron* to be accelerated towards the latter, which it finally hits. The kinetic energy of this incident electron is sufficient to cause several *secondary* electrons to be emitted from this dynode. By the applied voltage, this secondary electrons are, in turn, directed and accelerated towards the second dynode, where each of them transfers their kinetic energy to the electrons in the dynode. Tertiary electrons are emitted and again accelerated toward the next dynode. Thus, an avalanche is set off. When the final dynode has been reached, the emitted electron shower is directed toward the anode. Conventional PMTs have around 10 dynode stages, resulting in amplification factors (*gain*) of up to several $10^6$. Thus, the initial signal of one single electron is amplified into an electronically measurable charge.

In the following some essential parts of a PMT are introduced in more detail.

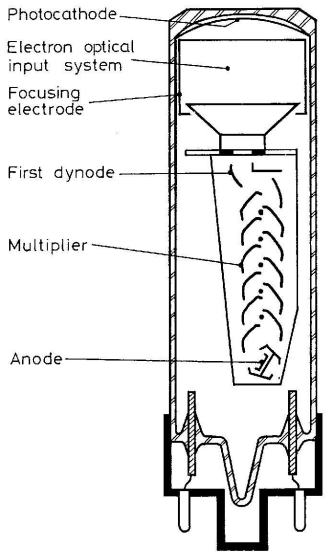


***Figure 8.1.:*** *Schematic diagram of a photomultiplier tube, from [73].*

### 8.1.1. Photocathode

The photocathode converts the incident light into a current of electrons, that can be amplified by the dynode structure. The photosensitive layer is placed on the inside of an optical window, usually made from glass or quartz. With $\nu$ the frequency of the incident photons, and $\phi$ the work function, an electron is emitted with a kinetic energy of

$$E = h\nu - \phi \tag{8.1}$$

It is well known that a minimum energy of incident light is required for this process to take place. However, even then, the probability of an electron actually being emitted is far from unity. This is quantified by the wavelength dependent *quantum efficiency*:

$$\text{Q.E.}(\lambda) = \frac{\text{number of photoelectrons emitted}}{\text{number of incident photons of wavelength } \lambda} \tag{8.2}$$

This quantity, which depends on the photocathode material, can easily be considered the most important characteristic of any PMT, as it defines the wavelength range in which this detector can be used. A large variety of photocathode materials have been developed, covering parts of the electromagnetic spectrum from infrared to the far ultraviolet.

Today most photocathodes are made of semiconductors, which have quantum efficiencies between 10 and 30%, while metals hardly surpass Q.E. = 0.1%. This is because in metals, the energy losses of the photoelectrons due to collisions with quasi-free atomic electrons are much higher.

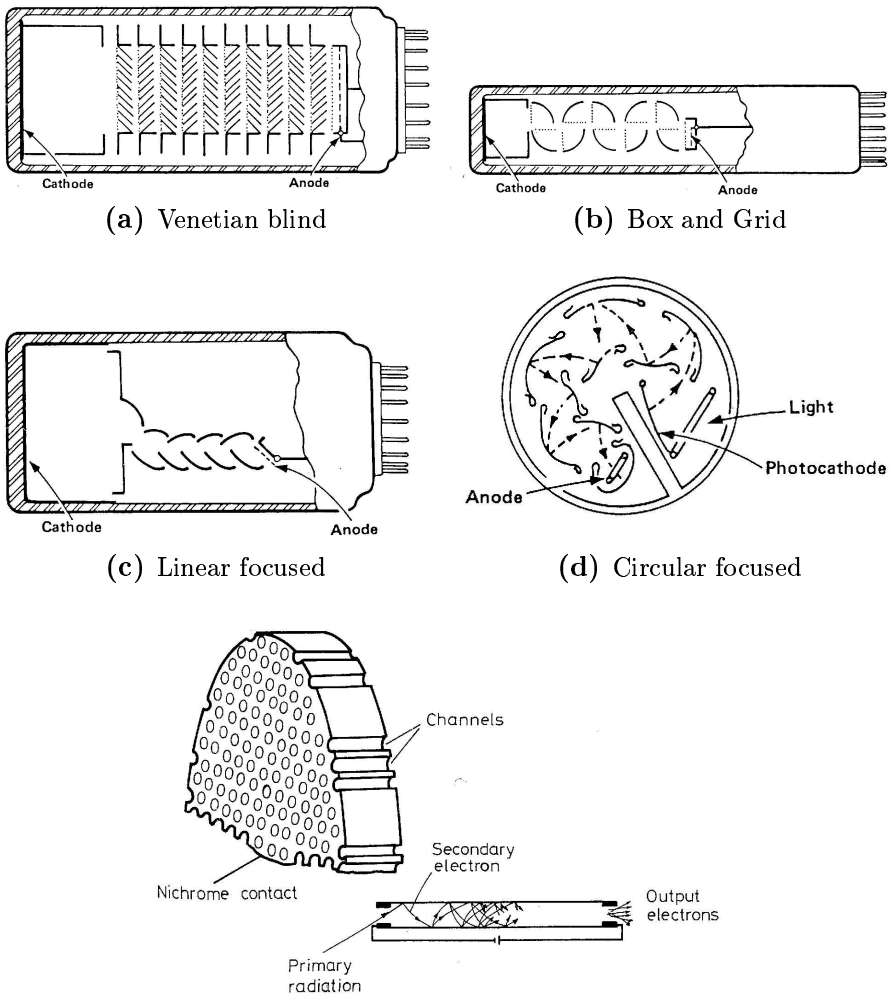


(a) Venetian blind

(b) Box and Grid

(c) Linear focused

(d) Circular focused

(e) Microchannel plate

***Figure 8.2.:*** *Different dynode structures, (a-d) from [74], (e) from [75].*

## 8.1.2. Dynode Structure

A variety of different dynode structures has been envisioned, each offering their own advantages and disadvantages: The most common ones are:

1. Venetian blind
2. Box and Grid
3. Linear focused
4. Circular focused
5. Microchannel plate

They are depicted in figure 8.2.

The Venetian blind's advantage is primarily the large input area. However, in this set up a considerable fraction of electrons will pass straight through the structure. This results in a low gain, and large spread in transit time.

The configurations (2) to (4) avoid this effect by avoiding opening a straight path for the electrons. In addition, these configurations make efficient use of space allowing more dynodes to be installed in the same volume thus increasing the gain further. Also, the risk of feedback is reduced, since cathode and anode are well isolated.

A recent development are microchannel plate dynodes. These use lead glass perforated with a large amount of microscopic channels (typically $10^4 - 10^7$ with a diameter of $10 - 100\,\mu$m each). The inner surfaces are coated with a semiconducting material, and act as a secondary electron emitter when an electron strikes the walls. A major advantage is the very compact setting, which is diminished by the low amplification factors of $10^3$ to $10^4$. However, several microchannel plates may be used consecutively if the need for higher gain outweighs space constraints.

The photomultiplier used in this analysis is equipped with a different dynode structure: a focussing mesh, which reduces the spatial spread of the secondary electron multiplication. Thus it is possible to achieve a coarse spatial resolution by segmenting the anode. This will be discussed further in section 9.2.

## 8.2. Analog-to-Digital Converters

An analog-to-digital converter (ADC) transforms an analog output signal, of a PMT for example, into a digital signal, that can be read out by digital electronics. ADCs come as two different types: *peak-sensing* or *charge sensitive*. The latter are also abbreviated QDCs. Peak-sensing convert a voltage signal that is in a certain range into a digital binary range. This type is generally used on slower signals that have already been integrated. A QDC integrates and digitizes a current input. Hence, it is used with current generating detectors like PMTs. The analysis described herein uses a QDC, and thus the following explanations focus on this type. Some terms have to be defined beforehand. The dynamic (charge) range a QDC can cover is called *full scale range*, abbreviated FSR. A signal in this range is converted into a number or QDC channel. The amount of available QDC channels is called the *resolution* of the QDC and often given as *bits*: For example, a QDC with 12 bit resolution has $2^{12} = 4096$ QDC channels. Hence, an $n$-bit QDC can distinguish input charges of $\Delta C = \mathrm{FSR}/2^n$. Ideally, for the type of QDC used in this analysis, all QDC channels are equidistant, with the smallest subdivision (one QDC channel) being called one *least significant bit* (LSB).

### 8.2.1. Operating Principle

This description focuses on the QDC used in this thesis: a CAEN V965A 8 Channel Dual Range QDC [76]. This QDC features two dynamic ranges in parallel, the basic

operating principle is, however, the same for other QDCs.

The QDC is equipped with 8 input channels, and one gate input. A block diagram is shown on the left hand side of figure 8.3 on the following page. Note that this diagram shows the CAEN V965 which features 16 input channels, but is identical in all other respects. Each input channel is connected to a QAC[1], which converts the input charge into a voltage amplitude. The QAC output is then split in two lines with one passing through a x8 gain stage. This enables the QDC to feature a double input range, with different resolutions (200 fC LSB, and 25 fC LSB), which allows to avoid saturation with big input charges, while preserving a high resolution for small inputs. The QAC outputs are then multiplexed and fed into a fast 12-bit ADC. The converted signals of all $2 \times 8$ input channels that exceed the programmable threshold values, and do not cause an overflow, are stored in a FIFO event buffer, that can be read out with digital electronics.

Figure 8.3(b) shows a sketch of the signal conversion. As soon as a `GATE` signal is applied to the QDC, a switch is closed allowing the input current to flow into the QACs. At the same time the `BUSY` flag is set by the QDC, meaning no further `GATE`s are accepted. The `CLEAR` flag is set as well permitting to abort the conversion process by sending a standard NIM signal to the `FAST CLEAR` input connector.

The input current is integrated and converted into a voltage level by the QACs. After the `GATE` signal is removed, and settling time of 600 ns, the digitization of the QAC output in the 12-bit ADCs is started. This typically takes about $6\,\mu$s. After digitization is complete, the `CLEAR` flag is removed, and the QACs are reset. This takes about 600 ns. Finally, the `BUSY` flag is removed and the QDC is ready to accept new gate inputs. The digitized information is written to the event buffer, and the `DRDY`[2] flag is set, signalling that there is data present in the event buffer, that can now be read out.

[1] charge-to-amplitude converter
[2] data ready

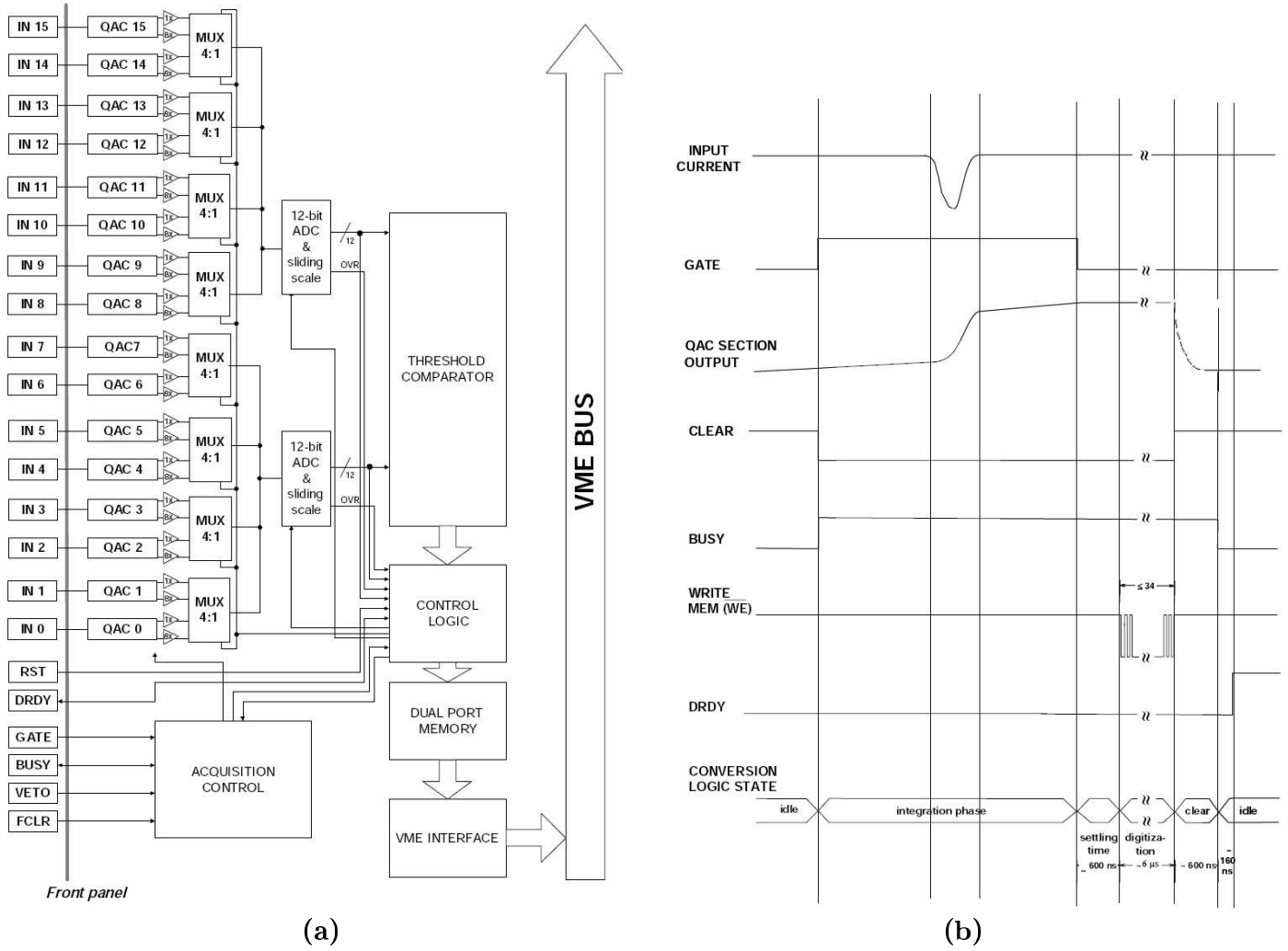


***Figure 8.3.:*** *Operating principle of a QDC (CAEN V965): (a) block diagram; (b) signal conversion timing, from [76].*

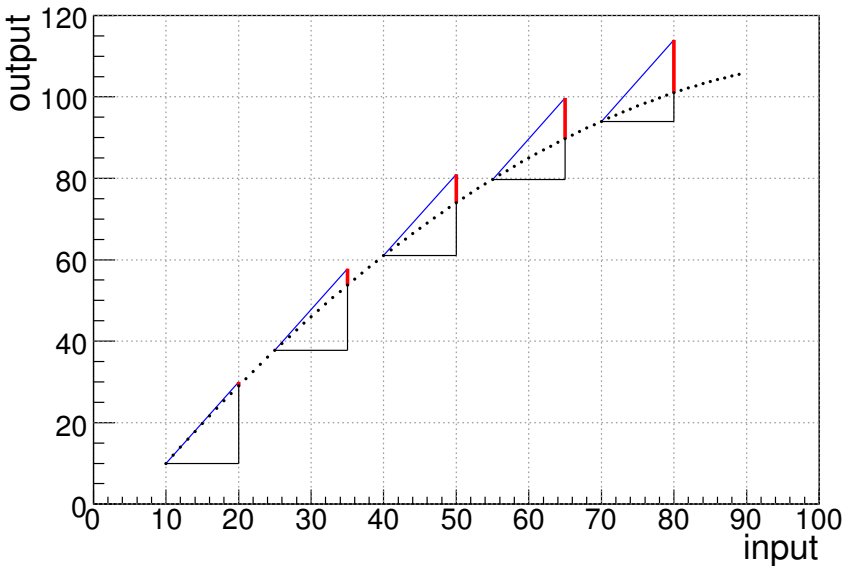


***Figure 8.4.:*** *Definition of the differential nonlinearity.*

## 8.3. Nonlinearity

When discussing the nonlinearity of a measuring device one usually distinguishes between the *differential nonlinearity* (DNL) and the *integral nonlinearity* (INL). Since different conventions are used, this section presents the definitions of DNL and INL as used in this thesis. Both properties are defined in a general way in order to be applicable to both QDCs and photodetectors.

### Differential Nonlinearity

The DNL is defined as the deviation in a device's response to a fixed change $\Delta S$ of the input signal $S_i \rightarrow S_i + \Delta S$ at different working points $S_i$. In case of an ideal, linear device the response $R_S$ to the change in the input signal is independent of the working point:

$$R_{S_i+\Delta S} = R_{S_i} + R_{\Delta S}, \quad \text{with } \frac{\partial R_{\Delta S}}{\partial S_i} = 0 \tag{8.3}$$

For a real device $R_{\Delta S}$ will depend on the working point $S_i$, and the differential nonlinearity is defined as

$$\mathrm{DNL}(S_i) = \frac{R_{\Delta S}(S_i)}{\mathcal{R}_{\Delta S}} - 1 \tag{8.4}$$

with $\mathcal{R}_{\Delta S}$ the response of an ideal, linear device.

In order to demonstrate this, figure 8.4 schematically depicts the measurement of some device's response. The device could be either a QDC or a photodetector. The output signal is shown as a function of the input signal, with the black points repre-

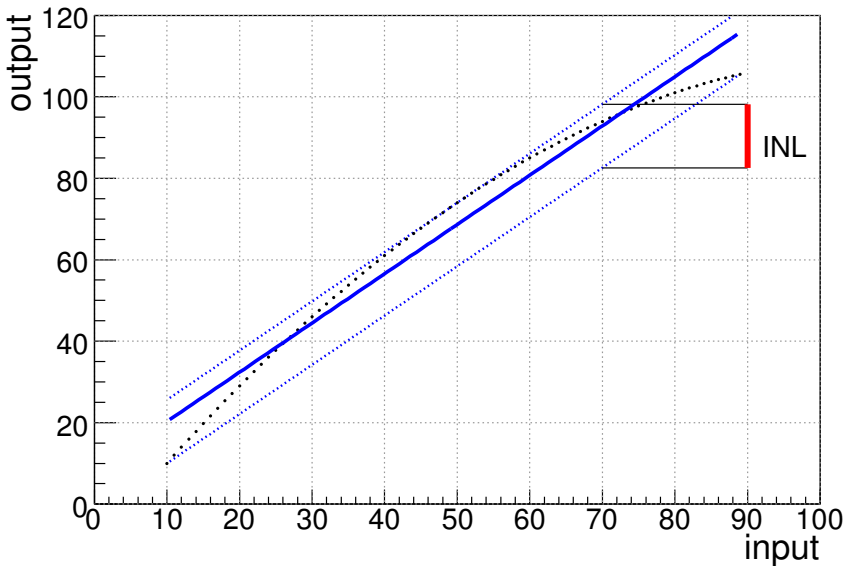


***Figure 8.5.:*** *Definition of the integral nonlinearity.*

senting the measured data. A nonlinear behavior is clearly visible.

In subfigure (a) five DNL measurements are shown. The input signal $S_i$ is increased by some fixed offset $\Delta S$, and the responses are measured in both cases, indicated by the black lines. The behavior of an ideal device is shown as a blue line. The DNL at a given working point $S_i$ is then given by the red vertical line.

In order to calculate the DNL with equation 8.4, the value $\mathcal{R}_{\Delta S}$ for an ideal device must be known. This is the case for QDCs:

$$\Delta S = \mathrm{FSR}/2^n \Longrightarrow \mathcal{R}_{\Delta S} = 1\,\mathrm{LSB} \tag{8.5}$$

for a QDC with $n$ bit resolution.

For photodetectors the response is usually unknown. In this case $\mathcal{R}_{\Delta S}$ is defined as the mean of all recorded $R_{\Delta S}(S_i)$.

### Integral Nonlinearity

The definition of the INL used in this thesis is illustrated in figure 8.5, which shows the same data points as figure 8.4.

A straight line is fitted to the data. This is shown as solid diagonal blue line in figure 8.5. The value given for the INL is then defined as the maximum deviation in the data points to both sides of this fitted line. In figure 8.5 this is depicted by the dashed blue lines, with the INL shown as bold red vertical line.

# Chapter 9.

# Testing Facility

In order to perform the measurements for this thesis, an appropriate test facility has been set up in a laboratory at DESY. In this chapter the different components are presented. The centerpiece is a light-tight box, that can be equipped with different types of photodetectors. Various optical filters can be inserted for light attenuation. LEDs serve as light sources. It can be controlled by a function generator. The data acquisition is done by a charge-sensitive ADC (*QDC*) using VME electronics. In the following sections the hardware components are introduced in more detail.

## 9.1. The Light-tight box

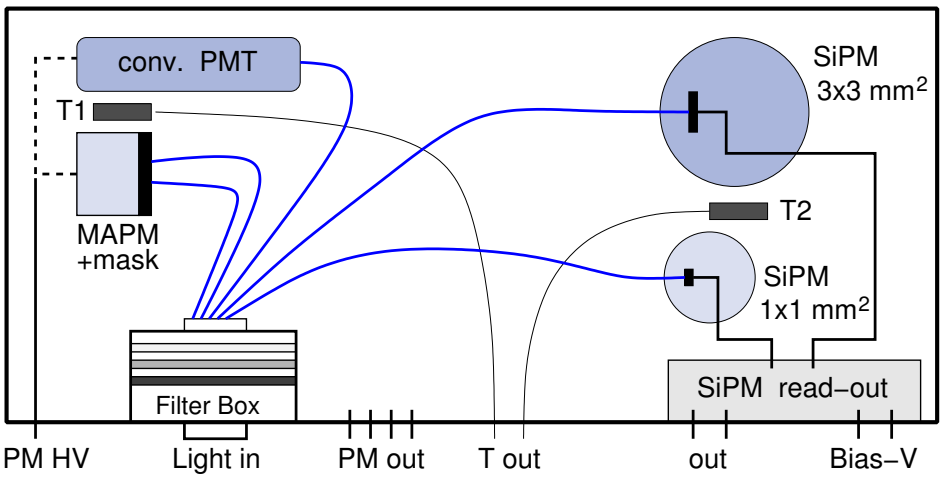


***Figure 9.1.:*** *Schematic of the light-tight box used in the measurements.*

The centerpiece of the test facility is a light-tight box. A schematic can be found in figure 9.1. Its dimensions are about $40\,\text{cm} \times 15\,\text{cm} \times 10\,\text{cm}$.

The light used in these measurements is generated by LEDs installed in a separate box (see below). By means of optical fibers, this light can be guided to a connector in the front wall of the light-tight box, denoted *Light in* in figure 9.1. Inside the box

up to three optical filters can be inserted in the light path (*Filter box*). Behind the filters the light is distributed to numerous optical fibers, and can thus be guided to a photodetector's cathode.

The box has mountings for different types of photodetectors: several types of multianode photodetectors, conventional photomultiplier tubes, as well as novel semiconductor based photodetectors. In the front wall of the box there are connectors for the photodetectors' supply voltage (*PM HV*). Several LEMO connectors (*PM out*) in the front wall of the box allow the readout of the photodetector signal.

Two Pt1000 temperature sensors are installed within the box (*T1* and *T2*), and can be read out via connectors in the front wall (*T out*). However, since these have not been used in this analysis they will not be discussed.

## 9.2. Photodetector

Several types of photodetectors can be mounted inside the box. However, since this thesis is dedicated the developement and testing of methods to measure photodetector nonlinearities at the subpercent level, all measurements have been performed on one model for comparative reasons. This photodetector will be introduced in the following.

### 9.2.1. Hamamatsu R5900U-00-M4

Although this photodetector utilizes the basic amplification principle of a conventional photomultiplier tube (see section 8.1), it has some special characteristics. The Hamamatsu R5900 is a multianode photodetector. More details on multianode photomultipliers in general can be found in [77]. The data sheet of this photodetector can be found in [82]. The most obvious difference is its compact size. Its dimensions are $30\,\mathrm{mm} \times 30\,\mathrm{mm} \times 23.5\,\mathrm{mm}$. This type of photodetector uses special *metal channel dynodes*, which are very thin, so that it is possible to install the dynode structure in a small volume. The photodetector uses a focussing mesh reducing the spatial spread of the secondary electron multiplication. Figure 9.2 shows a schematic side view of the photodetector including a typical electron cascade. The mesh structure can clearly be seen.

Because of the narrow spatial spread of electron cascades it is possible to segment the anode, thus providing the photodetector with a (coarse) position sensitivity to incident photons. The Hamamatsu R5900's anode is divided in a $2 \times 2$ grid. Every single segment is $9\,\mathrm{mm} \times 9\,\mathrm{mm}$ in size, so the effective area of the photodetector is $18\,\mathrm{mm} \times 18\,\mathrm{mm}$.

The photocathode is made of bialkali, while the window material is borosilicate glass. This results in a spectral response between 300 and 650 nm with a peak sensitivity at 420 nm. The quantum efficiency is displayed in figure 9.3(a). The peak wavelength of the LED used for the measurements in this thesis is 470 nm.

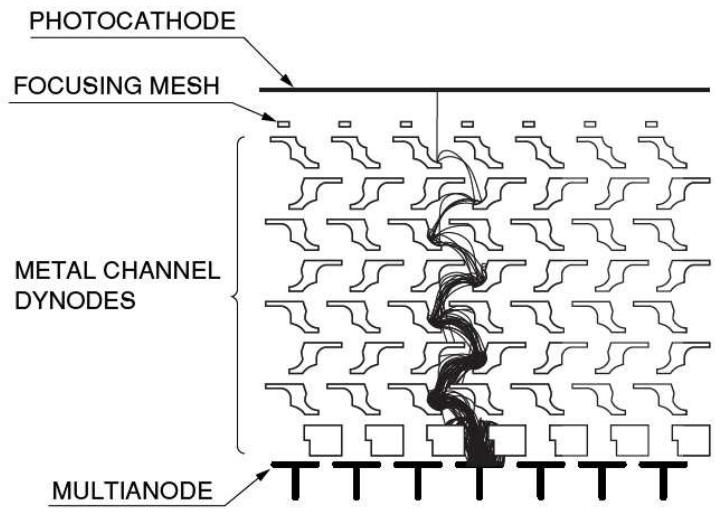


***Figure 9.2.:*** *Mesh structure of the Hamamatsu R5900, from [77].*

Figure 9.3(b) shows a plot of the gain and the dark current as a function of the supply voltage. The anode current that can be measured at a photodetector under high voltage even when no light is radiated on the photocathode is called *dark current*. This phenomenon is primarily caused by thermionic emissions within the photomultiplier tube, by scintillation photons randomly produced in the entry glass window, or leakage currents in the electric circuits of the photodetector. A detailed discussion can be found in [77]. In the measurements described herein a high voltage of 800 V has been applied, resulting in a gain of $g \lessapprox 2 \cdot 10^6$ and a dark current of $I_{\mathrm{dc}} \approx 450\,\mathrm{pA}$.

Apart from the position sensitivity this type of photodetector is also notable for its fast response. Its rise time is typically 1.2 ns, while the transit time spread (FWHM) is cited as 0.32 ns.

## 9.3. Light-emitting Diode

All light used for the measurements described herein was generated by a light-emitting diode. The LED is a HLMP-CB15 manufactured by Agilent Technologies. The data sheet can be found in [81]. Two LEDs of this type are built into a small box. The LEDs irradiate a diffuser, from which the light is fed into optical fibers and guided to the light-tight box with the photodetector.

According to the data sheet the LEDs emit blue light at a peak wavelength of 470 nm, and a spectral full-width-at-half-maximum of FWHM = 35 nm. A plot of the spectral distribution of the LED light has been generated from these values assuming a Gaussian shape. It is shown in figure 9.4.

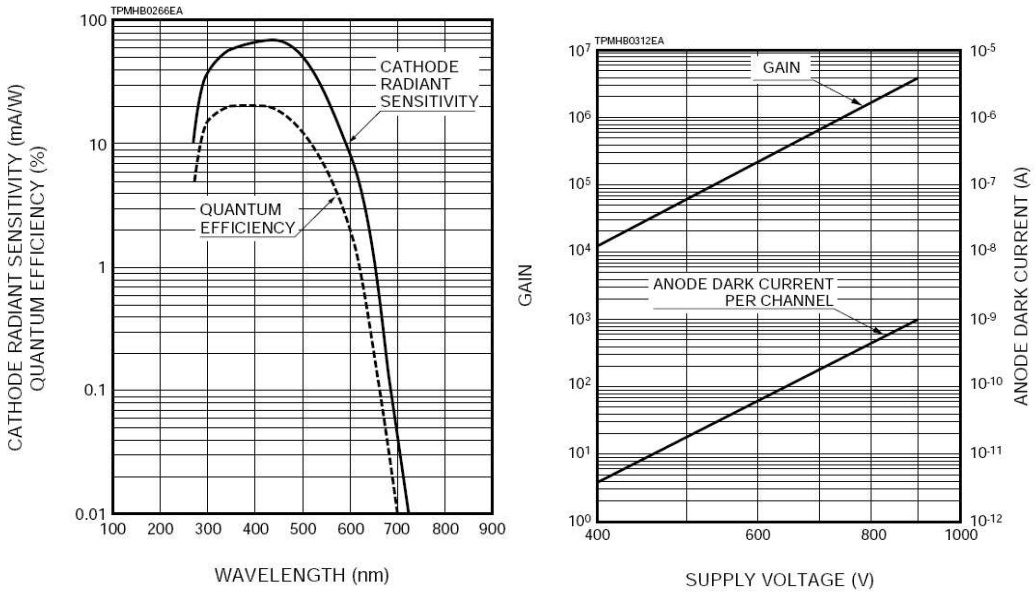


***Figure 9.3.:*** *Characteristics of Hamamatsu R5900, from [82]:*
*(a) quantum efficiency; (b) gain as a function of the supply voltage.*

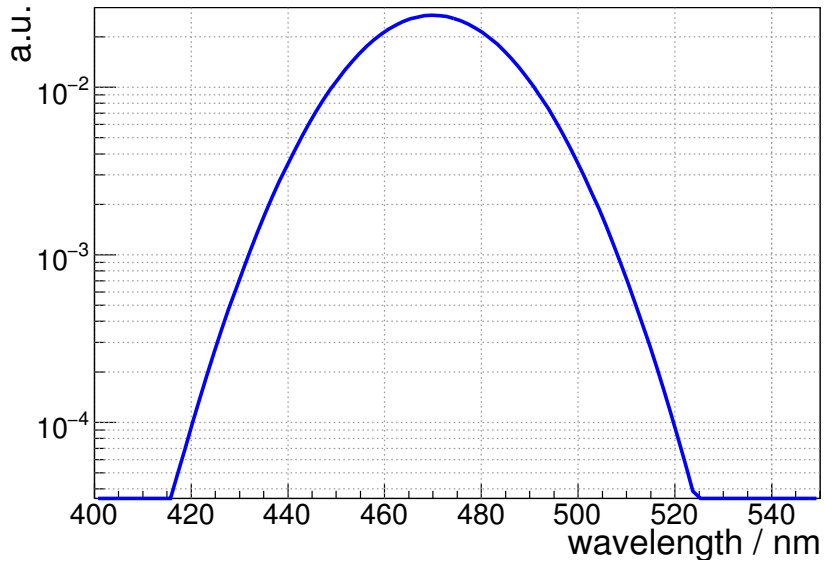


***Figure 9.4.:*** *The LED's emission spectrum, generated from parameters found in [81]. The peak wavelength is at* $\lambda_{peak} = 470\,\mathrm{nm}$.

## 9.4. Function Generator

In order to pulse the LEDs and for the generation of the QDC's readout gate a Tektronix Arbitrary/Function Generator AFG3102 was used [78]. It has two signal outputs that

can be synchronized, and one trigger output. For the wave form most commonly used in this analysis, a rectangular pulse, the data sheet cites a rise and fall time of less than 5 ns, and a typical jitter (rms) of 200 ps. For the ramp wave form used in the determination of the QDC nonlinearity a typical linearity of at worst 0.15% of the peak output is claimed. A detailed study of the precision of pulse length adjustment is described in section 10.3.2.

## 9.5. Data Acquisition

The read-out of the photodetector was done with an 8-channel 12-bit charge-sensitive analog-to-digital converter (QDC), manufactured by CAEN with the model name V965A [76]. The QDC has two input ranges and thus two different charge resolutions. One input range is from 0 to 800 pC. Since it is a 12-bit QDC this equals to a resolution of 200 fC per LSB. This range will be called *high range* in this thesis. For a higher resolution of smaller pulses, there is the *low range*. It covers input charges from 0 to 100 pC with a resolution of 25 fC per LSB. A detailed description of the electronics and the data acquisition software, that was only slightly adapted for this thesis, can be found in the diploma thesis of Ulrich Velte [79].

Apart from the nonlinearity of the photodetector, that is to be measured in this analysis, a further nonlinearity may be introduced by the QDC. In order to correct the results obtained for the photodetector (cf. section 10.3.4), it is necessary to determine the QDC nonlinearity first and to an equally precise (subpercent) level.

### 9.5.1. QDC Nonlinearity

The measurement principle that was chosen to determine the QDC nonlinearity was inspired by the *Histogram Testing Method* described in [80]. This method uses a long low frequency input signal (typically some Hertz) generated by a function generator. This signal is sent to the input connector of the QDC channel to be tested. The read-out is done by using a short high frequency random gate (typically some Kilohertz). The gate has to be short compared to the period of the input signal in order to get a high sampling rate of the input signal. A fast random gate is chosen to avoid phase effects in the recorded spectra, similar to the optical Moiré effect. A ramp signal has been used as input.

The input ramp wave form was generated in the first output channel of the function generator. The amplitude was chosen so that in the QDC's high range all channels up to about 1500 QDC counts were covered. The frequency was 10 Hz. In order to randomly trigger the gate, a white noise signal was generated in the second output channel of the function generator. This signal was fed into a NIM gate generator. This device produces a rectangular output signal, each time the input signal exceeds an adjustable threshold. The width of this signal can be chosen, the amplitude is NIM standard $\approx -800$ mV.

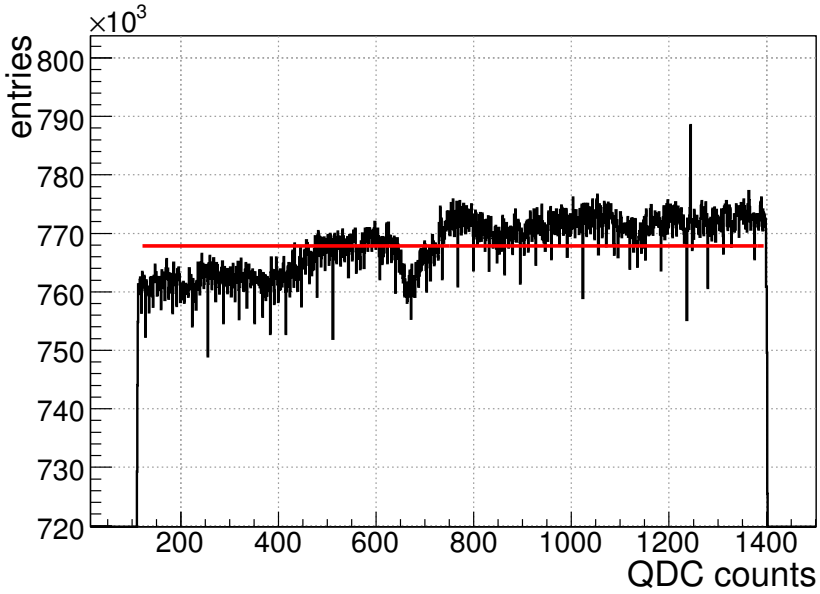


***Figure 9.5.:*** *Histogram Testing Method. The red line represents an ideal, completely linear QDC. This histogram shows the QDC's high range, that means* 1 LSB ≡ 1 *QDC count* = 0.2 pC.

The amplitude and offset of the white noise was then adjusted, so that an adequate rate was achieved for the NIM generated gate. The frequency chosen for the gate was about 20 kHz, meaning that an average of 2000 samples were recorded per single ramp. A total of $10^9$ gates were read out.

The recorded spectrum is shown in figure 9.5. The histogram in the figure shows the QDC's high range, which in this case means for the least significant bit 1 LSB = 0.2 pC. The horizontal red line represents an ideal, completely linear QDC, for which every bit width is exactly one least significant bit. This line was determined by dividing the total number of samples recorded in an interval of QDC counts by the number of QDC channels therein. The range of the interval was chosen a little bit smaller than the complete width of the recorded spectrum, in order to avoid artifacts from the function generator. These artifacts may appear because of the choice of a discontinuous input function. By a Fast Fourier Transform all output signals of the function generator are internally generated via superpositions of sine waves. For a discontinuous function this process can only be an approximation with oscillations appearing at the discontinuous points, so called artifacts.

The differential nonlinearity of a QDC is defined as the ratio of the actual and the ideal bin width. Every bin content in the recorded histogram in figure 9.5 is divided by the value of the ideal distribution, represented by the red line in the figure. The results are depicted in figure 9.6.

The differential nonlinearity in units of least significant bits is displayed in the QDC range between 115 and 1400 QDC counts. The distribution shows a positive slope. Low

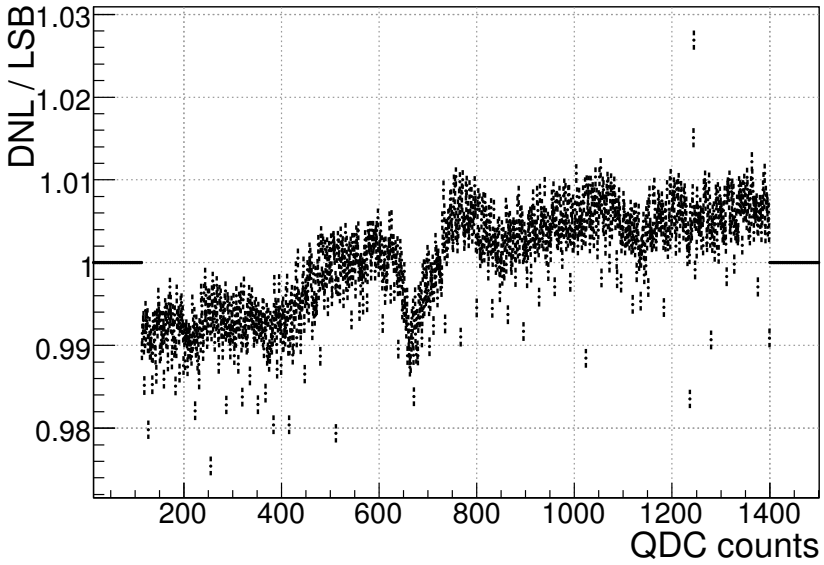


***Figure 9.6.:*** *Differential nonlinearity of the QDC in units of least significant bits. In this case, the QDC's high range, this means* $1\,\mathrm{LSB} = 0.2\,\mathrm{pC}$.

QDC bins generally seem to be smaller than the ideal bin width, whereas higher QDC bins are broader. The most prominent feature is a broad dip at about 700 QDC counts. Except for some outliers the differential nonlinearity for all tested QDC bins does not differ more than 0.01 LSB from the ideal bin width. However, cumulative effects can appear. They are taken into account by the integral nonlinearity.

In order to acquire the integral nonlinearity for bin $n$, the differential nonlinearity is summed up to the $n$th QDC bin. The results of this procedure are shown in figure 9.7. This figure shows the integral nonlinearity in units of least significant bits. A nonlinearity of 3 LSB is found. A more demonstrative way of plotting the integral nonlinearity was chosen in figure 9.8 on the next page, where it is shown in percent. The integral nonlinearity for bin $n$ was calculated by summing up the differential nonlinearity up to bin $n$, and additionally dividing the sum by the number of contributing bins: $n$. A nonlinearity of about one percent is observed in the low bins of the QDC.

In figure 9.7 the integral nonlinearity starts and ends at a value of zero. This is inherent to the method. The expected *ideal* number of entries per QDC bins was assumed to be the average over the range considered. This means that the cumulative distribution of the integral nonlinearity has to have the same start and final value - zero - because over the entire range, all deviations cancel out. The measured integral nonlinearity should therefore be considered a relative value. The absolute distribution can still be shifted by a constant offset. However, the result of a nonlinearity of one percent still holds.

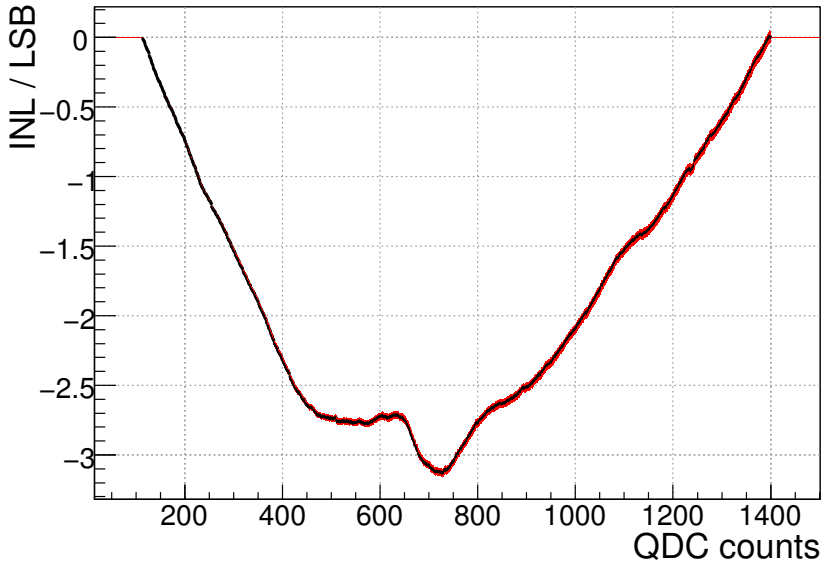


***Figure 9.7.:*** *Integral nonlinearity of the QDC in units of least significant bits. In this case, the QDC's high range, this means* $1\,\mathrm{LSB} = 0.2\,\mathrm{pC}$.

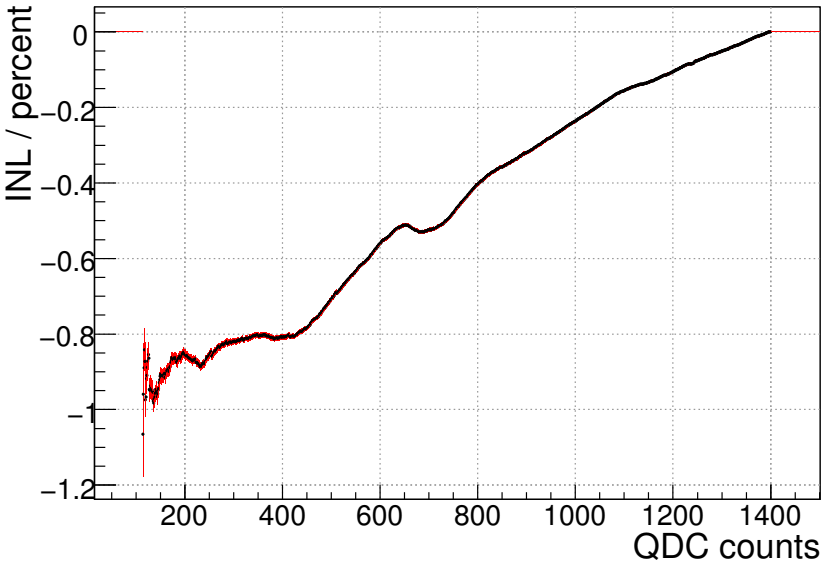


***Figure 9.8.:*** *Integral nonlinearity of the QDC in percent.*

## 9.5.2. Correction of Recorded Spectra

The QDC nonlinearity has been measured in order to correct the photodetector spectra recorded later on. In this section it is shown how the QDC correction affects a typical photodetector spectrum. The photodetector measurements are explained in detail in

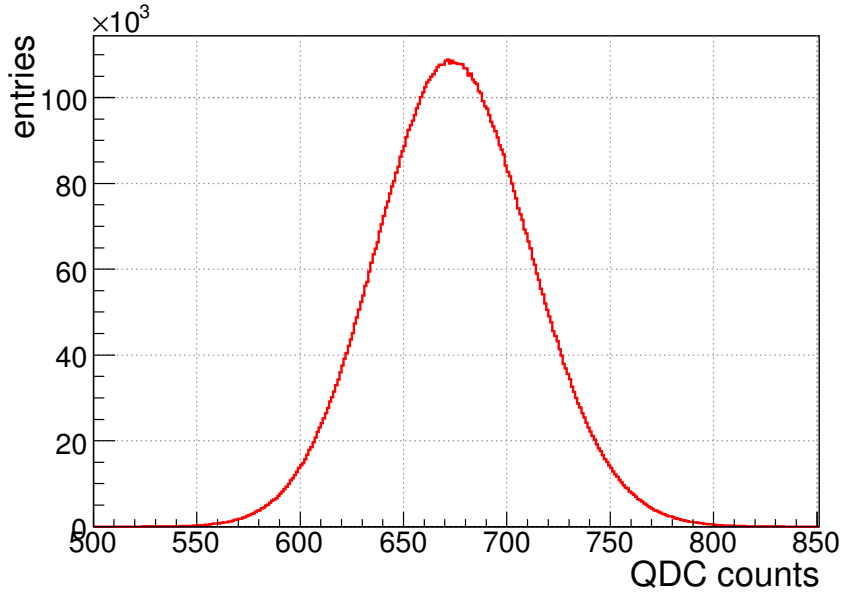


***Figure 9.9.:*** *A typical photodetector spectrum as recorded by the QDC used in this analysis. In this case, the QDC's high range is shown.*

chapter 10.

Figure 9.9 shows such a spectrum. A photodetector has been irradiated with light from an LED. A fixed pulse length has been used, and a total of $10^7$ pulses have been recorded. The spectrum does not have a sharp peak, but shows a Gaussian shape. This is caused by fluctuations of parameters like the number of photons produced in the LED, the quantum efficiency of the photocathode, and variations in the gain of the photodetector.

The differential QDC nonlinearity is now applied to this spectrum. This is done by weighting the content of each QDC bin by the inverse of the differential nonlinearity (figure 9.6). Thus, the contents of bins that are wider than the bin width of one least significant bit are reduced to the value that would be recorded if they had the ideal width, and vice versa.

Figure 9.10 on the next page shows the effect of this correction on the spectrum shown in figure 9.9. The dotted red histogram denotes the original, and the solid blue histogram the corrected distribution. Only the region between 650 and 700 QDC counts is shown, since this is where largest differences can be observed. It is also the region where the distribution of the differential QDC nonlinearity (figure 9.6) has its most irregular shape - the broad dip. Still, the changes are minute, as can be expected since the differential QDC nonlinearity is less than 0.01 LSB in most bins.

A check was performed on a series of 25 recorded photodetector spectra, similar to the one shown in figure 9.9, with varying QDC input charges (i.e. different peak positions of the spectra). A Gaussian function was fitted to both the corrected and uncorrected spectra, and the effect of the correction on two fit parameters were studied. The results

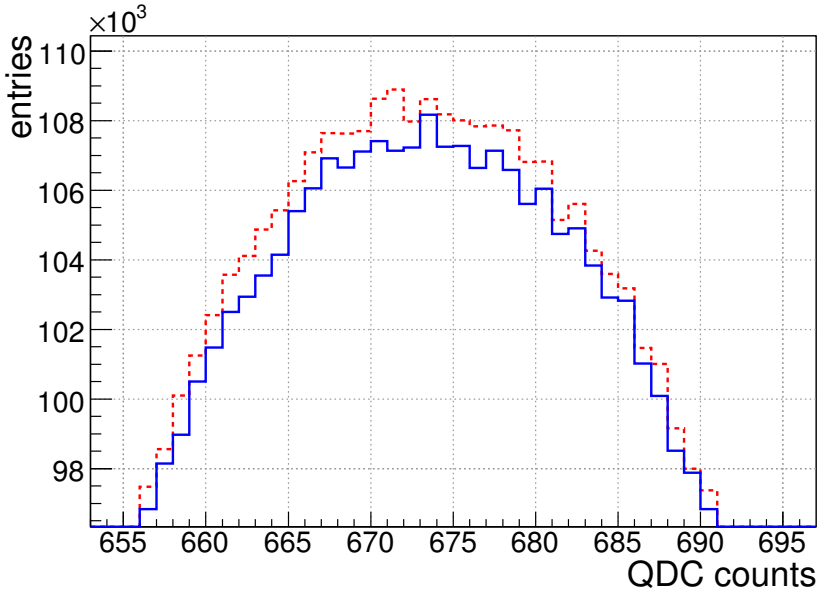


***Figure 9.10.:*** *Effect of correcting for the QDC nonlinearity on a typical photodetector spectrum. The dotted red histogram denotes the original, and the solid blue histogram the corrected distribution.*

are demonstrated in figure 9.11 on the facing page. In subfigure (a) the change in the reduced $\chi^2$ is shown. With one exception, the values for the corrected spectra are closer to unity. Thus, the QDC correction causes the signal to become more Gaussian-like. The effects on the peak position of the spectra, however, is minute. Subfigure (b) depicts the relative change in peak position $(S^\star - S)/S$ between the corrected and uncorrected signal $S^\star$ and $S$, respectively. The observed shifts are for the most part below 0.2 permille level. Only in proximity of the larger dip in the QDC nonlinearity (cf. figure 9.6) at about 600 to 700 QDC-counts, the correction causes a peak position shift of up to 0.5 permille.

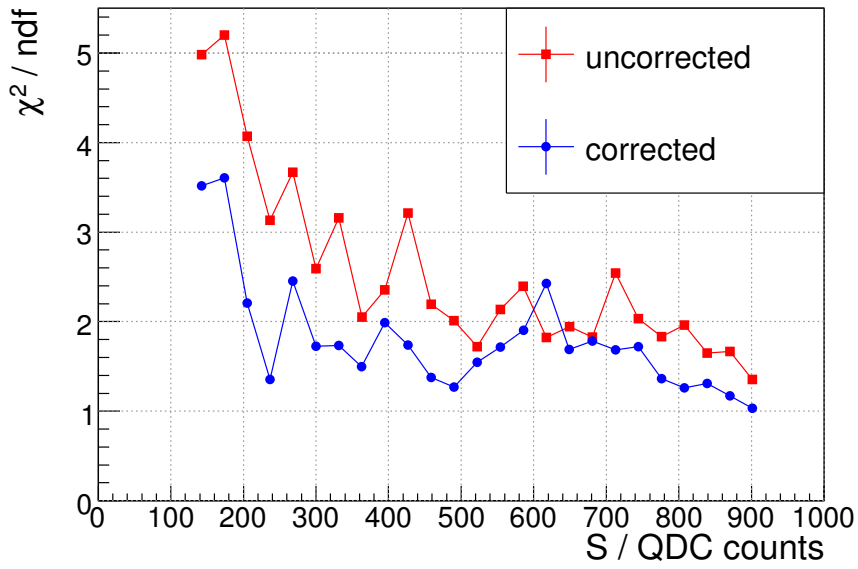


(a)

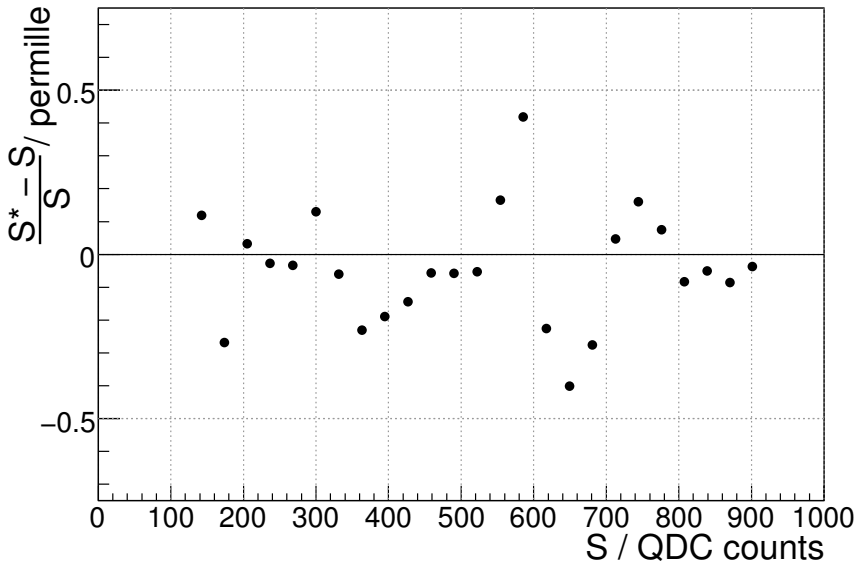


(b)

***Figure 9.11.:*** *Effect of correcting for the QDC nonlinearity on the parameters of a Gaussian fit to a typical photodetector spectrum (cf. figure 9.10). (a) reduced $\chi^2$; (b) relative change in peak position between corrected ($S^\star$) and uncorrected ($S$) signal. The effects are shown for a series of 25 photodetector measurements with varying QDC input charges.*

# Chapter 10.

# Photodetector Measurements

The prime task of this part of the thesis is to determine the photodetector nonlinearity to a level of precision of the order of $10^{-3}$. This chapter details on the several methods devised to achieve this goal.

In order to measure the photodetector linearity, an LED is used as light source. To be able to determine the photodetector's response at the permille level, it is obviously necessary to control the light yield of the LED to at least the same level. This cannot be done by simply varying the voltage applied to the LED, or changing the current, because the absolute calibration of the LED is not known to that precision. So several methods have been devised to ensure a linear variation of the amount of light on the photocathode. However, before these are discussed some basic remarks concerning the measurements shall be given.

## 10.1. General Remarks

All measurements described in this chapter were performed with a *Hamamatsu R5900* multi-anode photomultiplier (see section 9.2 on page 104 for technical details). It has four anodes that can be read out independently. All measurements used the same anode.

It has turned out that it is essential to take into account the warm-up phase for both the photodetector and the LED. So the photodetector was switched on five hours and the LED two hours prior to a series of measurements.

The term *series of measurements* refers to the full application of one of the methods described below. It consists of several *measurements*, in which one parameter is changed from one measurement to the next. In order to minimize the statistical error, 10 million events were recorded for each measurement.

In general, in all of the methods described below, the photocathode is illuminated by an LED, whose light is guided to the photodetector by optical fibers. It is ensured that the photocathode is uniformly radiated. The photoelectrons emitted in this process are then amplified in the dynode structure of the photodetector. Finally, a charge $Q_{\mathrm{A}}$ is collected at the anode, which should be proportional to the number of incident photoelectrons, and thus proportional to the amount of incident light (see section 8.1). The task of this analysis is to determine to which level this proportionality holds.

### 10.1.1. Photodetector Signal Modeling

The spectra that are recorded by a QDC and read out by a PC have to be fitted to a model in order to reconstruct the anode charge $Q_\mathrm{A}$ or the number of incident photoelectrons $N_\mathrm{p.e.}$. Both quantities can then be used to analyze the linearity of the photodetector's response to the incident light. Two different ansatzes have been chosen to model the photodetector signal, and are described in the following.

#### Multi-Poisson Model

The emission of electrons at the photocathode is a statistical process, so the number of photoelectrons $n$ follows a Poisson distribution with a mean value of $N$:

$$f(n) = C \cdot \frac{\exp(-N) \cdot N^n}{\Gamma(n-1)} \tag{10.1}$$

with some normalization constant $C$, and $\Gamma(n-1)$ denoting the Gamma function.

The number of photoelectrons $n$ can be expressed in terms of the (digitized) anode charge as measured with the QDC ($Q_\mathrm{QDC}$, in QDC counts):

$$n(Q_\mathrm{QDC}) = K \cdot (Q_\mathrm{QDC} - P)/(g \cdot e) \tag{10.2}$$

with $g$ and $P$ denoting the gain and dark current of the photodetector, respectively, and $e$ the elementary charge. $K$ is the conversion factor of the QDC, which is 200 fC per QDC count in the QDC's high range considered in the following results.

Combining both equations the measured QDC spectrum can be described. This function has four parameters: $N$, $g$, $P$, and $C$. However, $P$ has been measured separately to be $P = 62.5$ QDC counts, and can thus be fixed. When analyzing a series of measurements, with a variable LED pulse length for example as described in 10.3, it is advisable not to treat the gain as an independent variable in every measurement. Instead of fitting each measurement separately, all measurements were fitted simultaneously using only one parameter $g$. This means a *Multi-Poisson* fit to a series of $n$ measurements has $2n + 1$ free parameters ($C_i$ and $N_i$ for each measurement and one gain parameter $g$).

Figure 10.1 shows an example of this kind of fit. The data shown were recorded with the *Pulse Length Measurement* (see section 10.3.1 on page 126 for details). All 25 measured photodetector spectra were filled into *one* single histogram with an offset of 2000 QDC counts between each individual signal. A Multi-Poisson function is then fitted to this histogram. The fit shows good convergence: $\chi^2/\mathrm{ndf} = 13406/8245 \approx 1.626$. Subfigure (b) shows an extract of the fitted values of the free parameters. The number of photoelectrons in the respective measurement is denoted by `muX` (with `X` between 0 and 24). The parameter `eff_gain` is the *effective gain* $g_\mathrm{eff} = g \cdot e/K$ (compare equation 10.2). The fitted value of $g_\mathrm{eff} = 2.265$ corresponds to a gain of $g \approx 2.8 \cdot 10^6$. This is somewhat higher than the value of $\lessapprox 2 \cdot 10^6$ read off the plot in the manual (cf.

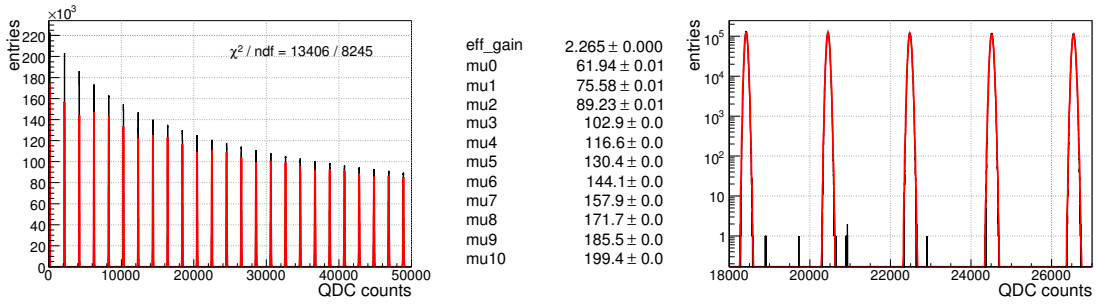


**(a)** full view **(b)** fit values **(c)** zoomed view

***Figure 10.1.:*** *Example of Multi-Poisson fit method: The measured photodetector signals are filled into* one *histogram every 2000 QDC counts. A Multi-Poisson function is fitted to the entire spectrum simultaneously. The fit converges well:* $\chi^2/ndf = 13406/8245 \approx 1.626$.

figure 9.3 on page 106).

The advantage of this fit method is that it is possible to determine both the number of photoelectrons produced at the cathode and the gain of the photodetector. However, for the purposes of this analysis it is already sufficient to determine the photodetector linearity against the output charge. Furthermore, the Multi-Poisson method proved to be time consuming and very susceptible to slight changes in the initial conditions of the fit. This is why a second, more robust fitting model was devised:

### Gaussian Model

Although the photodetector signal follows a Poisson distribution for the light intensities (number of photoelectrons) considered in this analysis, it can be approximated by a Gaussian in a narrow interval around its peak. A fit range of ±1rms around the peak position was chosen. Checks have confirmed that larger intervals do not change the fit results. This is valid, since in the scope of this analysis, it is not necessary to accurately describe the shape of the recorded signal. Although the gain is an interesting quantity, the main figure of interest is the output charge of the photodetector designated by the peak position of the signal. In order to determine this, it is easily sufficient to use a Gaussian fit around the peak of the signal. The mean of the Gaussian then equals the anode charge measured by the QDC $Q_{\mathrm{QDC}}$ shifted by an offset that is given by the dark current of the photodetector $P = 62.5$ QDC counts. Using the QDC's conversion factor $K$, the anode charge $Q_A$ can be calculated from:

$$Q_A = \frac{Q_{\mathrm{QDC}} - P}{K} \tag{10.3}$$

For all results presented herein the dark current subtraction and QDC conversion has always been performed in this form.

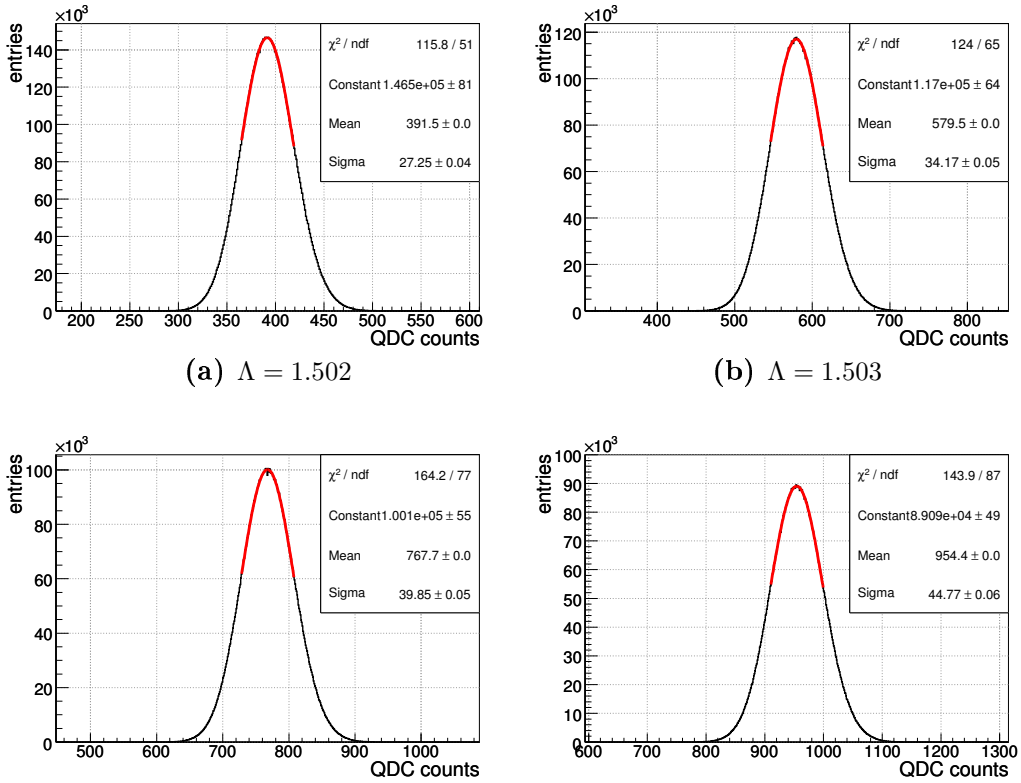


**(a)** $\Lambda = 1.502$ **(b)** $\Lambda = 1.503$

**(c)** $\Lambda = 1.501$ **(d)** $\Lambda = 1.499$

***Figure 10.2.:*** *Example of Gaussian fit method: The fits show good convergence. The fitted parameters and $\chi^2$/ndf can be found in the legends. The correlation $\Lambda$ between the Gaussian's width $\sigma$ and mean $Q_{QDC}$ is shown below the plot: $\Lambda = \sigma/\sqrt{Q_{QDC} - P}$, with the dark current $P = 62.5$ QDC counts.*

Again, as with the Multi-Poisson method, similarly good $\chi^2$/ndf ratios have been achieved. Four fits are shown as an example in figure 10.2. The same data set is used as in figure 10.1. Although the data are well described by a Gaussian function in a narrow interval around the peak position, the underlying Poisson statistics can be observed. Beneath the four histograms of figure 10.2 the correlation $\Lambda$ between the Gaussian's width $\sigma$ and mean $Q_{\mathrm{QDC}}$ is given. It is defined as

$$\Lambda = \frac{\sigma}{\sqrt{Q_{\mathrm{QDC}} - P}} \tag{10.4}$$

The photodetector's dark current $P$ has been measured separately to be $P = 62.5$ QDC counts. The values of $\Lambda$ are almost the same for all four measurements. This corresponds to the width of a Poisson distribution with mean $N$ scaling with $\sqrt{N}$.

### Comparison of both models

The parameters of interest are the number of photoelectrons in the Multi-Poisson model, and the output charge in the Gaussian case, i.e. the mean of the distribution. The relative statistical errors on these parameters are around $10^{-4}$ when using the Multi-Poisson fit method. In case of Gaussian fitting they are below $5 \cdot 10^{-5}$ in the vast majority of cases. A further advantage of the Gaussian approach are a robust and fast fit routine that is not dependent on well-tuned initial conditions.

The Gaussian Model has been used for the fitting of the recorded photodetector spectra in all the different measurements described below.

The results obtained for the photodetector nonlinearity differ slightly depending on whether either the Multi-Poisson or the Gaussian method was used for fitting the photodetector spectrum. This is interpreted as a systematic uncertainty of the analysis. A detailed description can be found in section 10.3.2 on page 127.

## 10.2. Optical Filters

At first glance, the easiest and most reproducible way to control the amount of light on the photocathode is the use of optical filters. Light, from an LED for example, is attenuated and guided to the photodetector. This is repeated with different filters, and the photodetector's response to different amounts of light is recorded. The photodetector's linearity can thus be measured to a level corresponding to the precision of knowledge of the filters' transmission coefficient.

For this analysis a set of five optical filters[1] was available. Before using them in photodetector linearity measurements, they were calibrated at *Laser Zentrum Hannover (LZH)*[2].

### 10.2.1. Filter Calibration

A spectrometric measurement of the filters' transmission coefficient in the range between 200 nm and 2000 nm with a step size of 1 nm was performed at the LZH. The spectrometer used was a *Perkin Elmer Lambda 900*. The accuracy of measurements as stated by the LZH can be found in table 10.1 on the following page.

For filters 2, 3, and 4 three series of measurements have been performed over the entire spectral range, whereas for filter 8 and 10 only two and one series have been measured, respectively. Figure 10.3(a) shows the transmission coefficient versus the wavelength. The peak wavelength of the LED used in this thesis' measurements ($\lambda = 470\,\mathrm{nm}$) is marked by a vertical black line. The root mean square of the different measurements for filters 2, 3, and 4 was compared to the relative uncertainty cited by LZH of 0.08 % (see table 10.1 on the next page). The results are shown in figure 10.3(b).

[1] in the following referred to by *filters number 2, 3, 4, 8, and 10*

[2] `http://www.laser-zentrum-hannover.de`

| | |
|---|---|
| wavelength accuracy | $< 0.08\,\text{nm}$ (UV/VIS)<br>$< 0.32\,\text{nm}$ (NIR) |
| wavelength reproducibility | $< 0.02\,\text{nm}$ (UV/VIS)<br>$< 0.08\,\text{nm}$ (NIR) |
| relative photometric accuracy | $\pm 0.08\,\%$ |

***Table 10.1.:*** *Accuracy of transmission coefficient measurements of optical filters, performed at LZH.* *(UV: ultraviolet, VIS: visual, NIR: near infrared)*

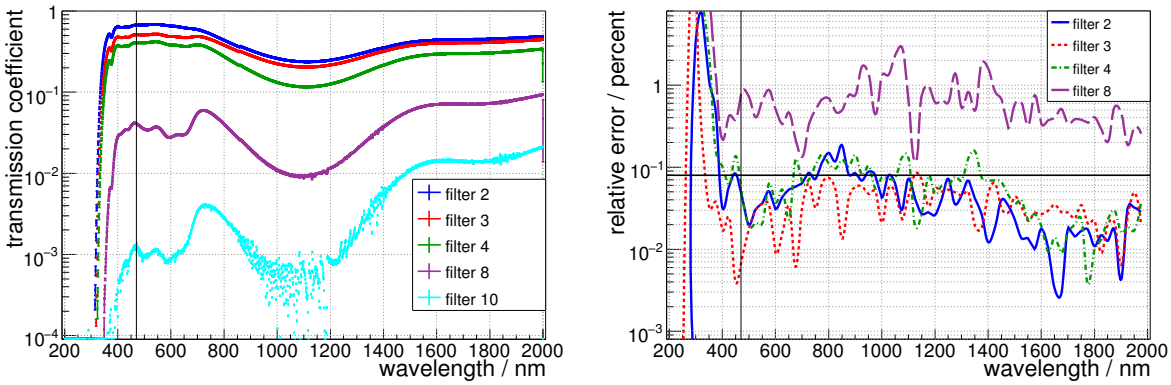


**(a)** recorded distributions **(b)** relative error

***Figure 10.3.:*** *Filter transmission coefficients as measured by LZH. The vertical black line denotes the peak wavelength of the LED used in this thesis' measurements ($\lambda = 470\,\text{nm}$).*
*(a) the recorded distributions of transmission coefficients for five different optical filters.*
*(b) root mean square for four of these measurements compared to the measurements' relative uncertainty of* $0.08\,\%$ *cited by LZH (marked by the horizontal line).*

For filters 2, 3, and 4 the difference between single measurements seems to reflect the level of uncertainty as cited by LZH. For filter 8, however, the deviations between both measurements is considerably larger than $0.08\,\%$ over the entire spectral range. For further calculations, the error attributed to the graphs of figure 10.3(a) is set to the root mean square of the initial measurements, but is at least $0.08\,\%$. For filter 10, for which only one single series of measurements was performed, an error of $0.08\,\%$ is assumed.

The LED used in these measurements does not emit light at a single wavelength. According to the manufacturer's datasheet [81], the emission spectrum follows a Gaussian distribution with a peak wavelength at $\lambda_{\text{peak}} = 470\,\text{nm}$ and a full-width-at-half-maximum of $\text{FWHM} = 35\,\text{nm}$. A graphical representation of emission spectrum is dis-

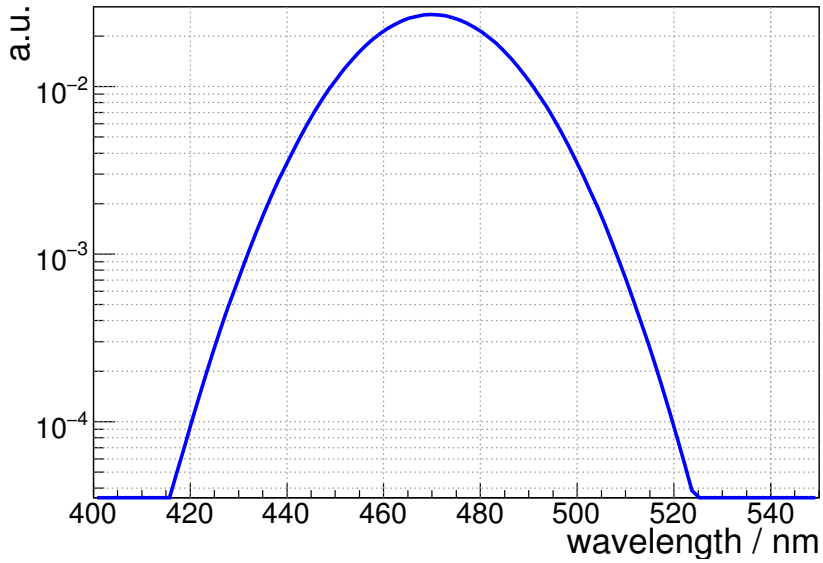


***Figure 10.4.:*** *The LED's emission spectrum as reconstructed from the parameters found in the datasheet [81]. The peak wavelength is* $\lambda_{peak} = 470\,\mathrm{nm}$.

played in figure 10.4. In order to correctly calculate the filters' transmission coefficients it is also necessary to take into account the quantum efficiency of the photodetector. The quantum efficiency has been extracted from a plot in the photodetector's data sheet [82]. It has been parametrized by an eighth order polynomial in a wavelength interval between 300 and 600 nm, in order to cover the LED's spectral range. A plot can be found in figure 10.5 on the following page.

The filter's transmission coefficients for the test setup were determined using a Monte Carlo approach: $10^7$ photons were generated according to the LED's emission spectrum (figure 10.4). Then for each photon a Monte Carlo experiment was performed to determine whether the photon passes a given filter. The wavelength dependent transmission spectra recorded by LZH were used for this (figure 10.3(a)). The procedure was repeated for all photons passing the filter, this time using the parametrization of the quantum efficiency (figure 10.5). This cycle was repeated ten times for every filter and the case of no filter. Figure 10.6 on page 123 shows the spectral distributions and total number of photons after each step, in this case for filter 2. For a given filter, the final number of photons equals the filter's transmission coefficient when normalized with the final number of photons without any filter.

In addition to this, a systematic shift of the transmission coefficient was studied: The transmission measurement from figure 10.3(a) was shifted up and down by its respective error. Another ten cycles were done each. The mean values of both the systematic cycles and the original simulation was compared to the root mean square from the latter. No significant difference could be observed. Obviously, systematic effects are still covered by the Monte Carlo statistics. It was decided that the accuracy

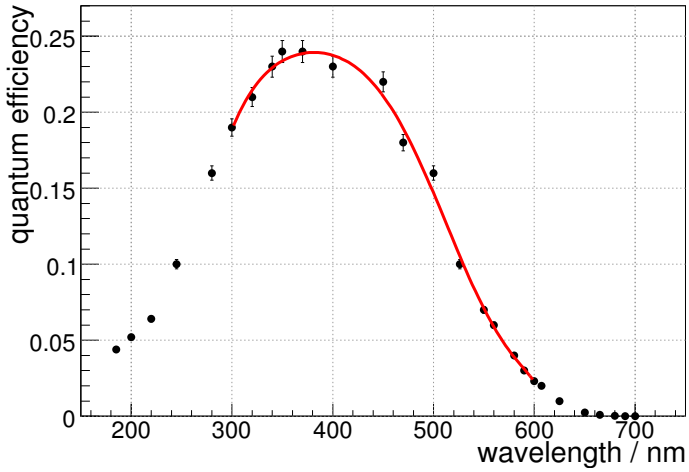


***Figure 10.5.:*** *Quantum efficiency of the Hamamatsu R5900 multi-anode photomultiplier, extracted from [82], and parametrized by an eighth order polynomial. The peak wavelength of the LED used for the measurements herein is* $\lambda_{peak} = 470\,\mathrm{nm}$.

of the method is sufficient, and thus, the mean of the ten cycles without systematic shifts are used as the transmission coefficient for this analysis' setup. The root mean square is used as an error attributed to these values.

Table 10.2 shows the final results for the transmission coefficients for the different optical filters. Since the testbox provides mounting for up to three filters (see section 9.1), the table additionally shows the transmission coefficients for the filter combinations used in later measurements.

| filters | transmission coefficient | absolute error |
|---|---|---|
| 2 | 0.66573 | $7.08 \cdot 10^{-4}$ |
| 3 | 0.50433 | $5.68 \cdot 10^{-4}$ |
| 4 | 0.40244 | $5.48 \cdot 10^{-4}$ |
| 8 | 0.03936 | $1.53 \cdot 10^{-4}$ |
| 10 | 0.00112 | $0.18 \cdot 10^{-4}$ |
| $2+3$ | 0.33575 | $5.20 \cdot 10^{-4}$ |
| $2+4$ | 0.26791 | $4.63 \cdot 10^{-4}$ |
| $3+4$ | 0.20296 | $3.59 \cdot 10^{-4}$ |
| $2+3+4$ | 0.13512 | $2.79 \cdot 10^{-4}$ |

***Table 10.2.:*** *Transmission coefficients of optical filters, taking into account the spectral range of the LED and the quantum efficiency of the photodetector used in this analysis.*

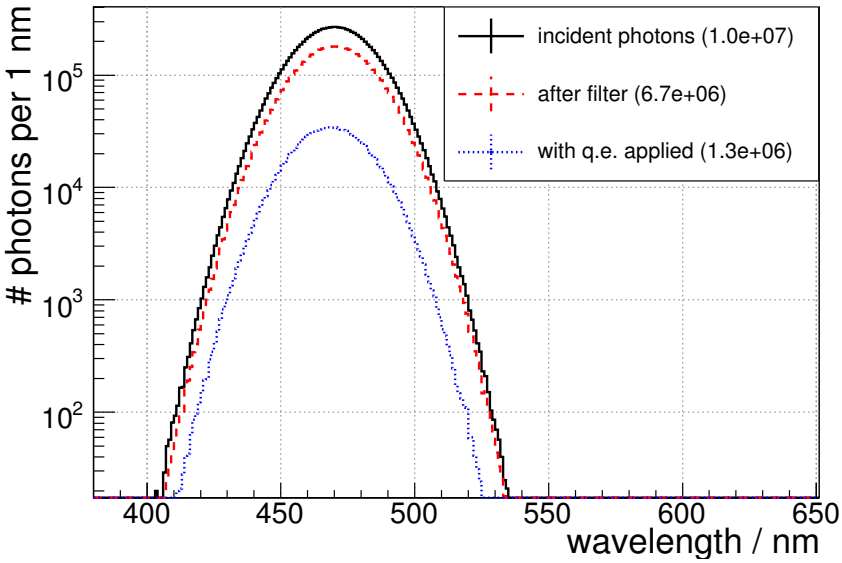


***Figure 10.6.:*** *Determination of filters' transmission coefficients by a Monte Carlo method. Shown are the spectral distributions of the incident (generated) photons (solid black histogram), the photons passing the filter (dashed red histogram), and the photons after applying the photodetector's quantum efficiency (dotted blue line). The total number of photons after each step is listed in the legend. The filter's transmission coefficient can be derived from the number of photons after the final step normalized with the final number of photons without any filter. This plot was done for filter 2.*

### 10.2.2. Photodetector Linearity Measurements

In order to measure the photodetector nonlinearity the following setup was used: The LED was pulsed with a frequency of $f = 10\,\mathrm{kHz}$, a pulse length of $t = 50\,\mathrm{ns}$, and a voltage of $U_{\mathrm{LED}} = -5\,\mathrm{V}$. The photodetector was operated at a high voltage of $U_{\mathrm{HV}} = -800\,\mathrm{V}$. For the QDC readout a gate of length $t_{\mathrm{gate}} = 200\,\mathrm{ns}$ was used. A total of eight measurements were performed with filters 2, 3, and 4, with all four combinations of these, and without any filter (see table 10.2 on the preceding page for the transmission coefficients). For each measurement $10^7$ LED pulses were recorded.

Figure 10.7 on the following page shows the results obtained with this method. The output charge from the photodetector's anode is plotted versus the transmission coefficients of different filter configurations (compare table 10.2). The errors in this figure are statistical errors resulting from the Gaussian fits to the recorded spectra. Due to the high statistics used ($10^7$ samples per point), the statistical errors are minute, and are shown as a red band in a separate histogram.

A straight line is fitted to the points in figure 10.7 on the next page. The relative deviation of the measured data points from this line then gives the integral nonlinearity

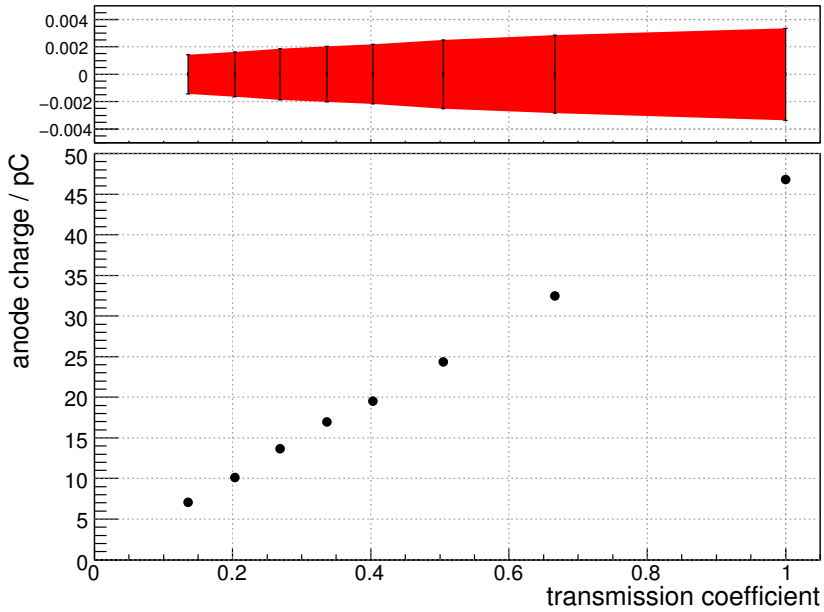


***Figure 10.7.:*** *Photodetector linearity measurement with optical filters: Anode charge of photodetector output for eight different filter configurations (compare table 10.2). The statistical errors are shown as a red band in a separate histogram.*

of the photodetector. The procedure has been performed using five and six points of figure 10.7. This is visualized in figure 10.8. The subfigures on the left-hand side show the fitted lines, those on the right-hand side display the obtained integral nonlinearity. The points' labels indicate which filter combination has been used for that particular measurement. Both the nonlinearity obtained using five (figure 10.8(b)) and six fit points (figure 10.8(d)) look similar. Analogous result have been observed using more or less points for the straight line fit.

The nonlinearity obtained with this filter method appears to be quite large. Relative deviations up to 2.5 % can be observed. This seems unreasonably large, especially when compared to measurements with different methods (see for example section 10.3). In addition to this, the fitted parameters of the straight line are not compatible with the case of no output charge at a transmission coefficient of 0. Including this physically sensible point in the fit procedure only worsened the results.

Furthermore, a systematic effect seems to be visible. The four measurements which *included* filter 2 all have positive nonlinearities while for the three measurements *without* filter 2 (considering only measurements using at least one filter) the nonlinearities are all below zero.

Possible sources of systematics errors have been taken into account. The same optical fiber has been used for all measurements. A sufficient warm-up time has been ensured for both the photodetector and the LED, and has been applied identically in all measurements.

Especially considering the systematic shift of all measurements including filter 2, this

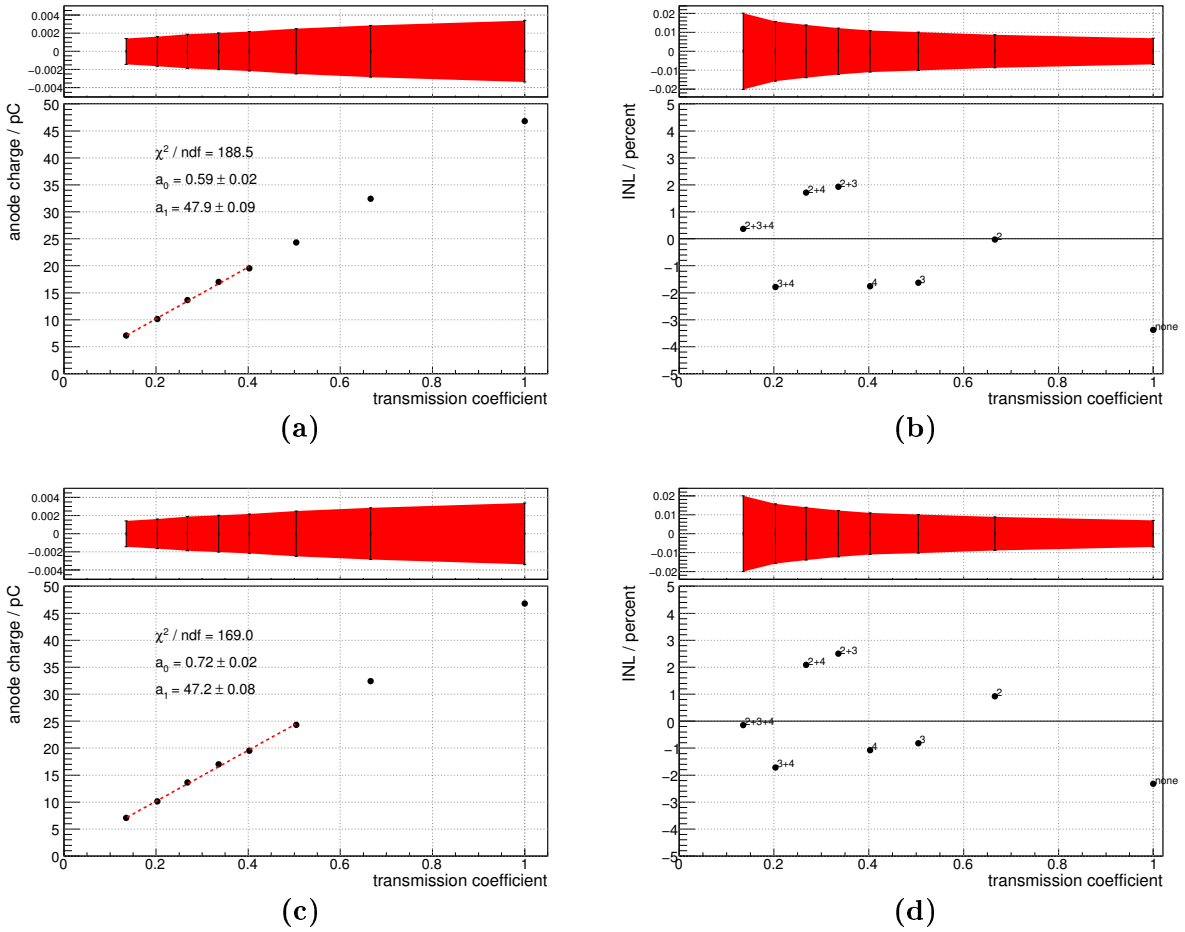


***Figure 10.8.:*** *Photodetector linearity measurement with optical filters: A straight line is fitted to the data using five (a) and six (b) points, respectively. The fitted parameters of the straight line are displayed in the plots. The relative deviation of the data from this line is the integral nonlinearity of the photodetector (b) and (d). The points' labels indicate which filter combination has been used for that particular measurement. Errors are shown as a red band in separate histograms.*

leads to the assumption that the precision of the filter calibration may be insufficient for the purposes of this analysis.

The error bars in figures 10.7 and 10.8 attributed to the measured transmission coefficients are basically resulting from the root mean square of separate calibration measurements (in $x$), and from the statistical errors of the fitting procedure (in $y$).

It was decided to discard this method to determine the photodetector nonlinearity for the time being. It is advisable to redo the filter calibration with special attention to systematic uncertainties.

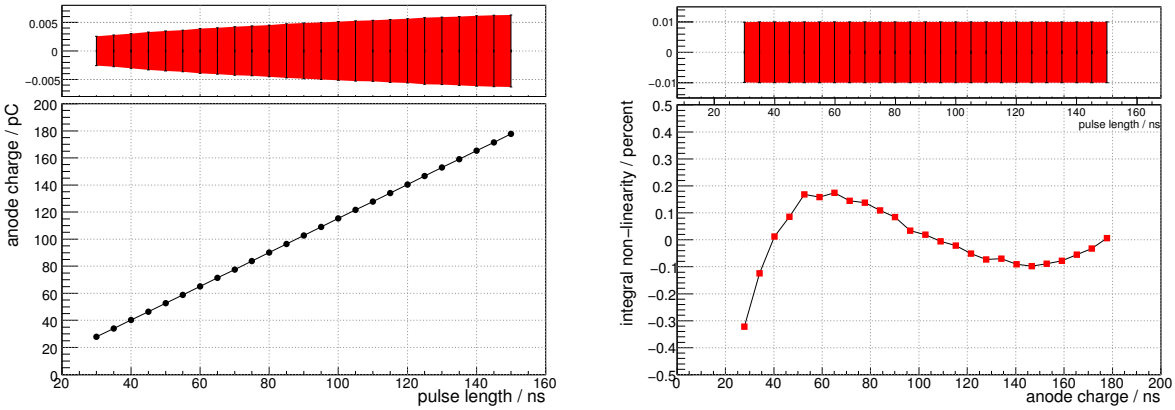


(a) (b)

***Figure 10.9.:*** *Pulse length measurement: (a) the recorded anode charge for different LED pulse lengths. Only statistical errors are applied.*
*(b) integral nonlinearity for these data points. The pulse lengths can be found on the upper, the corresponding anode charge on the lower horizontal axis. The statistical errors are shown in separate plots as a red band.*

## 10.3. Pulse Length

In order to ensure a linear variation of the amount of light on the photocathode, a second method has been envisioned. The LED is operated with a rectangular signal from the function generator. The length of the pulse is varied. With the minimal pulse length still considerably larger than the rise and fall time of the LED, this procedure provides a linear variation of the incident light. It has to be taken into account that a large change of the length of the light pulses may also affect the photodetector's linearity. The electron shower traversing the dynode structure can partially shield the potential differences between the dynode stages, thus altering the voltage configuration of the device. In order to keep this effect minimal it has been decided to vary the pulse length only by a factor of five. If this effect still had a considerable contribution to the nonlinearity measurements, it would become visible in the comparisons of the results acquired with this method and those determined by the E158 method, which does not rely on pulse length variations (cf. section 10.6 on page 140).

### 10.3.1. Photodetector Linearity Measurements

For these measurements the LED was pulsed at a frequency of $f = 10\,\mathrm{kHz}$ and with a voltage of $U_{\mathrm{LED}} = -5\,\mathrm{V}$. The pulse length $t$ was varied in 5 ns steps between 30 ns and 150 ns. The QDC was read out during a gate of 200 ns duration. The photodetector was operated at a supply voltage of $U_{\mathrm{HV}} = -800\,\mathrm{V}$. For each measurement $10^7$ LED pulses were recorded.

Subfigure (a) of figure 10.9 shows the results recorded with this method. The charge

collected on the photodetector's anode during one gate is plotted against the different pulse lengths. The charge was acquired from the photodetector spectrum recorded by the QDC using the Gaussian fit method (see section 10.1.1). No systematic, only the statistical uncertainties are applied to this plot. They are very small and shown in a separate plot as a red band. The treatment of uncertainties is described in the next section. By fitting a straight line to these data points, the integral nonlinearity can be calculated as the relative deviation of the measured data from this line. The results can be seen in figure 10.9(b). In this plot the integral nonlinearity is plotted against the anode charge. The corresponding LED pulse length is shown in the upper horizontal axis. The range of anode charge used in these measurements is considerably larger than the one used in the filter measurements. In the latter the charge was varied between 5 and 45 pC, approximately. In these measurements the anode charge is in the range of 30 to 180 pC.

Subfigure (a) proves that the photodetector has a linear behavior on a larger scale, as opposed to the dubious results obtained by the optical filters method (see figure 10.7 on page 124). A nonlinearity at the subpercent level can clearly be observed in subfigure (b). However, in order to determine the relevance of this, an estimate of systematic uncertainties has to be done first.

## 10.3.2. Systematic Uncertainties

In figure 10.9 no systematic uncertainties are plotted. Only the statistical uncertainties on the anode charge, derived from the fitting process, are displayed. Two sources of uncertainty were estimated: the accuracy of the function generator's pulse length, and a general systematic uncertainty on the fitting procedure.

### Accuracy of pulse length

The function generator allows a very fine adjustment of pulse lengths orders of magnitude lower than the typical pulse lengths used in this analysis. However, one cannot assume that this actually represents the accuracy of the device. In order to get a more realistic estimate, a $\chi^2$-test has been used. Mathematically the center part of the measured integral nonlinearity (figure 10.9(b)) can be parametrized by a straight line. If the errors on the data are of the correct order of magnitude, and assuming the pulse length is the only error source, the reduced $\chi^2$ should be about 1. Figure 10.11 shows three iteration steps in the process described below.

First of all, the data recorded with the pulse length measurement is plotted with the pulse length on the vertical and the anode charge on the horizontal axis. In that way the error on the pulse length is propagated to the vertical axis of the integral nonlinearity plot, so that the $\chi^2$-test can be applied.

Then an initial relative error of $10^{-3}$ is assumed for the pulse length (in the distributions on the left-hand side of figure 10.11). This initial error encompasses both

systematic and statistical uncertainties from the fitting procedure. However, the latter are so small ($\mathcal{O}(10^{-5})$) that they can safely be neglected.

A straight line is fitted to the graph, and the (relative) deviation of the data from the line is calculated, representing the integral nonlinearity of the photodetector. In the central part, this distribution can be described by a straight line. Nine points are used for the following procedure, representing a range from about 80 to 130 pC in terms of anode charge, or 70 to 110 ns in terms of pulse length. A straight line is fitted to these nine points. The $\chi^2$ is calculated for these points with respect to that line.

In case of the assumed error of $10^{-3}$ the $\chi^2$ is close to zero, because this error is too large by far. So the error is set to the half of its value, and the whole procedure is redone: A line is fitted to the measured data, the linearity is calculated, and the $\chi^2$ of the nine points is calculated with respect to a fitted straight line. This iteration is repeated several times.

Three iteration steps are shown in figure 10.10 on the facing page. The plots on the left-hand side (subfigures (a), (c), and (e)) show the LED pulse length versus the measured anode charge. The errors are shown as a red band in seaperate plots on top. The integral nonlinearity (INL) determined from this data can be found in the plots on the right-hand side of figure 10.10 (subfigures (b), (d), and (f)). The straight line fitted to the central linear part of the integral nonlinearity is displayed in red. The reduced $\chi^2$ of this line with respect to the data points is noted in each plot.

If the behavior of the integral nonlinearity in the central region is linear, one expects the reduced $\chi^2$ to be about 1 once the correct error estimate is applied.

In figure 10.11 on page 130 the reduced $\chi^2$ is plotted versus the (inverse) relative error on the pulse length $t$. The expected quadratic behavior can be observed. The reduced $\chi^2$ is 1 for a relative pulse length error of about $\Delta t/t = 10^{-4}$. This is assumed to be the uncertainty on the pulse length of the function generator.

### Fitting process

A second source of systematic uncertainty is analyzed. As described before (in section 10.1.1 on page 119), there is a systematic difference in the results for the integral nonlinearity depending on whether the data has been fitted with the Multi-Poisson or the Gaussian model. This is treated as a systematic uncertainty on the results acquired for the nonlinearity. In order to quantify this, seven series of pulse length measurements have been recorded. They have been analyzed using both the Multi-Poisson and the Gaussian fitting model.

The results can be seen in figure 10.12 on page 131. The difference between the integral nonlinearities calculated with both fitting models is plotted as red circles in subfigures (a) to (g) for seven series of pulse length measurements. In subfigure (h) the root mean square of results of the same seven measurements is shown for every pulse length. Green squares represent the Multi-Poisson fit method, whereas blue circles denote the Gaussian fit model. The latter two graphs are an order of magnitude lower than graphs in subfigures (a) - (g) for most pulse lengths. This means the differences

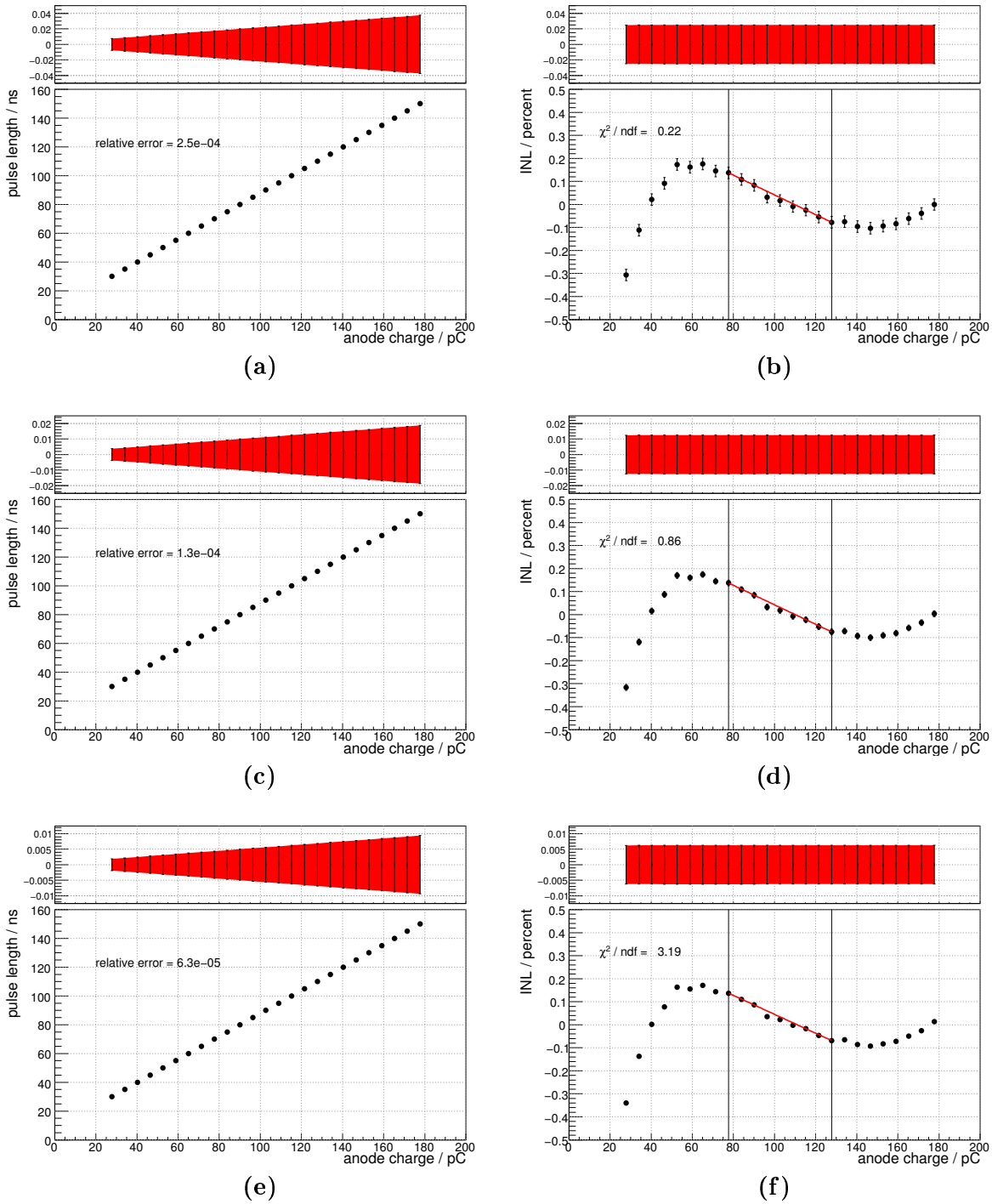


***Figure 10.10.:*** *Three iteration steps of the $\chi^2$ estimation of pulse length errors.*
*(a), (c), (e): measured anode charge for different pulse lengths.*
*(b), (d), (f): derived INL and the straight line fitted to the central part.*
*(INL: integral nonlinearity)*

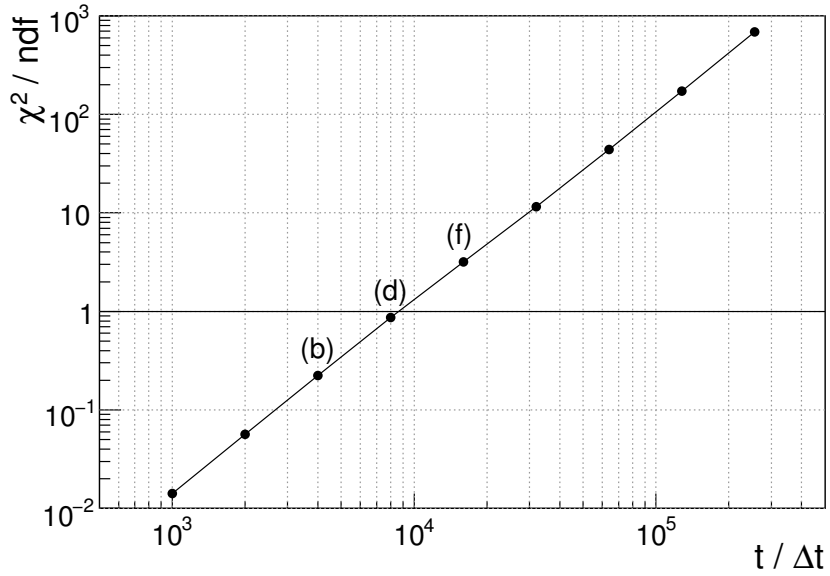


***Figure 10.11.:*** *Results of the $\chi^2$ estimation of pulse length errors. The reduced $\chi^2$ from all iteration steps is plotted versus the (inverse) relative error on the pulse length $t$. The indices refer to the corresponding subfigures in figure 10.10. From this plot, the relative error is determined to be $\Delta t/t = 10^{-4}$.*

within each fit method can be ignored against the systematic difference between both methods.

The difference between the Gaussian and Multi-Poisson fitting procedure has a similar shape in all seven series of measurements (figure 10.12(a)-(g)). Most prominent feature is a dip in the center where it drops more than one order of magnitude below its highest values, in cases even up to two orders of magnitude. Around this point (at an anode charge of $\approx 100\,\mathrm{pC}$) the integral nonlinearity has a zero crossing (cf. figure 10.9). Obviously, this feature is similarily reproduced with both fitting models.

In order to estimate a reasonable value for the mean difference between the Gaussian and the Multi-Poisson fit model, the difference has been averaged over the seven series of measurements for each pulse length.

This is shown in figure 10.13 on page 132. The red points represent the mean of the difference, while the red band represents the root mean square of the results for a given pulse length. A relative systematic uncertainty of $5 \cdot 10^{-4}$ appears reasonable. A black horizontal line in figure 10.13(a) denotes this value. Only three out of 25 measurements show differences significantly larger than that.

The uncertainty of the pulse length of $10^{-4}$ is combined with that of the fit method, and a total systematic uncertainty of $5.1 \cdot 10^{-4}$ is assumed for the measured data.

In the scope of the $\chi^2$ test performed for the pulse length error, this would, of course, mean $\chi^2 \ll \mathrm{ndf}$. However, this argument is not applicable here, since the differences due to the fit method cause shifts in the same direction.

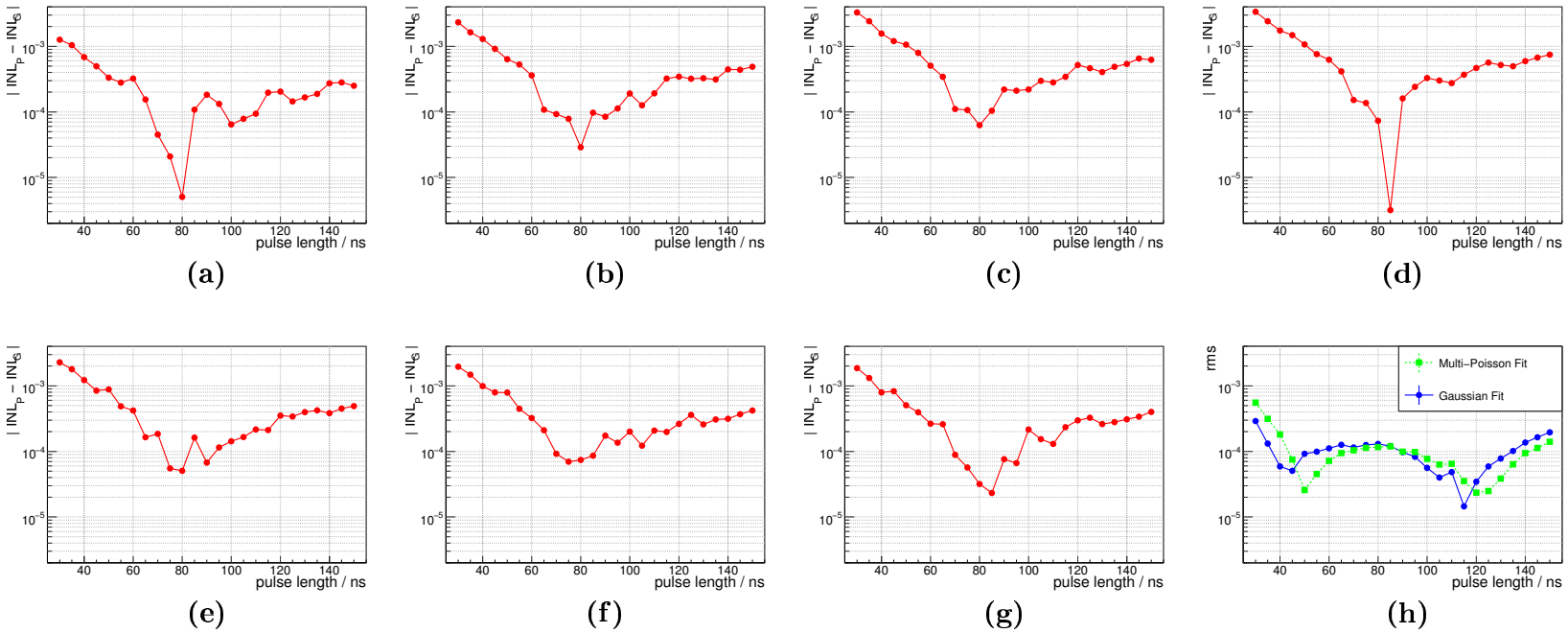


***Figure 10.12.:*** *Estimation of systematic uncertainties due to fitting method:*
*(a)-(g): Difference of integral nonlinearity obtained using Gaussian and Multi-Poisson fit model for seven series of pulse length measurements.*
*(h): Root mean square of results versus LED pulse length obtained by Multi-Poisson (green squares) and Gaussian (blue circles) fit method.*

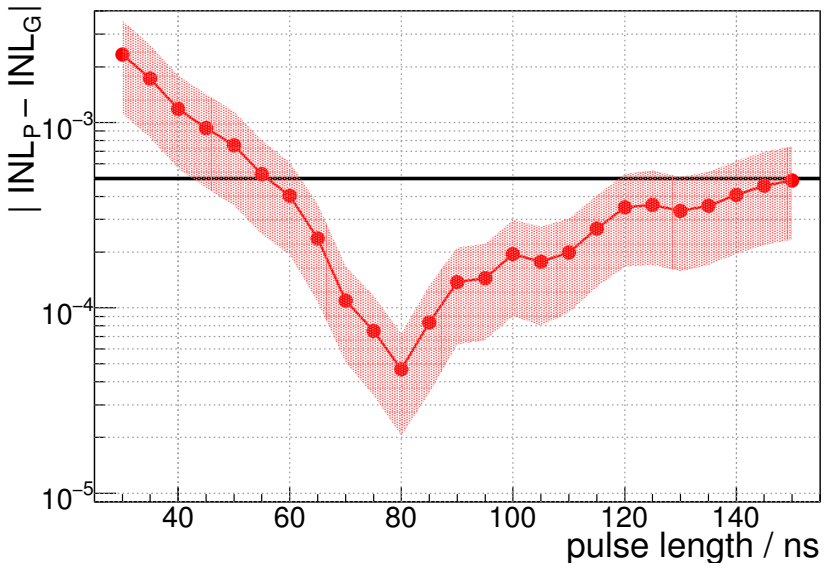


***Figure 10.13.:*** *Difference between the integral nonlinearity (INL) obtained using the Gaussian and the Multi-Poisson approach, plotted versus the LED pulse length. The points mark the average values of seven series of pulse length measurements. The red band represents the root mean square of results. The horizontal line represents an uncertainty of* $5 \cdot 10^{-4}$.

### 10.3.3. Results

The combined systematic uncertainty is now applied to the results shown in figure 10.9 on page 126. This is displayed in figure 10.14 on the facing page. The measured anode charge is plotted against the LED pulse length. The error bars are shown as a red band on a separate plot on top. A large scale linear behavior is visible. However, photodetector nonlinearities are expected to be below one percent, which is not visible in this diagram. A straight line is fitted to the data points. Then the relative deviation of the measured anode charge from this straight line is calculated for each pulse length. This represents the integral nonlinearity of the photodetector.

The result is shown in figure 10.15 on the next page. The nonlinearity is plotted against the recorded anode charge (lower horizontal axis). The upper horizontal axis shows the corresponding LED pulse length. The blue band represents the full uncertainties, combining the statistical error from the fitting of the recorded QDC spectra, and the systematic uncertainty of the measurement, as determined in section 10.3.2. The nonlinearity of the photodetector in the subpercent range can clearly be observed within the errors. The graph has both a maximum and a minimum and a turning point in the center. A sharp rise is observed for small anode charges and short pulse lengths. This may hint to effects caused by an LED rise time that is larger than expected. However, no information about this property could be acquired. Future analyses on

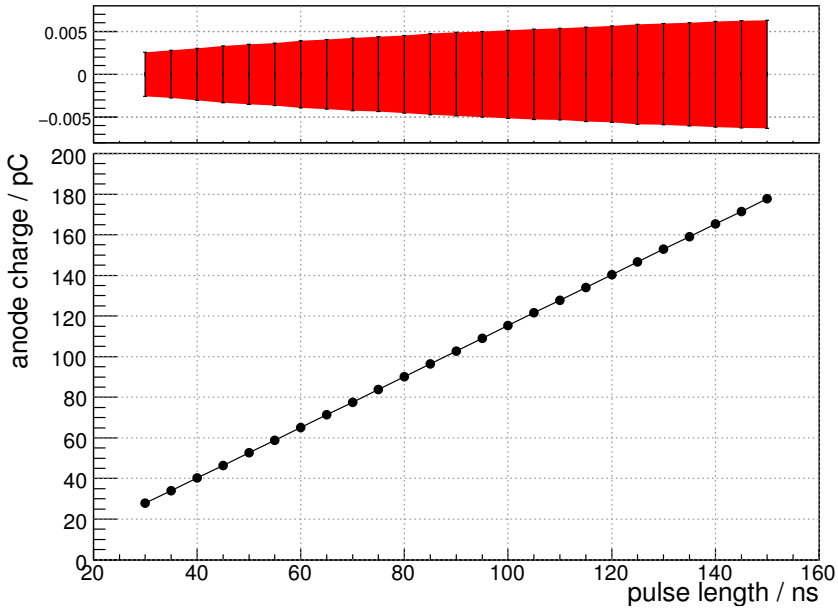


***Figure 10.14.:*** *Pulse length measurement: Anode charge versus pulse length with full systematic and statistical uncertainties applied. The error bars are shown as a red band on a separate plot on a different scale.*

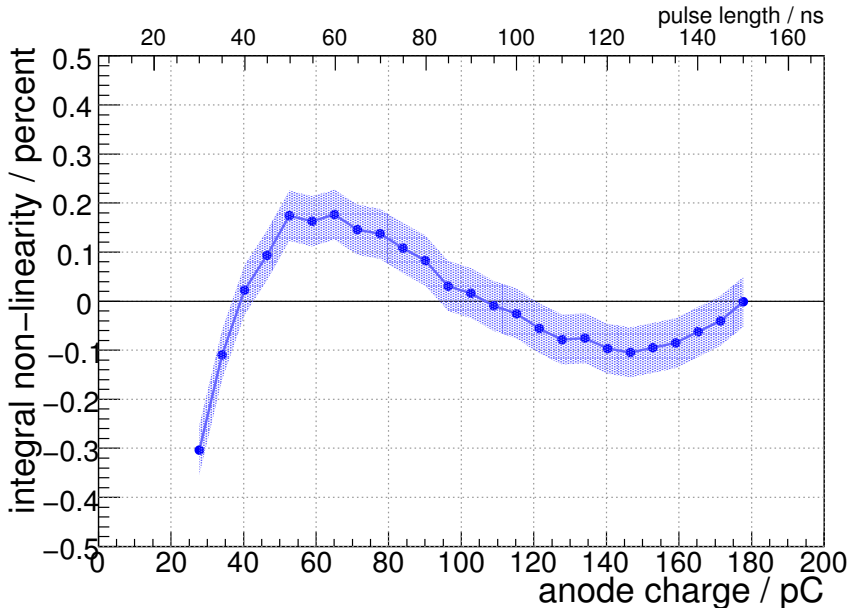


***Figure 10.15.:*** *Pulse length measurement: Integral nonlinearity of the photodetector. The blue band represents the full statistical and systematic uncertainties.*

this topic should further investigate this behavior of the nonlinearity.

Following the convention discussed in 8.3 the integral nonlinearity of the investigated

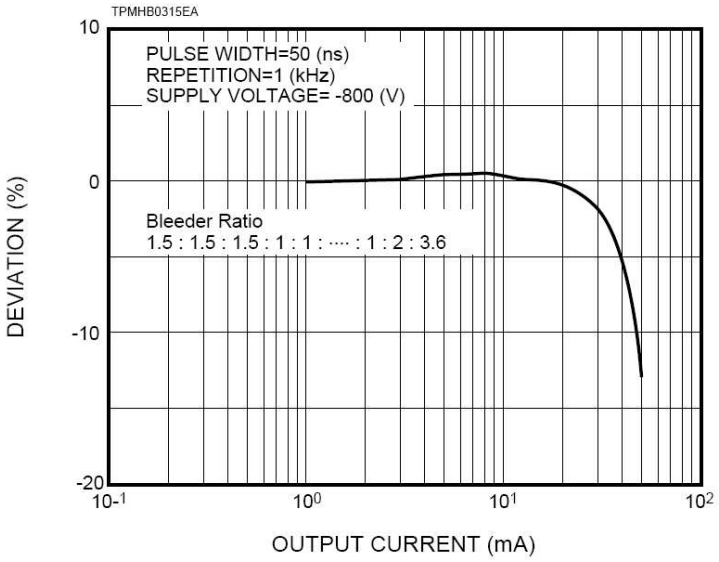


***Figure 10.16.:*** *Information about the nonlinearity of the photodetector under test as provided by the manufacturer, from [82]. The anode charges considered in this analysis correspond to average currents of up to* $2\,\mu$A.

photodetector has been measured to be

$$\mathrm{INL} = (0.5 \pm 0.05)\% \tag{10.5}$$

The measurement of a photodetector's nonlinearity in the subpercent range is an achievement of this analysis. For comparison figure 10.16 shows the information of the photodetector under test as provided by the manufacturer, Hamamatsu, taken from the data sheet [82]. For comparison with the manufacturer's figure the anode charges recorded in this analysis are transformed into average currents by the following estimate: Anode charges $Q_A$ of up to 200 pC have been read out at a rate of $f = 10\,\mathrm{kHz}$, resulting in an average anode current of $\bar{I} = Q_A \cdot f = 2\,\mu\mathrm{A}$. This current domain is three orders of magnitude below the information provided by the manufacturer.

In order to devise and test methods to measure the photodetector nonlinearity only a limited charge range has been considered in this analysis. Of course, in a polarization measurement at a running ILC experiment, a much larger dynamic range has to be covered. From one up to one thousand electrons are expected per photodetector during ILC polarization measurements. However, the methods developed in this thesis can easily be expanded to cover different ranges. By gradually increasing the amplitude voltage used to operate the LED, the same pulse length method described herein can be used to cover higher charge ranges.

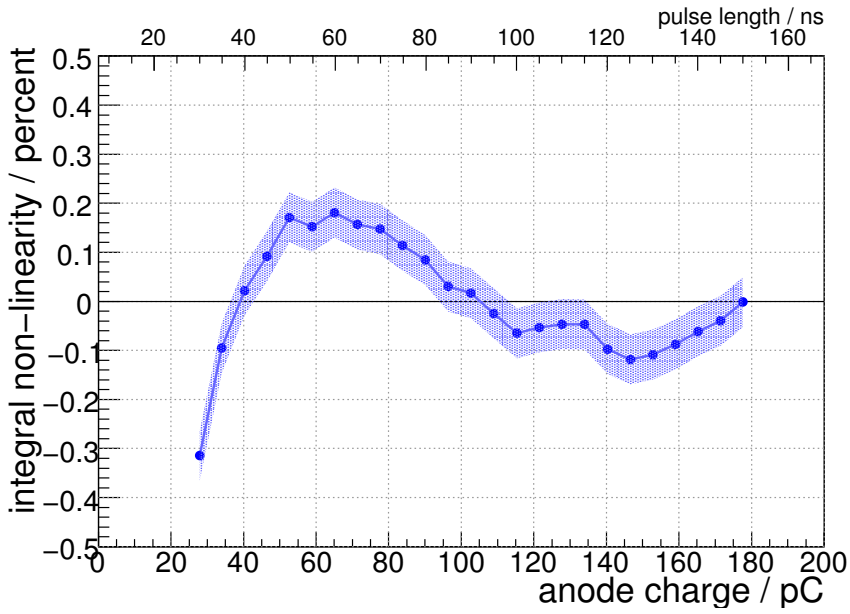


***Figure 10.17.:*** *Pulse length measurement: Integral nonlinearity of the photodetector, corrected for QDC nonlinearity. The blue band represents the full statistical and systematic uncertainties.*

### 10.3.4. Application of QDC Nonlinearity

The results recorded with the pulse length measurement are corrected for the QDC nonlinearity. The determination of the QDC nonlinearity is described in section 9.5.1 on page 107. The *differential* nonlinearity of the QDC is used for this (see figure 9.6), which is equivalent to the actual bit sizes of the QDC. In the recorded photodetector spectra each histogram bin is weighted with the inverse of the differential nonlinearity of the corresponding QDC bit. Thus, the content of a QDC bit that has been determined to be larger than one least significant bit is scaled down and vice versa. Once this procedure has been applied to all QDC bits, the photodetector's integral nonlinearity is calculated again.

The results can be found in figure 10.17. This figure refers to the same measurement as figure 10.15 on page 133, except that the QDC nonlinearity has been corrected for. Both figures are very similar. The major difference is a slight shift between 120 and 140 pC. This corresponds to the large dip in the differential QDC nonlinearity at around 600 QDC counts (see figure 9.6 on page 109). The subpercent nonlinearity of the photodetector is still clearly visible, and the observations made in the previous section are still fully applicable.

## 10.4. Double Pulse

While the methods described so far are sensitive to the integral nonlinearity of the photodetector, two further methods have been devised that are sensitive to the differential nonlinearity. They will be introduced in this and the following chapter.

The *double pulse method*, described in this section makes use of a second LED of the same type installed beside the one used so far. The first LED is pulsed in the same way as in the pulse length method (see section 10.3). The second LED is operated with a fixed, very short pulse. The differential nonlinearity is acquired by comparing the signal when both LEDs are lit simultaneously and when only the first LED is used. By varying the length of the first pulse, the DNL can be measured at different operating points.

The two LEDs were pulsed by the two output channels of the function generator, which were synchronized to each other and operated at a frequency of $f = 10\,\mathrm{kHz}$. The first LED was powered by a rectangular pulse with an amplitude of $U_1 = -5\,\mathrm{V}$. The pulse length was varied between 50 and 150 ns in 5 ns steps. For the second LED the pulse length was fixed to 25 ns, and the amplitude was $U_2 = -2\,\mathrm{V}$. There was a very short delay of 0.05 ns between both channels. The gate for the QDC read-out was generated by the trigger output of the function generator. Since this is using TTL[3] it had to be fed into several NIM modules. First it was inverted, and then processed by a gate generator. The resulting gate had a width of 300 ns.

After a warm-up time of 5 hours for the photodetector and 3 hours for both LEDs a dark current measurement was done. Then the first LED was switched on with a pulse length of 50 ns, and $10^7$ pulses were recorded. The second LED's short pulse was turned on as well, and another $10^7$ samples were acquired. Then the second LED was switched off, the first LED's pulse length was increased and the procedure was repeated.

### 10.4.1. Results

Figure 10.18 on the facing page shows the data acquired by the double pulse method. The anode charge is plotted against the pulse length of the first LED. Of course, for the measurements with both LEDs turned on not one specific pulse length can be given. In this plot these measurements have been attributed a pulse length of 1 ns more than the corresponding single pulse measurement.

In order to acquire the differential nonlinearity, the effect of adding the second LED pulse is calculated. This can be seen in figure 10.19 on the next page. Subfigure (a) shows the difference $\Delta Q$ in the output anode charge between the measurements with both LEDs on and the ones with only the first LED turned on. This is basically the difference within each of the pairs of points in figure 10.18. The difference $\Delta Q$ is plotted against the anode charge acquired from the first LED's pulse. Since the small LED pulse is not altered one would expect a uniform distribution for a perfectly linear

[3] Transistor transistor logic: a type of digital logic gate

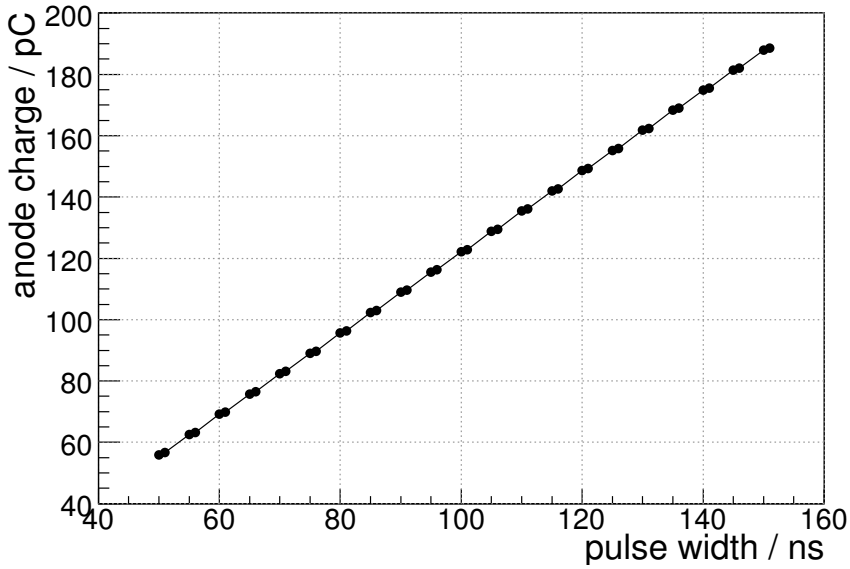


***Figure 10.18.:*** *Double pulse measurement: Anode charge versus pulse length. The left one of each pair of points represents the measurement with only the large pulse (first LED) on, the right one the measurement with both LEDs switched on.*

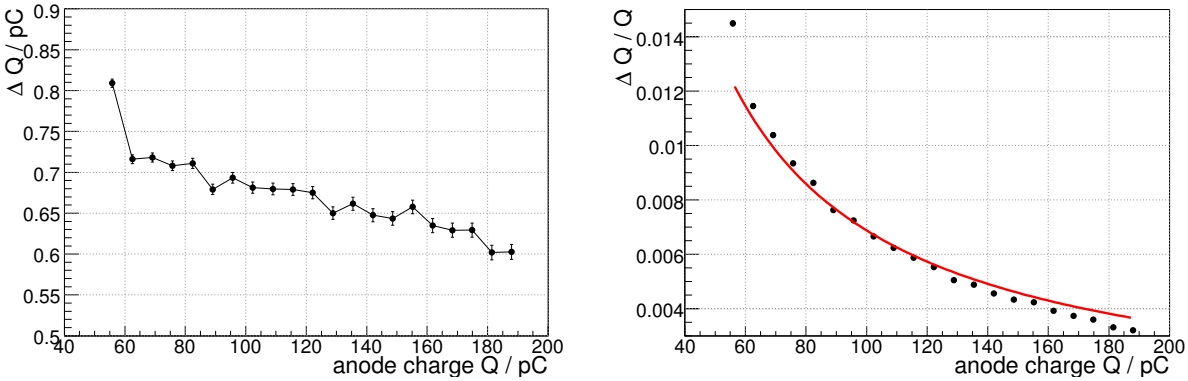


**(a)** **(b)**

***Figure 10.19.:*** *Double pulse measurement: Difference between double and single pulse signals plotted against the anode charge recorded in the corresponding single pulse measurement.*
*(a) The difference $\Delta Q$ is shown in units of pC.*
*(b) The difference is divided by the respective single pulse anode charge. A parametrization is fitted to the data points.*

photodetector. That is not the case. A negative slope is clearly visible.

In figure 10.19(b) the data of subfigure (a) are divided by the respective anode charge

from the first LED pulse. If $Q$ denotes the charge from the large first LED pulse and $q$ the charge from the small pulse, the variable plotted in figure 10.19(b) is

$$\Delta Q/Q = (Q + q - Q)/Q = q/Q \tag{10.6}$$

A parametrization of the form

$$f(Q) = \frac{p_0}{Q} \tag{10.7}$$

was fitted to the data of subfigure (b). Equation 10.7 represents a perfectly linear photodetector, for which the response to a small but constant change in the incident light is independent of the working point $Q$. As in subfigure (a) large deviations from the behavior of an ideal photodetector can be observed.

The ratio of the actual data and this parametrization then yields the differential nonlinearity. The results are shown in figure 10.20 on the facing page. Very large nonlinearities of more than 10% can be observed. In comparison to the very good linear behavior determined with the pulse length measurement (cf. section 10.3), the measured differential nonlinearity seems implausible. It can be assumed that the recorded data was biased. Several possible reasons can be excluded. It was made sure an identical setup was used for every single measurement. Both the photodetector and the LED were warmed up prior to data taking. The warm-up time was the same for every measurement. The linear slope of the recorded DNL seems suspicious, and hints at a systematic effect. This may be some saturation effect. It is, however, unclear from which source. The charge range of this method is similar to that of the pulse length method, for which no large deviations from linearity were observed. Some slack joint or other technical explanation can most likely be excluded since successful measurements have been performed with the same equipment. In contrast to the pulse length method, this method made use of the second LED installed in the external LED box. Problems with the coupling of this second LED to the optical fibers can most probably also be excluded considering the successful measurements with the E158 method. This method also makes use of the second LED, and will be introduced in 10.5.

Ultimately, it was not possible to identify the problems with this method. This should be investigated further in future analyses on this topic. For the further considerations in this thesis, the double pulse method has been discarded.

## 10.5. E158 Method

The second method fit to measure the differential nonlinearity of the photodetector was inspired by a technical note of the E158 collaboration [83]. The method described therein has been slightly altered in order to be realizable with the equipment available for this thesis.

The method makes use of two LEDs. However, in contrast to the other methods described so far, both are operated with fixed pulses. The differential nonlinearity can

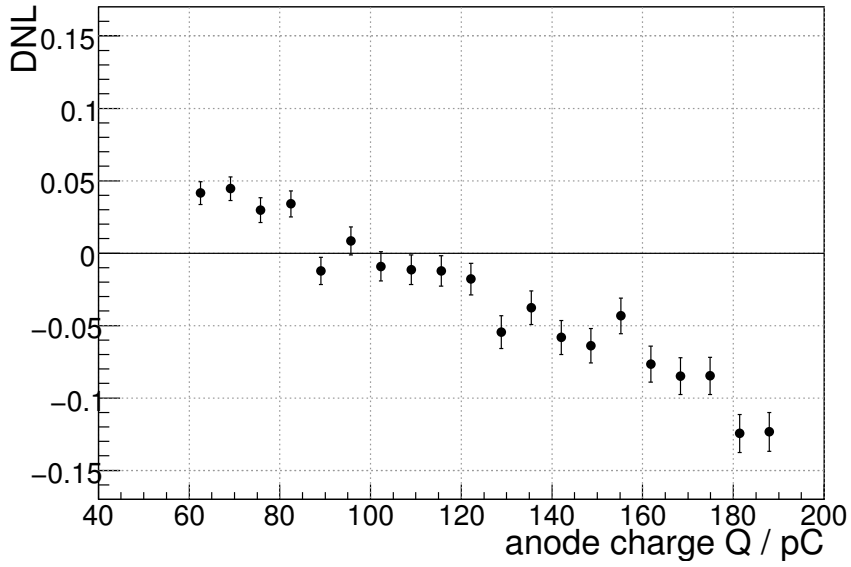


***Figure 10.20.:*** *Double pulse measurement: Differential nonlinearity.*

be measured by the ratio of signals acquired when pulsing both LEDs at the same time, and the sum of two measurements with both LEDs pulsed separately. By attenuating the signal with optical filters, the differential nonlinearity can be measured at different light intensities and anode charges.

Both LEDs were pulsed with rectangular signals at a frequency of $f = 10\,\mathrm{kHz}$. The amplitude of the supply voltage was $U = -5\,\mathrm{V}$. The pulse lengths were $t_1 = 50\,\mathrm{ns}$ and $t_2 = 150\,\mathrm{ns}$. This resulted in QDC signals with a ratio of $Q_1/Q_2 \approx 1/4$. This ratio is not $1/3$ as may intuitively be assumed from the ratio of pulse lengths due to differences in the LED performances, or in the LED's optical coupling to the fibers.

In order to measure the differential nonlinearity at different light intensities, the same optical filters were used, that were already discussed in detail in section 10.2. In this section problems with the accuracy of the filter calibration were observed. However, they can still be used for this measurement since here no information about the transmission coefficients is required. The E158 method only uses the filters to attenuate the LED light to be able to measure at different intensities. It is extraneous how large exactly the attenuation actually is.

Measurements were done using the filters 2, 3, and 4, and all combination of these. See table 10.2 on page 122 for details on these filters. In addition one measurement was done without any filter. Each of these measurements consisted of three parts. Each LED was pulsed separately, and then both were operated simultaneously. $10^7$ pulses were recorded for each part.

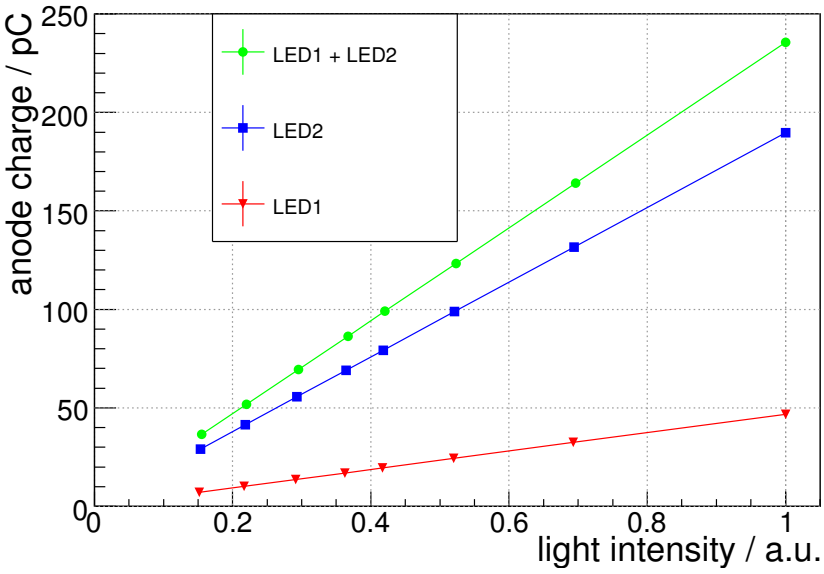


***Figure 10.21.:*** *E158 Method: Anode charge for three LED and eight filter configurations.*

### 10.5.1. Results

The data recorded with the E158 method are shown in figure 10.21. The plot shows the recorded anode charge as a function of different light intensities, given in arbitrary units. This is shown for the three cases of only one of two and both LEDs being pulsed. The approximate ratio of 1/4 between the two LED configurations can be seen in the plot. The differential nonlinearity of the photodetector can now be calculated via:

$$\mathrm{DNL} = \frac{Q(\mathrm{LED1}) + Q(\mathrm{LED2})}{Q(\mathrm{LED1{+}LED2})}$$

The results can be found in figure 10.22 on the facing page. The differential nonlinearity is clearly visible. The nonlinearity measured with this method appears to be smaller than with the double pulse method (figure 10.20). In contrast to the results of the previous method a positive slope can be observed. The zero crossing of this line appears approximately at an output charge of 150 pC. A more detailed comparison and discussion of these results will be given in the following section.

## 10.6. Comparison of Results Obtained with Different Methods

In this section the differential nonlinearities acquired with the E158 method are compared to the results obtained by the pulse length method. However, the latter was used

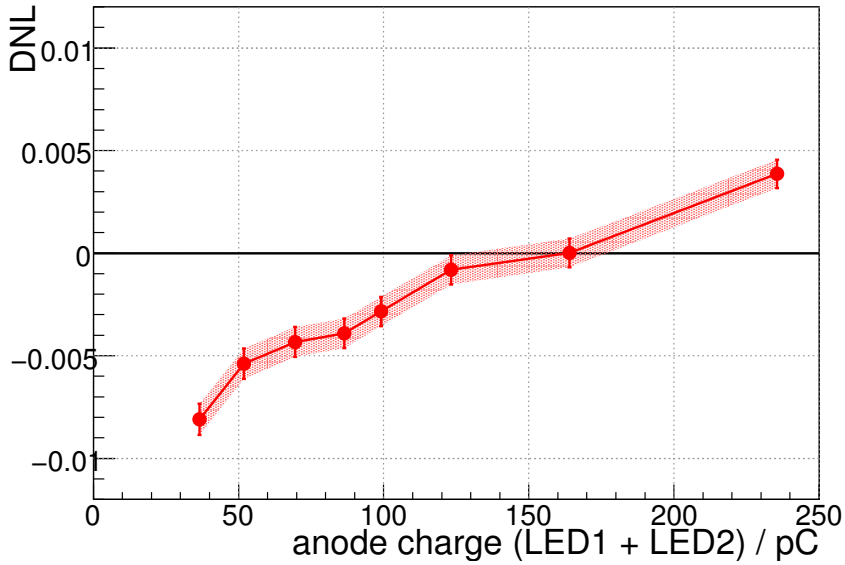


***Figure 10.22.:*** *E158 Method: Differential nonlinearity in dependence of the anode charge recorded with both LEDs pulsed simultaneously.*

to measure the *integral* nonlinearity. So first it will be discussed how the data acquired with this method can be used to calculate a *differential* nonlinearity.

### 10.6.1. Extracting a Differential Nonlinearity from the Pulse Length Method

Figure 10.23 shows the data recorded with the pulse length method (see section 10.3 on page 126). It shows the same data as figure 10.9. The analysis of the data follows in principle the one used to extract the differential nonlinearity with the double pulse method (see section 10.4). In that method a very small pulse from a second LED was used to study the differential behavior of the anode charge depending on the pulse length.

The data acquired with the pulse length method are now interpreted in a similar way. A data point (recorded at a pulse length of $t$) is assumed to be generated by the first large LED pulse alone, while the following data point (recorded at a pulse length of $t + 5\,\mathrm{ns}$) is interpreted as being produced by adding a second smaller LED pulse to the first. This is, of course, only a very coarse approximation at a differential measurement, but it will suffice for a comparison with the E158 method.

Figure 10.24 on page 143 shows the difference in the anode charge between consecutive pulse length measurements, in ratio to the anode charge of the respective first pulse. It is plotted versus the anode charge. As in the double pulse method this graph

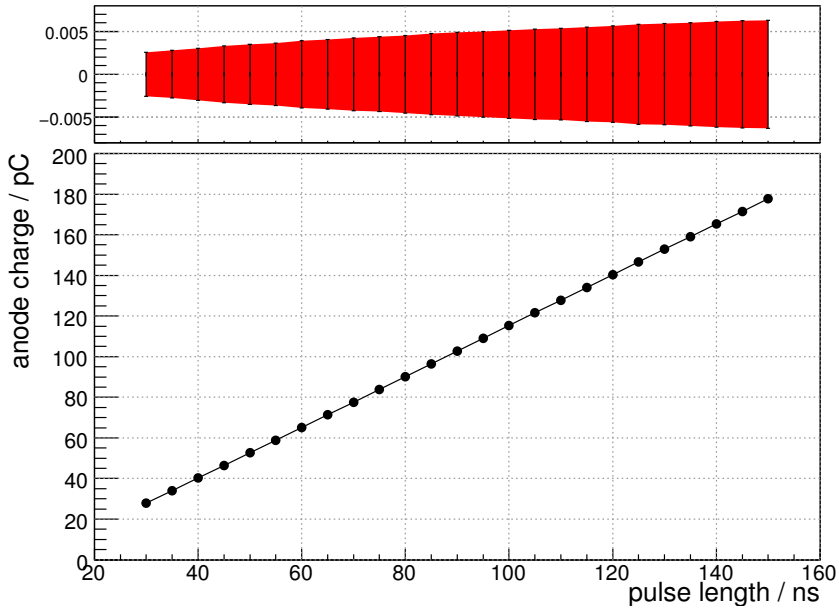


***Figure 10.23.:*** *Pulse length measurement: the recorded anode charge for different LED pulse lengths. Only statistical errors are applied.*

should be, for an ideal photodetector, of the form

$$\frac{p_0}{Q} \tag{10.8}$$

An according parametrization has been fitted to the data. The differential nonlinearity is acquired as the relative deviation from the ideal behavior.

The result can be found in figure 10.25 on the next page. A positive slope is again visible in the data, albeit preceded by a negative slope at low anode charges. The differential nonlinearities are for the most part in an interval between $-0.005$ and $0.005$, thus being in the same range as those measured with the E158 method.

## 10.6.2. Comparison of Results

Figure 10.26 on page 144 shows a comparison of the differential photodetector nonlinearities acquired by two different methods, plotted versus the anode charge. The red squares the E158 method, while the green triangles stand for the differential nonlinearity extracted from the pulse length method's data. The E158 and pulse length method show good agreement, at least in the range between 50 and 150 ns. Furthermore, both methods show the same basic characteristics in the range between 50 and 150 pC: a soft positive slope, and a zero crossing at around 140 pC.

However, some inconsistencies cannot be denied. At both ends of the DNL spectrum extracted from the pulse length measurement deviations from the E158 method can be observed. The discrepancies at short pulse lengths may be attributed to a finite

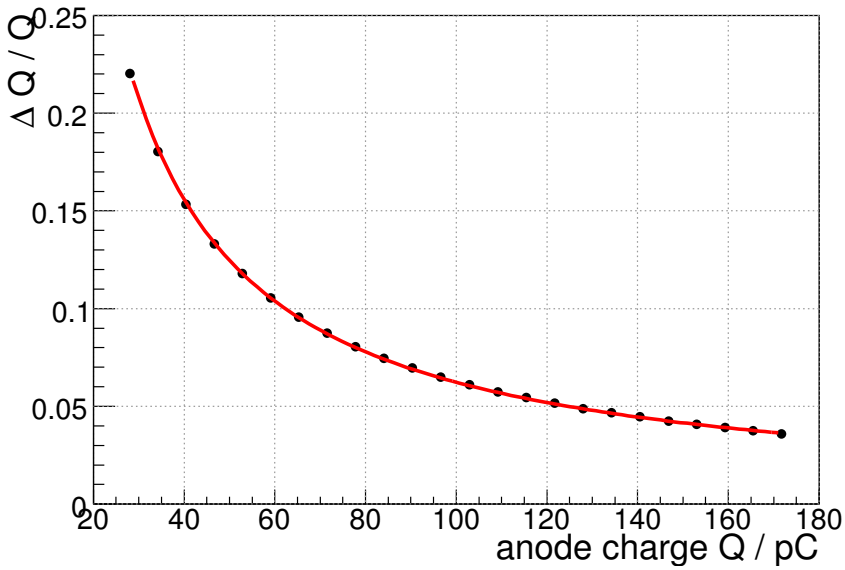


***Figure 10.24.:*** *Pulse length measurement: Differential interpretation of data. The difference in the anode charge between consecutive pulse length measurements, in ratio to the anode charge of the respective first pulse, is plotted versus the anode charge. A parametrization is fitted to the data.*

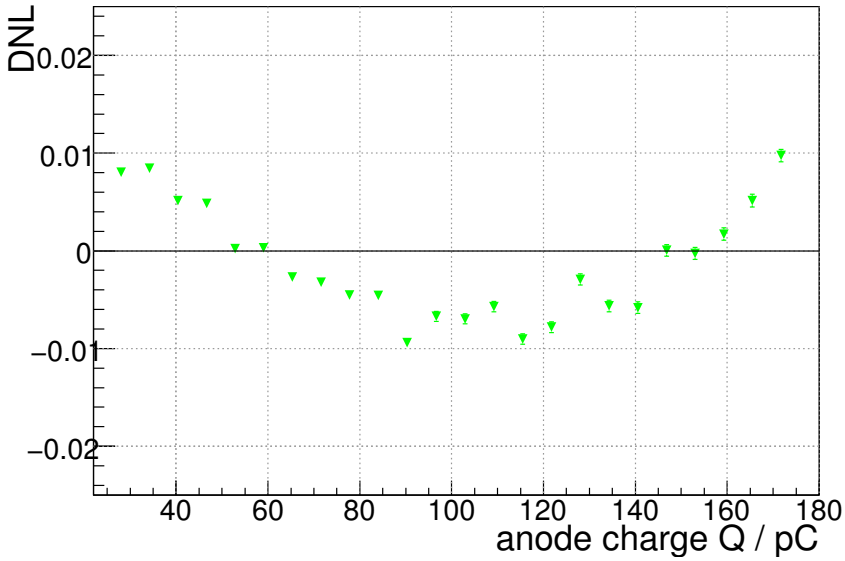


***Figure 10.25.:*** *Pulse length measurement: Differential nonlinearity extracted from the data.*

LED rise time. This has already been discussed for the pulse length method. It may be that at pulse lengths below $\approx 50\,\mathrm{ns}$ the LED pulse form cannot be approximated

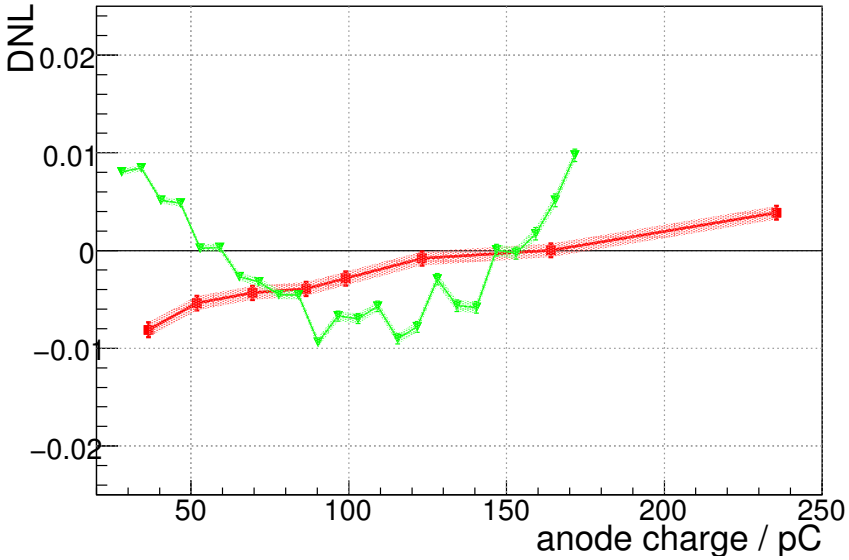


***Figure 10.26.:*** *Comparison of differential nonlinearities acquired by two different methods in a zoomed view.*
*red squares: E158 method*
*green triangles: pulse length method.*

as rectangular. The deviations at long pulse lengths are not understood yet. Effects from an altered potential configuration in the photodetector's dynode structure due to extended charge clouds at longer pulse length can be a possible explanation. This should be investigated further in future works on this topic.

Nevertheless, taking into account the coarse information generally available on photodetectors' nonlinearities the measured consistency at the subpercent level between data gathered from two very different methods can be considered an achievement. This seems to justify the validity of the ansatz chosen for the pulse length measurement.

## 10.7. Long Term Stability and Calibration

The measurement of subpercent nonlinear effects in the photodetector output is a success of this analysis. However, the question arises if the methods developed are applicable for the calibration of the Cherenkov detector during polarization measurements at a running ILC experiment. In that situation it is desirable to constantly correct the recorded spectra for the photodetectors' nonlinearities to improve the accuracy of the polarization measurement. In other words, it is to be clarified whether the measured nonlinearities are stable over a longer period of time, and if one series of measurement can be used to correct others.

In order to check the reproducibility of the measurements, the pulse length method

described above has been applied several times over a longer period of time, and the integral nonlinearity has been calculated. The nonlinearity obtained from the measurement described in section 10.3.3 has been used to correct the nonlinearities measured in the repetition measurements. A correction of QDC nonlinearities has been performed (cf. section 10.3.4). The plot of the nonlinearity used as reference measurement can be found in figure 10.17 on page 135.

A total of twelve series of pulse length measurements (including the reference measurement) have been performed over a span of about 40 days. Measurements have taken place both on consecutive days and as long as four weeks apart.

An overview of results is shown in figure 10.27 on page 147. The reference measurement is shown in subfigure (e). The other subfigures show the reproducibility measurements. The measured integral nonlinearity is plotted as red squares. The corrected values are shown as blue circles with the band representing the combined statistical and systematic errors. The legend shows the reduced $\chi^2$ and the fit probability for both the uncorrected and the corrected graphs with respect to a zero line. Figure 10.27 merely gives an overview. Larger plots will be shown in the following passages. All the graphs shown in this section have been corrected for the QDC nonlinearity.

A long time effect can clearly be seen in the plots. For measurements which have been taken only a couple of days before or after the reference measurement (subfigures (a) to (g)), the nonlinearity can be corrected for very successfully. Larger plots of the results of these measurements can be found in figure 10.28 on page 148.

The measurement in figure 10.27(h), which has been performed seven days after the reference measurement, can still be corrected. However, the corrected graph already shows some discrepancy from a zero line.

The measurements shown in subfigures (i) to (l), which took place four weeks and longer after the reference measurement, cannot be corrected, with the exception of subfigure (k). The corrected graph of this measurement shows good consistency with a zero line.

Figure 10.29 on page 149 shows the measurements of figure 10.27(j) and (l) in a larger view. The plots on the left hand side are the same as in the overview of figure 10.27. That means they were corrected with a reference measurement that dates back about four weeks. As already mentioned, the correction was not successful for them. However, when using a more recent measurement as reference (the one from figure 10.27(i)), the correction succeeds. This can be seen in the plots on the right hand side of figure 10.29.

Usually, the nonlinearity of a photodetector is considered an intrinsic quality, that should not change over time. The results of this analysis are not meant to contradict this. In fact the stability of the entire setup was tested. It is possible that environmental effects may have caused the time dependence of the measured nonlinearities. Altogether, it has to be noted that a subpercent nonlinearity could be measured and successfully corrected for using regular reference measurements.

One can conclude that over a range of several days the nonlinearity is well under control and can be corrected for. At a scale of weeks, however, long time effects in the nonlinearity can be observed. Thus, reference measurements have to be taken

regularly, and not more than one week apart. This would not prove difficult in a running ILC experiment. In the layout of the Cherenkov detector it is foreseen to include an LED in one leg of the gas tubes (see section 7). On-the-fly calibration runs could be taken between ILC runs. One might even consider taking calibration data in between consecutive trains. The time distance between two ILC bunch trains is projected to be 199 ms. At a readout frequency of 20 kHz, about 4000 LED pulses could be recorded between trains. Consecutive calibrations would need to be cumulated until sufficient statistics are achieved to be used as a reference measurement. By means of a sliding average over the last couple of reference measurements, an up-to-date calibration of the photodetectors could be guaranteed at all times.

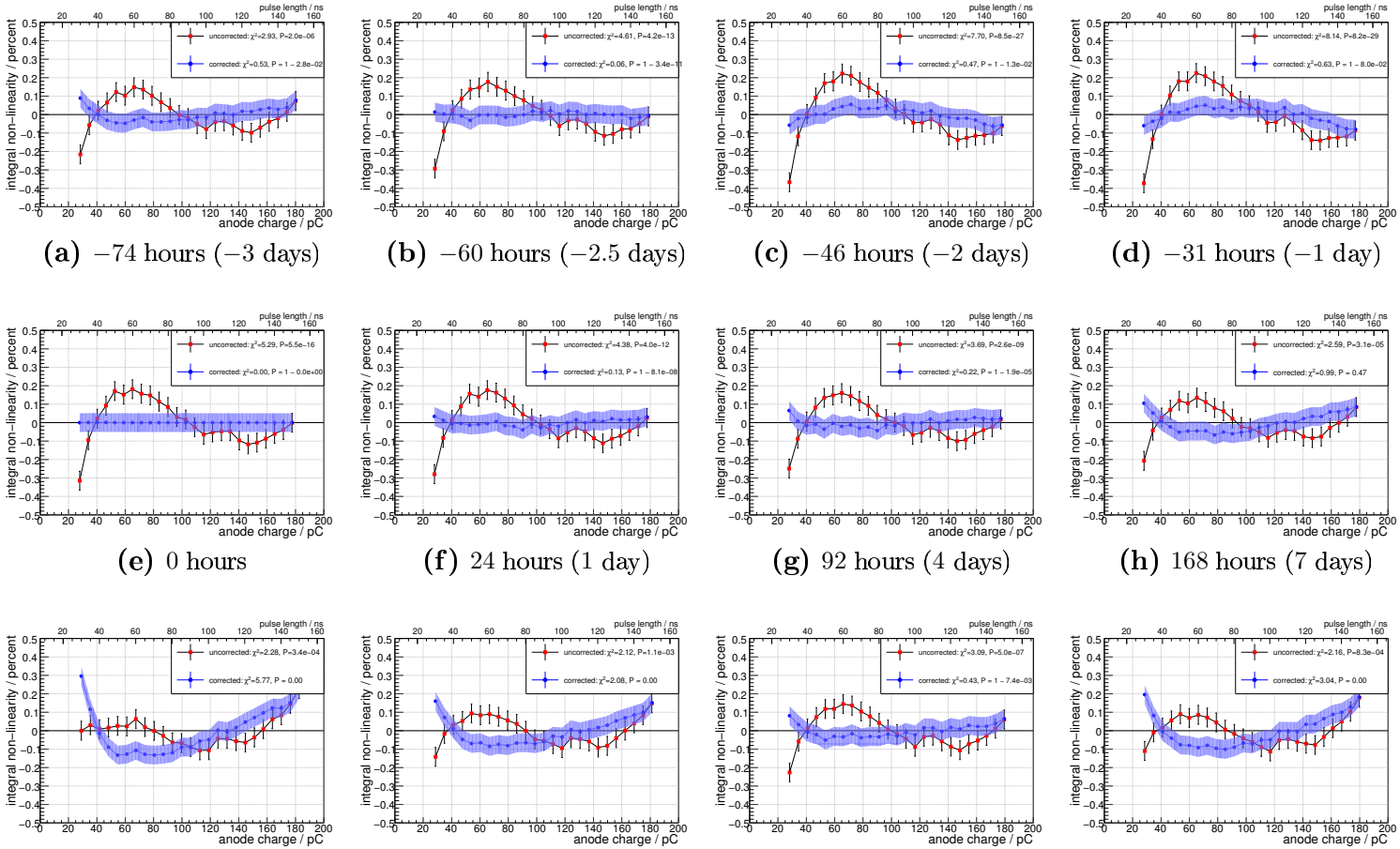


**(a)** −74 hours (−3 days) **(b)** −60 hours (−2.5 days) **(c)** −46 hours (−2 days) **(d)** −31 hours (−1 day)

**(e)** 0 hours **(f)** 24 hours (1 day) **(g)** 92 hours (4 days) **(h)** 168 hours (7 days)

**(i)** 672 hours (28 days) **(j)** 696 hours (29 days) **(k)** 718 hours (30 days) **(l)** 839 hours (35 days)

***Figure 10.27.:*** *Reproducibility of the pulse length method: Integral nonlinearity determined from independent series of pulse length measurements are corrected by a reference measurement (shown in (e)).*

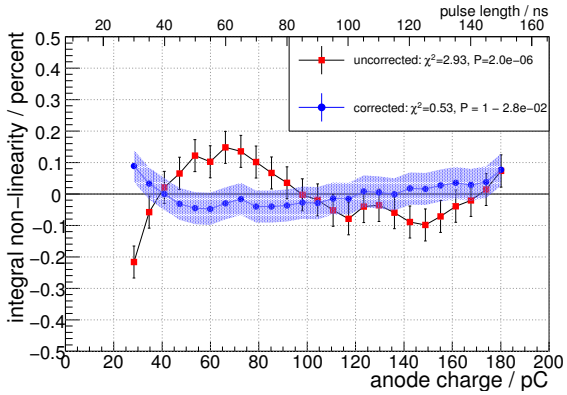


**(a)** −74 hours (−3 days)

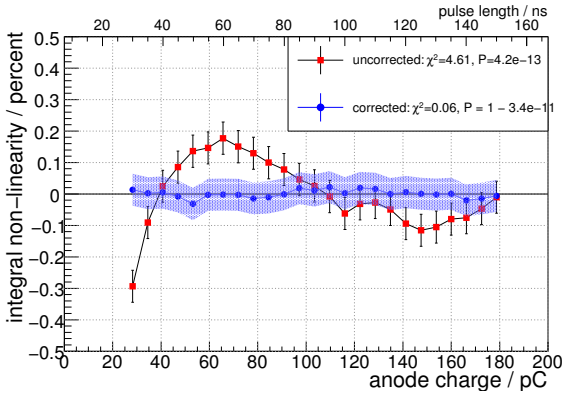


**(b)** −60 hours (−2.5 days)

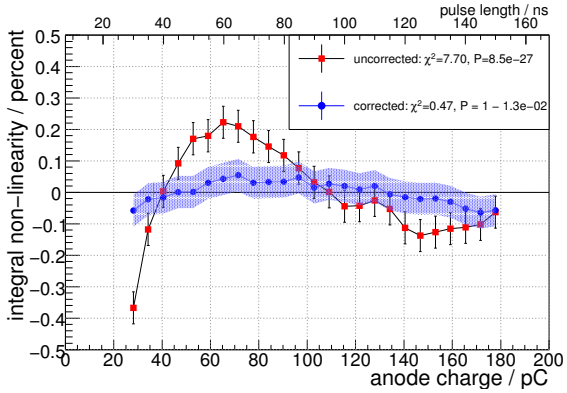


**(c)** −46 hours (−2 days)

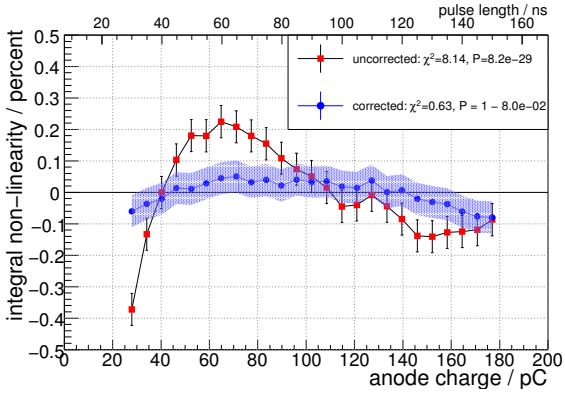


**(d)** −31 hours (−1 day)

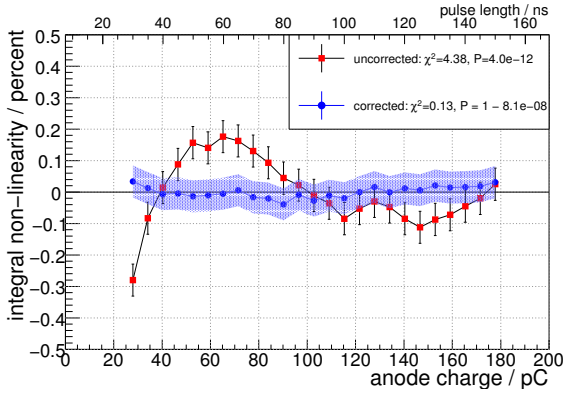


**(e)** 24 hours (1 day)

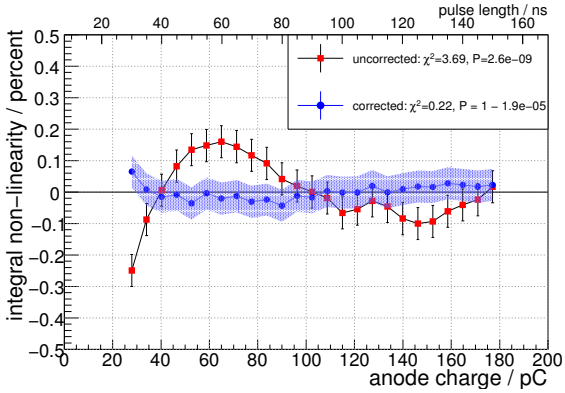


**(f)** 92 hours (4 days)

***Figure 10.28.:*** *Successful correction of nonlinearity measurements: Measurements taken within a few days of the reference measurement can be corrected very successfully.*

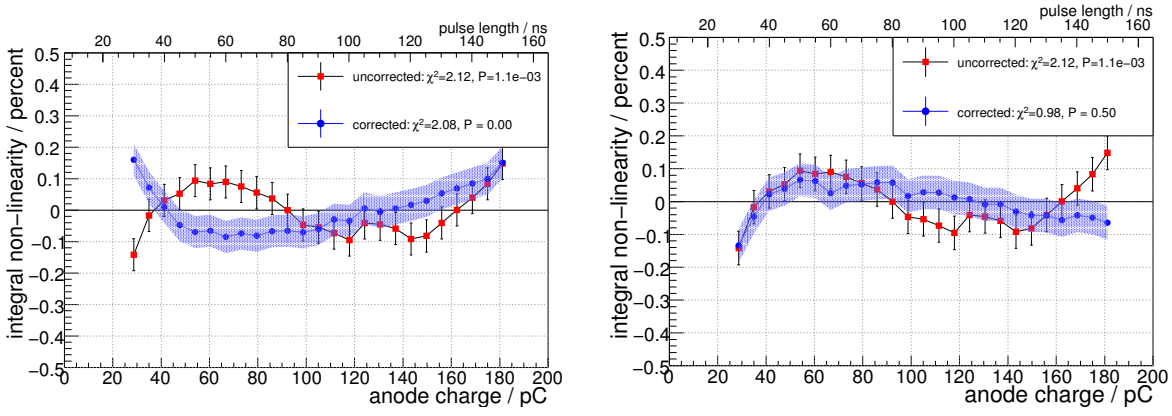


**(a)** 696 hours (29 days)




**(b)** 24 hours (1 day)

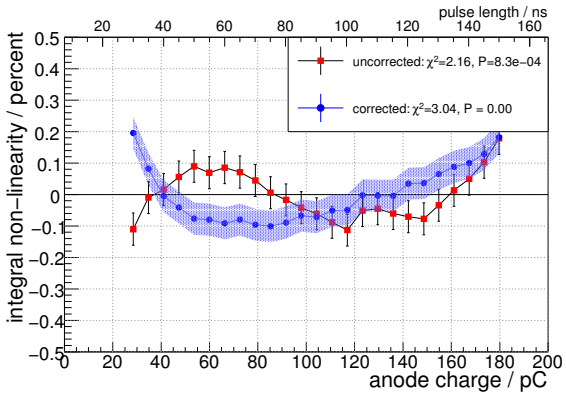


**(c)** 839 hours (35 days)

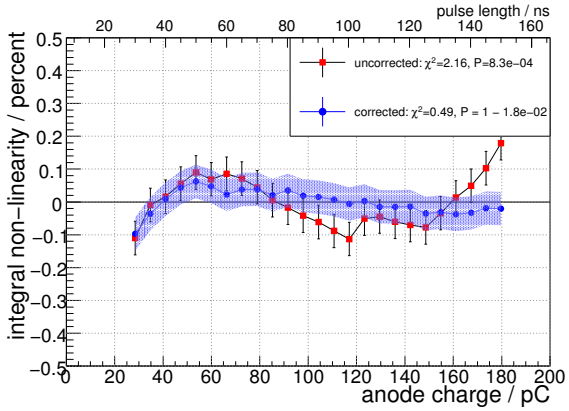


**(d)** 167 hours (7 days)

***Figure 10.29.:*** *Long time effects in the photodetector nonlinearity: The left hand side plots have been corrected with a reference measurement taken four weeks before. The right hand side plots have been corrected with a recent reference measurement. The respective time differences to the reference measurement is shown below the plots.*

# Conclusion and Outlook

The general topic of this thesis was the importance of polarized leptons in the search for new physics beyond the Standard Model at particle colliders. The first part of this thesis described a search for hypothetical particles called leptoquarks at the H1 experiment. The analysis has been performed on data with an integrated luminosity of $335\,\mathrm{pb}^{-1}$ recorded during the HERA-2 runphase. In this time period the beam leptons were longitudinally polarized. This fact was exploited to enhance the sensitivity of the analysis to the chirally coupling leptoquarks. The data was split up into subsamples according to lepton charge and helicity. Each sample had an average polarization of at least $\pm 25\%$. The two possible decay channels of first generation leptoquarks are indistinguishable from the Standard Model neutral and charged current processes. Hence, a selection of neutral and charged current events was performed. However, no evidence of the presence of leptoquarks was found. Using the statistical method of fractional event counting, limits depending on the mass and Yukawa coupling were calculated for the 14 leptoquark types of the Buchmüller-Rückl-Wyler model. The limits acquired by this analysis surpass those published for the HERA-1 runperiod except in cases for which the statistical method is limited by systematic uncertainties, that are still larger for the HERA-2 runperiod than for HERA-1. Once these issues are clarified, future searches for leptoquarks will be able to further improve the exclusion limits. In this analysis leptoquarks coupling with electromagnetic strength can be excluded at 95 % C.L. up to masses of $M_{\mathrm{LQ}} = 280 - 300$ GeV, depending on the leptoquark type.

It is expected that the planned linear collider ILC will open up a new domain of physics. At this electron positron collider polarized beams will enhance the ILC's potential to detect and measure new phenomena as well as Standard Model particles. However, in order to benefit from the beam polarization, it must be known with high accuracy. It is aimed to achieve an as yet unequaled precision of 0.25%. Experiences from other Compton polarimeters show that this goal is not limited by statistical but systematic effects. A crucial limiting factor will be the linearity of the photodetectors used in the polarimeter. In order to achieve a high precision polarization measurement these effects will have to be controlled to approximately 0.1%. This is a level of precision that is not usually not provided by the manufacturer, and only few publications on this topic can be found. The second part of this thesis dealt with the development of methods to measure photodetector nonlinearities with this precision. A test facility has been assembled in order to measurements. Several methods were devised and tested using a multianode photodetector. Two successful methods have been developed. One

measures the integral nonlinearity of the photodetector by varying the pulse length of LED light irradiating the photocathode. An integral nonlinearity of $(0.5 \pm 0.05)\%$ was measured for the photodetector. With second method it was possible to measure the differential nonlinearity in the subpercent regime. As cross check, a differential nonlinearity was extracted from the former method. The results were conclusive for the most part. However, some issues still need clarification. Although it has been tried to keep this effect minimal, the variation of the pulse length may still influence the linearity of the device. This will have to be investigated further.

The pulse length method has been used to test the long term stability. It has been found that the measured nonlinearity shows a time dependence. This may be attributed to environmental effects on the entire setup. Still, the photodetector nonlinearity could be corrected successfully for measurements taken several days apart.

Both methods could be used in an ILC polarimeter to correct the data for photodetector nonlinearities. The limited dynamic range covered by the methods described herein can easily be expanded. By gradually increasing the amplitude voltage used to operate the LED, the methods described herein can be used to cover any dynamic range. The calibration process described above could easily be performed at an ILC polarimeter between or even during ILC runs, via LEDs that are planned to be installed in the polarimeter.

# List of Figures


1.1. Generic layout of a Compton polarimeter. . . . . 5
1.2. Differential Compton cross section for different polarization configurations. 5
1.3. Electron spin configuration and polarimeters at HERA. . . . . 7
1.4. The International Linear Collider . . . . . 7

2.1. Deep inelastic scattering . . . . . 14
2.2. Electroweak radiative corrections. . . . . 15
2.3. The $Q^2$ dependence of the neutral and charged current cross sections as measured by H1. . . . . 18
2.4. Polarization dependence of the charged current cross section. . . . . 19
2.5. Polarization dependence of the neutral current cross section. . . . . 20
2.6. Standard Model background processes. . . . . 21
2.7. Leptoquark processes in $ep$ collisions. . . . . 24

3.1. The H1 Detector. . . . . 28
3.2. Side view of the H1 tracking system. . . . . 29
3.3. Radial view of the H1 central tracking detector. . . . . 30
3.4. Schematic of the H1 forward tracking detector. . . . . 31
3.5. The Liquid Argon calorimeter. . . . . 32
3.6. Overview of the H1 trigger system. . . . . 35

4.1. Effect of electron energy calibration. . . . . 43
4.2. Effect of hadronic energy calibration. . . . . 44

5.1. Timing profile of the data. . . . . 48
5.2. Effect of electron requirements on the neutral current selection. . . . . 54
5.3. The longitudinal momentum balance before application of the cut on the neutral current selection. . . . . 55
5.4. The longitudinal momentum balance before application of the cut on the charged current selection. . . . . 56
5.5. The missing transverse momentum before application of the cut. . . . . 57
5.6. Schematic of the definition of acoplanarity. . . . . 58
5.7. The distribution of $\mathcal{V}$ plotted against $P_T^{\mathrm{miss}}$ before the cut. . . . . 59

5.8. Monte Carlo reweighting factors for background finders and trigger efficiency. . . . 61
5.9. Example of vertex reweighting. . . . 62
5.10. Event yields for neutral and charged current selections. . . . 65
5.11. Control plots for the neutral current selection. . . . 67
5.12. Control plots for the neutral current selection. . . . 68
5.13. Control plots for the charged current selection. . . . 69
5.14. Control plots for the charged current selection. . . . 70
5.15. Problematic charged current selection in 06R period. . . . 71

6.1. Leptoquark mass for neutral and charged current selections. . . . 74
6.2. $M_{\mathrm{LQ}} - y$ binning used in leptoquark search. . . . 75
6.3. Example of weights used in leptoquark search. . . . 77
6.4. Exclusion limits on scalar and vector leptoquarks. . . . 81
6.5. Comparison with HERA-1 results. . . . 82
6.6. Comparison of exclusion limits on two scalar leptoquark types with other results. . . . 83

7.1. Coordinate system of Compton scattering. . . . 87
7.2. Analyzing power for Compton scattering off longitudinally polarized electrons. . . . 90
7.3. Magnetic chicane for the ILC Polarimeter. . . . 91
7.4. Top view of the Cherenkov hodoscope. . . . 92
7.5. Side view of a Cherenkov counter. . . . 92

8.1. Schematic diagram of a photomultiplier tube. . . . 96
8.2. Different dynode structures. . . . 97
8.3. Operating principle of a QDC. . . . 100
8.4. Definition of the differential nonlinearity. . . . 101
8.5. Definition of the integral nonlinearity. . . . 102

9.1. Schematic of the light-tight box used in the measurements. . . . 103
9.2. Mesh structure of the Hamamatsu R5900. . . . 105
9.3. Characteristics of Hamamatsu R5900. . . . 106
9.4. The LED's emission spectrum. . . . 106
9.5. Histogram Testing Method. . . . 108
9.6. Differential nonlinearity of the QDC. . . . 109
9.7. Integral nonlinearity of the QDC in units of least significant bits. . . . 110
9.8. Integral nonlinearity of the QDC in percent. . . . 110
9.9. A typical photodetector spectrum. . . . 111
9.10. Effect of the QDC correction on the photodetector spectrum. . . . 112
9.11. Effect of the QDC correction on fit values. . . . 113

10.1. Example of Multi-Poisson fit method . . . 117

10.2. Example of Gaussian fit method . . . . . 118
10.3. Filter transmission coefficients as measured by LZH. . . . . 120
10.4. The LED's emission spectrum. . . . . 121
10.5. Quantum efficiency of the Hamamatsu R5900 multi-anode photomultiplier. 122
10.6. Determination of filters' transmission coefficients by a Monte Carlo method. 123
10.7. Photodetector linearity measurement with optical filters. . . . . 124
10.8. Integral nonlinearity of photodetector measured with optical filters. . . 125
10.9. Pulse length measurement: Recorded data and integral non linearity (statistical errors only). . . . . 126
10.10Three iteration steps of the $\chi^2$ estimation of pulse length errors. . . . . 129
10.11Results of the $\chi^2$ estimation of pulse length errors. . . . . 130
10.12Estimation of systematic uncertainties due to fitting method. . . . . 131
10.13Difference between the integral nonlinearity (INL) obtained using the Gaussian and the Multi-Poisson approach. . . . . 132
10.14Pulse length measurement: Anode charge versus pulse length with full systematic and statistical uncertainties applied. . . . . 133
10.15Pulse length measurement: Integral nonlinearity of the photodetector. . 133
10.16Manufacturer's information on nonlinearity . . . . . 134
10.17Pulse length measurement: Integral nonlinearity of the photodetector, corrected for QDC nonlinearity. . . . . 135
10.18Double pulse measurement: Anode charge versus pulse length. . . . . 137
10.19Double pulse measurement: Difference between double and single pulse signals. . . . . 137
10.20Double pulse measurement: Differential nonlinearity. . . . . 139
10.21E158 Method: Anode charge for three LED and eight filter configurations. 140
10.22E158 Method: Differential nonlinearity. . . . . 141
10.23Pulse length measurement: Recorded data (statistical errors only). . . . 142
10.24Pulse length measurement: Differential interpretation of data. . . . . 143
10.25Pulse length measurement: Differential nonlinearity extracted from the data. . . . . 143
10.26Comparison of differential nonlinearities acquired by two different methods. 144
10.27Reproducibility of the pulse length method. . . . . 147
10.28Successful correction of nonlinearity measurements. . . . . 148
10.29Long time effects in the photodetector nonlinearity. . . . . 149

# List of Tables

2.1. Leptoquark types in the BRW model. . . . . 23

4.1. Data sets used in this analysis. . . . . 38
4.2. Integrated luminosities of Monte Carlo simulations used in this analysis. 44

5.1. Definition of subtriggers used in this analysis. . . . . 51
5.2. Systematic uncertainties for neutral and charged current selection. . . . 63
5.3. Event numbers for neutral and charged current selection. . . . . 65

10.1. Accuracy of transmission coefficient measurements of optical filters. . . 120
10.2. Transmission coefficients of optical filters. . . . . 122

# Bibliography


[1] D. Griffiths. *Introduction to Elementary Paricles.* Wiley, New York, 1987. 392 p.

[2] S. L. Glashow. Partial Symmetries of Weak Interactions. *Nucl. Phys.*, 22:579–588, 1961.

[3] Abdus Salam and John Clive Ward. Gauge theory of elementary interactions. *Phys. Rev.*, 136:B763–B768, 1964.

[4] Steven Weinberg. A Model of Leptons. *Phys. Rev. Lett.*, 19:1264–1266, 1967.

[5] I. J. R. Aitchison and A. J. G. Hey. *Gauge theories in particle physics: A practical introduction. Vol. 2: Non-Abelian gauge theories: QCD and the electroweak theory.* Institute of Physics, Bristol, 2004. 454 p.

[6] F. Halzen and A.D. Martin. *Quarks and Leptons.* Wiley, New York, 1984. 396 p.

[7] Peter W. Higgs. Broken symmetries, massless particles and gauge fields. *Phys. Lett.*, 12:132–133, 1964.

[8] Peter W. Higgs. Broken symmetries and the masses of gauge bosons. *Phys. Rev. Lett.*, 13:508–509, 1964.

[9] Wu-Yang Tsai, L. Deraad, and K. A. Milton. Weak-boson triangle anomalies. *Phys. Rev.*, D8:1887–1890, 1973.

[10] H1 Collaboration. First measurement of charged current cross sections at HERA with longitudinally polarised positrons. *Phys. Lett.*, B634:173–179, 2006.

[11] Gudrid A. Moortgat-Pick et al. The role of polarized positrons and electrons in revealing fundamental interactions at the linear collider. *Phys. Rept.*, 460:131–243, 2008.

[12] V. Gharibyan, N. Meyners, and P. Schüler. The TESLA Compton polarimeter. 2001. LC-DET-2001-047; In: *2nd ECFA/DESY Study 1998-2001* 2131-2180.

[13] A. A. Sokolov and I. M. Ternov. On polarization and spin effects in the theory of synchrotron radiation. *Sov. Phys. Dokl.*, 8:1203–1205, 1964.

[14] A. Airapetian et al. Using the HERA Polarization Measurements - Recommendations for the Summer 2007 Conferences, 2007. `http://www.desy.de/~pol2000/documents/pol2000-2007-001.pdf`.

[15] Graphic courtesy of ILC, form one visual communication, `http://www.linearcollider.org`.

[16] ILC Collaboration. *ILC Reference Design Report.* 2007. `http://www.linearcollider.org/rdr/`.

[17] Andrei Nikiforov. *Measurements of the Neutral Current $e^{\pm}$ Cross Sections Using Longitudinally Polarised Lepton Beams at HERA II.* PhD thesis, Ludwigs-Maximilians-Universität München, 2007.

[18] H. Spiesberger et al. Radiative corrections at HERA. 1991. Contribution to Workshop on Physics at HERA, Hamburg, Germany, Oct 29-30, 1991.

[19] H1 Collaboration. Measurement and QCD analysis of neutral and charged current cross sections at HERA. *Eur. Phys. J.*, C30:1–32, 2003.

[20] H1 Collaboration. High $Q^2$ Charged Current in polarised $ep$ collisions. *Int. J. Mod. Phys.*, A22:5413–5607, 2007. In: *High energy physics. Proceedings, 33rd International Conference, ICHEP 2006, Moscow, Russia, July 26-August 2, 2006.*

[21] R. J. Cashmore et al. Measurement of weak neutral current couplings of quarks at HERA. 1996. Talk given at Workshop on Future Physics at HERA, Hamburg, Germany, 30-31 May 1996.

[22] Particle Data Group. Review of particle physics. *J. Phys.*, G33:1–1232, 2006.

[23] Matthias Enno Janssen. *Performance studies of a time projection chamber at the ILC and search for lepton flavour violation at HERA II.* PhD thesis, Universität Hamburg, 2008. DESY-THESIS-2008-011.

[24] W. Buchmüller, R. Rückl, and D. Wyler. Leptoquarks in lepton quark collisions. *Phys. Lett.*, B191:442–448, 1987.

[25] A. Djouadi et al. $(eb)$, $(et)$ type Leptoquarks at $ep$ Colliders. *Z. Phys.*, C46:679–686, 1990.

[26] H1 Collaboration. Search for lepton flavour violation in $ep$ collisions at HERA. *Eur. Phys. J.*, C52:833–847, 2007.

[27] ZEUS Collaboration. Search for lepton-flavor violation at HERA. *Eur. Phys. J.*, C44:463–479, 2005.

[28] H1 Collaboration. A Search for leptoquark bosons and lepton flavor violation in $e^+p$ collisions at HERA. *Eur. Phys. J.*, C11:447–471, 1999.

[29] H1 Collaboration. The H1 detector at HERA. *Nucl. Instrum. Meth.*, A386:310–347, 1997.

[30] H1 Collaboration. Homepage. `http://www-h1.desy.de`.

[31] B. Andrieu et al. Beam tests and calibration of the H1 liquid argon calorimeter with electrons. *Nucl. Instrum. Meth.*, A350:57–72, 1994.

[32] B. Andrieu et al. Results from pion calibration runs for the H1 liquid argon calorimeter and comparisons with simulations. *Nucl. Instrum. Meth.*, A336:499–509, 1993.

[33] F. Sefkow, E. Elsen, H. Krehbiel, U. Straumann, and J. Coughlan. Experience with the first level trigger of H1. *IEEE Trans. Nucl. Sci.*, 42:900–904, 1995.

[34] T. Nicholls et al. Concept, design and performance of the second level trigger of the H1 detector. *IEEE Trans. Nucl. Sci.*, 45:810–816, 1998.

[35] Jürgen Naumann. *Development and testing of the third level trigger for H1. (In German).* PhD thesis, Universität Dortmund, 2003. DESY-THESIS-2003-009.

[36] Stan Bentvelsen et al. Reconstruction of ($x$, $Q^2$) and extraction of structure functions in neutral current scattering at HERA. 1992. NIKHEF-H-92-02.

[37] A. Blondel and F. Jacquet. In: *U. Amaldi (ed): Study of an ep facility for Europe: Proceedings, ECFA, Hamburg, Germany, April 2-3.* 1979. DESY-79-48.

[38] Philippe Bruel. *Recherche d'interactions au-delà du Modèle Standard à HERA.* PhD thesis, Université Paris XI Orsay, 1998. in French.

[39] H1OO Group. Electron Finders in OO. `https://www-h1.desy.de/icas/oop/finders/efinder/oo-efinder.html`.

[40] M. Peez et al. An Energy Flow Algorithm for Hadronic Reconstruction In OO: Hadroo2. H1-IN-616(01/2005), 2005.

[41] Beate Heinemann. *Measurement of Charged Current and Neutral Current Cross Sections in Positron-Proton Collisions at* $\sqrt{s} \approx 300$ *GeV.* PhD thesis, Universität Hamburg, 1999.

[42] Stephen D. Ellis and Davison E. Soper. Successive combination jet algorithm for hadron collisions. *Phys. Rev.*, D48:3160–3166, 1993.

[43] Thomas Kluge. Jet Finder. `https://www-h1.desy.de/icas/oop/finders/jetfinder/jetfinderframe.ps.gz`.

[44] H1 Collaboration. Measurement of neutral and charged current cross-sections in electron - proton collisions at high $Q^2$. *Eur. Phys. J.*, C19:269–288, 2001.

[45] G. A. Schuler and H. Spiesberger. DJANGO: The Interface for the event generators HERACLES and LEPTO. 1991. In: *Hamburg 1991, Proceedings, Physics at HERA, vol. 3 1419-1432. (see HIGH ENERGY PHYSICS INDEX 30 (1992) No. 12988).*

[46] K. Charchula et al. Combined QED and QCD radiative effects in deep inelastic lepton - proton scattering: The Monte Carlo generator DJANGO6. *Comput. Phys. Commun.*, 81:381–402, 1994.

[47] Torbjorn Sjostrand et al. High-energy-physics event generation with PYTHIA 6.1. *Comput. Phys. Commun.*, 135:238–259, 2001.

[48] Torbjorn Sjostrand et al. PYTHIA 6.2: Physics and manual. 2001.

[49] Tetsuo Abe. GRAPE-Dilepton (Version 1.1): A generator for dilepton production in *ep* collisions. *Comput. Phys. Commun.*, 136:126–147, 2001.

[50] U. Baur et al. Electroweak vector boson production in high-energy *ep* collisions. *Nucl. Phys.*, B375:3–44, 1992.

[51] Christoph Berger and Patrick Kandel. A new generator for wide angle bremsstrahlung. 1998. Prepared for Workshop on Monte Carlo Generators for HERA Physics (Plenary Starting Meeting), Hamburg, Germany, 27-30 Apr 1998.

[52] J. Katzy. H1OO - an analysis framework for H1. 2005. In: *Interlaken 2004, Computing in high energy physics and nuclear physics*, 265-267.

[53] H1OO Group. Homepage. `https://www-h1.desy.de/icas/oop/`.

[54] ROOT. Homepage. `http://root.cern.ch/`.

[55] R. Brun and F. Rademakers. ROOT: An object oriented data analysis framework. *Nucl. Instrum. Meth.*, A389:81–86, 1997.

[56] E. Sauvan et al. Marana: A library for the analysis of the H1 events, 2005. `https://www-h1.desy.de/icgi-h1wiki/moin.cgi/MarAna`.

[57] Christian Helebrant. Analysis of charged weak current reactions and search for leptoquarks in HERA-II data of 2005. (In German). Diploma thesis, Universität Hamburg, 2006.

[58] Christian Veelken. H1NonepBgFinder - Rejection of cosmic muon and beam-halo events in the H1OO framework. H1-IN-603(09/2002), 2002.

[59] E. Chabert et al. QBGFMAR: An Updated Phan Package for Cosmic and Halo Muon Topological Rejection in High $P_T$ Physics Analysis. H1-IN-556(11/1998), 1998.

[60] Biljana Antunovic. *A First Measurement of the Charged Current DIS Cross Sections with Longitudinally Polarised Electrons in the H1 Experiment at HERA*. PhD thesis, Ludwigs-Maximilians-Universität München, 2007.

[61] H1 Collaboration. Search for leptoquark bosons in $ep$ collisions at HERA. *Phys. Lett.*, B629:9–19, 2005.

[62] Peter Bock. Computation of Confidence Levels for Exclusion or Discovery of a Signal with the Method of Fractional Event Counting. *JHEP*, 01:080, 2007.

[63] Stefan Schmitt. personal communication.

[64] OPAL collaboration. Tests of the standard model and constraints on new physics from measurements of fermion pair production at 183-GeV at LEP. *Eur. Phys. J.*, C6:1–18, 1999.

[65] L3 collaboration. Search for manifestations of new physics in fermion pair production at LEP. *Phys. Lett.*, B489:81–92, 2000.

[66] D0 collaboration. Search for first-generation scalar leptoquarks in $p\bar{p}$ collisions at $\sqrt{s} = 1.96$-TeV. *Phys. Rev.*, D71:071104, 2005.

[67] D. P. Barber et al. The HERA polarimeter and the first observation of electron spin polarization at HERA. *Nucl. Instrum. Meth.*, A329:79–111, 1993.

[68] S. Boogert et al. Polarimeters and Energy Spectrometers for the ILC Beam Delivery System. 2009.

[69] Robert Dean Elia. *Measurement of the left-right asymmetry in Z boson production by electron - positron collisions*. PhD thesis, Stanford University, 1994. SLAC-0429.

[70] P.L. Reinertsen. Non-Linear Effects in the Compton Polarimeter System and Impact on the Measured Electron Polarisation. SLD Note 261, 1999.

[71] Jenny List and Daniela Käfer. Improvements to the ILC Upstream Polarimeter. 2009.

[72] W. R. Leo. *Techniques for nuclear and particle physics experiments: A how to approach*. Springer, Berlin, 1987. 368 p.

[73] J.M. Schonkeren. *Photomultipliers*. Philips Application Book Series. Philips, Eindhoven, 1970.

[74] EMI Photomultiplier Catalog 1979. EMI Industrial Electronics Ltd., Ruslip, Middlesex, England.

[75] S. Dhawan. *IEEE Trans. Nucl. Sci.* **28**, 672, 1981.

[76] CAEN S.p.A. *Technical Information Manual: V965/V965A 16/8 channel Dual Range QDC*, 2007. revision 6.

[77] Hamamatsu Photonics K.K. *Photomultiplier Tubes: Basics and Applications (Third Edition)*, 2006. `http://www.hamamatsu.com`.

[78] Tektronix. *Arbitrary/Function Generators AFG 3011 / 3021B / 3022B / 3101 / 3102 / 3251 / 3252*, 2008. Data sheet, `http://www.tek.com/`.

[79] Ulrich Velte. Aufbau eines Teststandes für Photodetektoren und Teststrahlmessungen für die Strahlpolarisationsmessung am ILC. Diploma thesis, Universität Hannover, 2008. DESY-THESIS-2009-005, in German.

[80] Maxim. Histogram Testing Determines DNL and INL errors. *Application Note 2085*, 2003. `http://www.maxim-ic.com/appnotes.cfm/an_pk/2085/`.

[81] Agilent Technologies. *T-1 3/4 (5 mm) Precision Optical Performance InGaN Blue and Green Lamps - Technical Data*, 2002. Data sheet, `http://www.agilent.com`.

[82] Hamamatsu Photonics K.K. *Multianode Photomultiplier Tube R5900U-M4*, 1999. Data sheet, `http://www.hamamatsu.com`.

[83] Piotr Decowski, Darcy Lambert, and Laura Peterson. Tests of linearity of Hamamatsu R2154-07 PMT used in polarimetry measurements in the E158 experiment. *E158 Technical Note No. 67*, 2005.

# Danksagung

Die Fertigstellung dieser Arbeit signalisiert für mich auch den nahenden Abschied von DESY. Fünf Jahre sind eine lange Zeit, ja schon ein echter Lebensabschnitt. Daher möchte ich an dieser Stelle einige Personen erwähnen, die während dieser Zeit auf die ein oder andere Art eine wichtige Rolle für mich gespielt haben.

Zunächst möchte ich mich bei Dr. Jenny List für die ausgezeichnete Betreuung bedanken, ganz besonders auch für die Unterstützung während der *heißen Phase*.

Desweiteren danke ich Prof. Dr. Robert Klanner für die Übernahme des Zweitgutachtens meiner Dissertation und einige kritische Anmerkungen und wertvolle Hinweise.

Mein Dank geht auch an Prof. Dr. Caren Hagner für ihre Bereitschaft als Zweitgutachterin meiner Disputation zu fungieren und ihre Flexibilität bei meiner kurzfristigen Terminverschiebung.

Wichtig ist mir auch an dieser Stelle Dr. Benno List zu danken für seine wertvollen Ratschläge und aufbauenden Worte.

Ein sehr herzlicher Gruß geht auch an alle, mit denen ich während dieser Zeit ein Büro geteilt habe (glücklicherweise nicht mit allen zur gleichen Zeit): Christian, Christoph, Daniela, Jörgen, Lea, Michael, Moritz, Oleg, Oliver, Shiraz, Tammo und Uli.

Ausserdem möchte ich mich für den vielen Spaß und die schöne Zeit bedanken bei Alex, Diana, Franzi, Jeannine und Robert.

Zwei gute Freunde muss ich hier auch erwähnen: Dennis und Jan, Dr. Rock schuldet Euch noch ein Bier!

Ein ganz besonderer Dank geht an Dich, Kirsten, dafür, dass mir lange Zeit gar nicht bewusst wurde, wie nervös ich sein könnte. Und dafür dass Du da warst, als mich dieses Bewusstsein am Ende doch einholte.

Zu guter letzt danke ich natürlich meinen Eltern. Ohne Eure Unterstützung - auf so vielfältige Weise - hätte ich dies alles nie erreichen können.